frontiers in Earth Science

ORIGINAL RESEARCH
published: 12 February 2021
doi: 10.3389/feart.2020.594355

Tectonic Fabric, Geochemistry, and Zircon-Monazite Geochronology as Proxies to Date an Orogeny: Example of South Delhi Orogeny, NW India, and Implications for East Gondwana Tectonics

Subhash Singh[1], *Bert De Waele*[2], *Anjali Shukla*[1], *B. H. Umasankar*[1] *and Tapas Kumar Biswal*[1]*

[1]Department of Earth Sciences, Indian Institute of Technology Bombay, Mumbai, India, [2]SRK Consulting (Australasia) Pvt Ltd., West Perth, WA, Australia

OPEN ACCESS

Edited by:
Guillermo Booth-Rea,
University of Granada, Spain

Reviewed by:
Junpeng Wang,
China University of Geosciences Wuhan, China
Christoph Von Hagke,
RWTH Aachen University, Germany

***Correspondence:**
Tapas Kumar Biswal
tkbiswal@iitb.ac.in

Specialty section:
This article was submitted to Structural Geology and Tectonics, a section of the journal Frontiers in Earth Science

Received: 13 August 2020
Accepted: 17 December 2020
Published: 12 February 2021

Citation:
Singh S, De Waele B, Shukla A, Umasankar BH and Biswal TK (2021) Tectonic Fabric, Geochemistry, and Zircon-Monazite Geochronology as Proxies to Date an Orogeny: Example of South Delhi Orogeny, NW India, and Implications for East Gondwana Tectonics. Front. Earth Sci. 8:594355. doi: 10.3389/feart.2020.594355

We have dated the South Delhi orogeny, Aravalli-Delhi Mobile Belt (ADMB), NW India, using the tectonic fabric, geochemistry, and zircon-monazite geochronology as the proxies. The South Delhi Terrane (SDT), a passive margin domain in the ADMB, consists of multiply deformed (D_1–D_4) greenschist facies rocks and several granite plutons. The D_1 deformation is characterized by pervasive isoclinal recumbent F_1 fold and axial planar tectonometamorphic fabric, S_1, developed in all rock types. The S_1 minerals belong to peak greenschist facies metamorphism, M_1, suggesting syntectonic nature of M_1 with D_1. The age of the D_1-M_1 is constrained by the syncollisional peralkaline S type Sewariya granite which is characterized by magmatic/submagmatic fabric (S_m) coplanar with the S_1. The margin of the pluton is turned into quartzofeldspathic gneiss carrying the evidence of high temperature deformation. The age of Sewariya granite is estimated at ca. 878 Ma by zircon geochronology. The D_1-M_1 is further constrained by monazite geochronology of the mica schist at ca. 865–846 Ma. The other granite plutons and metarhyolite are pre-D_1 and emplaced at ca. 992–946 Ma. The D_2 deformation produced NE-SW trending open upright F_2 folds coaxial with the F_1, and northwesterly vergent F_2–axial planar thrusts. Monazite geochronology constrains the D_2 at ca. 811–680 Ma. The D_3 is characterized by small to large scale NW-SE folds, and the D_4 by faults and fractures marking the brittle deformation in the rocks. The D_4 is constrained by monazite geochronology at ca. 588–564 Ma. There are upper amphibolitic tectonic slivers along the D_2-Phulad thrust, belonging to the pre-Delhi rocks, which show ca. 1,638 Ma metamorphism age. From the above study, it is suggested that the South Delhi orogeny belongs to ca. 878–680 Ma marking the final amalgamation of Marwar Craton with the rest of India. This overlaps the early phase of the Pan-African orogeny (900–630 Ma). The brittle deformation, D_4, coincides with Kuunga orogeny (650–500 Ma). Our study implies that India, like other continents in the East Gondwana, underwent amalgamation of internal blocks until the late part of the Neoproterozoic.

Keywords: blastesis-deformation relationships, granite, geochemistry, zircon-monazite geochronology, South Delhi orogeny, ca. 878–680 Ma, East Gondwana

INTRODUCTION

Amalgamation of continents took place through accretion and continental collision giving rise to supercontinental assembly. Orogens were created along the zone of amalgamation, which are marked by ductile as well as brittle deformation of rocks, different types of metamorphism, and intrusion of variety of magmatic rocks (Twiss and Moores, 1992; Kearey et al., 2009). A correlative study between tectonometamorphic fabric with geochronology of magmatic rocks and metamorphic mineral could estimate the life span of a supercontinental cycle (Hawkesworth et al., 2017). The earth underwent several orogenic cycles in the past since Neoarchean to Tertiary period. The Nuna orogeny was responsible for the formation of the Columbia Supercontinent (ca. 2.1 to 1.8 Ga, Rogers and Santosh 2002; Zhao et al., 2002), the Grenvillian orogeny was responsible for the Rodinia Supercontinent (ca. 1.3 to 1.0 Ga; Valentine and Moores, 1970; McMenamin and McMenamin, 1990; Meert and Torsvik, 2003; Cawood, 2005; Li et al., 2008), and the Pan-African orogeny created the Gondwana Supercontinent (0.9–0.5 Ga, Stern, 1994; Kroner and Stern, 2005; Fritz et al., 2013; Oriolo et al., 2017). Each orogeny comprises several phases of subduction and arc accretion that vary temporally and spatially at different parts of the Supercontinent. For example the Pan-African orogeny consists of an earlier phase of subduction and arc accretion (0.9–0.63 Ga) as observed in the Arabian-Nubian shield (Kroner and Stern, 2005) and a late phase of collision (Kuunga orogeny, ca. 0.65–0.50 Ga) in Madagascar, Tanzania, and other parts of Africa (Meert and Lieberman, 2008; Lehmann et al., 2016).

In this paper, we studied the South Delhi orogeny of the Archean-Neoproterozoic Aravalli-Delhi Mobile Belt (ADMB) in NW India that consists of several terranes juxtaposed along shear zones (**Figures 1A,B**). The terranes are Hindoli-Jahazpur, Mangalwar, Sandmata, Aravalli, North Delhi, South Delhi, and Sirohi terranes. The ADMB bears the imprint of the Nuna, Grenvillian, and Pan-African orogenies. The age of the South Delhi orogeny is still debated, if it is equivalent to Grenvillian or Pan-African, because most of the studies are based on single proxy. For instance, with very little analysis of magmatic vs. solid state fabric of the diorite (1.0 Ga, Volpe and Macdaugall, 1990), the Godhra granite (0.95 Ga, Gopalan et al., 1979), and the Chang granite (**Table 1**, 0.97 Ga, Tiwana et al., 2019), a Grenvillian age for the South Delhi orogeny was advocated (Roy, 2001). Similarly, based on monazite ages of Pilwa-Chinwali area without much consideration to deformation fabric Grenvillian age has been considered (Bhowmik et al., 2018). Contrarily, Singh et al. (2010) used zircon geochronology of granite and deformation history of host rocks and deduced ca. 0.87–0.65 Ga age, suggesting Pan-African age. Similar ages (ca. 0.87–078 Ga) were obtained by Tiwari and Biswal (2019a) who applied a combined study of monazite geochronology and deformation fabric to Ambaji granulite. We adopted a new approach wherein multiple proxies have been applied that include deformational structure in the metasediments and granite plutons to know chronological sequence of granite intrusion with deformation. Further, geochemistry of granites was studied to decipher the tectonic setting of their intrusion. Furthermore, zircon and monazite geochronology were conducted to date the granite plutons and tectonometamorphic fabric in the metasediments. Based on these studies, the South Delhi orogeny was found not directly related to Grenvillian or Kuunga orogeny (late part of Pan-African) rather to the early part of Pan-African orogeny. Therefore, we suggest that some of the orogenies observed in different continents may not have direct match with global scale orogenies which was responsible for building supercontinental assembly.

REGIONAL GEOLOGICAL SETTING AND OROGENIC CYCLES IN THE ARAVALLI-DELHI MOBILE BELT

The ADMB underwent three orogenic cycles, namely, Bhilwara, Aravalli, and South Delhi orogenic cycles (**Figure 1**; Synchanthavong and Desai, 1977; Sinha-Roy, 1988; Gupta et al., 1997; Biswal et al., 1998a,b; Bhowmik and Dasgupta, 2012). The Bhilwara orogenic cycle belongs to Archean age and is represented by multiply deformed, metamorphosed, migmatized greenstone-tonalite-trondhjemite-granodiorite gneisses of the Mewar gneiss, Mangalwar, Sandmata, Hindoli-Jahazpur terranes, and Beawar and Anasagar gneisses (**Figures 1B–D**) (ca. 3.3 Ga to 2.8 Ga age, Kaur et al., 2020 and reference therein). All these terranes were part of Marwar-Bundelkhanda Craton (**Figure 1C**). The Bhilwara orogeny terminated with westerly subduction and intrusion of arc setting Berach, Gingla, and Jhiri granites at 2.6 Ga (**Figure 1D**). The Aravalli orogenic cycle initiated during Paleoproterozoic period and was manifested in the Aravalli and North Delhi terranes (**Figure 1B**). The cycle was marked by rifting and creation of expansive continental margin (ca. 2.0 Ga, **Figure 1E**) where thick sequence of sandstone-shale-carbonate rocks with interbedded rift-generated bimodal volcanics were deposited with conglomerate and palaeosol at the base (Pandit et al., 2008; De Wall et al., 2012; Mehdi et al., 2015; Wang et al., 2014). The N-S aligned inverted V-shaped Aravalli Terrane comprises shallow water stromatolites bearing rocks in the east and low metamorphic grade carbonate and pelitic rocks in the west. The Aravalli orogeny is marked by subduction along Rakhabdev shear zone (**Figure 1F**), emplacement of ophiolites at 1.8 Ga, intrusion of granulite and charnockite plutons in the Sandmata Terrane at ca. 1.7 Ga, granulite facies metamorphism in the Pilwa-Chinwali area at 1.7 Ga (Fareeduddin et al., 1994; Bhowmik et al., 2018), and arc setting rhyolite and volcanic tuffs volcanism in the Hindoli-Jahazpur Terrane at 1.8 Ga (Deb et al., 1989; Verma and Greiling, 1995; Deb and Thorpe, 2001; Raza and Siddiqui, 2012). The Mangalwar Terrane was completely metacratonized

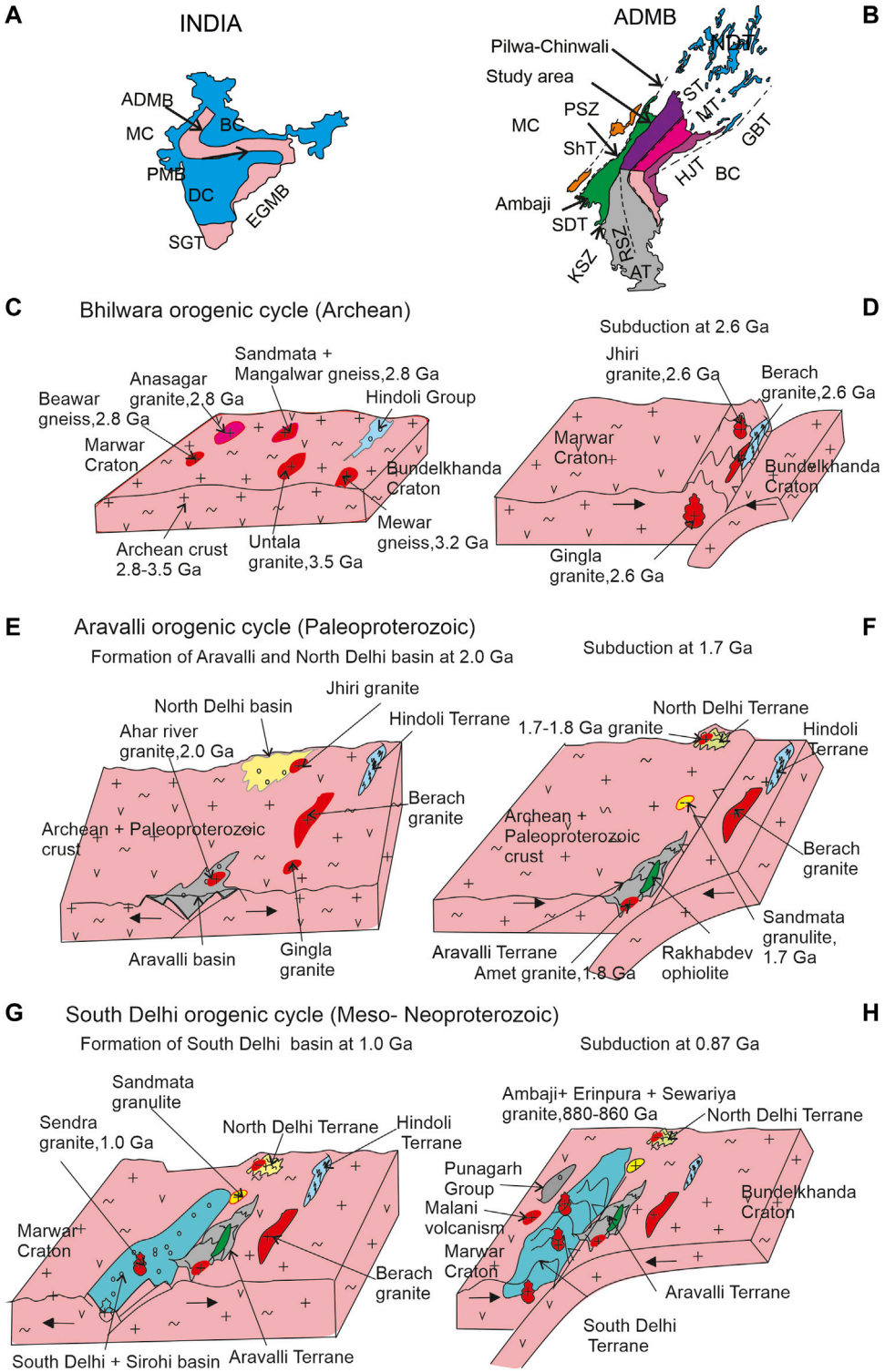

FIGURE 1 | (A) Peninsular India with location of various cratons and mobile belts. Abbreviations: ADMB: Aravalli-Delhi Mobile Belt, BC: Bundelkhanda Craton, DC: Dharwar Craton, EGMB: Eastern Ghats Mobile Belt, MC: Marwar Craton, PMB: Proterozoic mobile belt, SGT: Southern Granulite terrane. **(B)** Simplified terrane map of the ADMB (Singh et al., 2010). Abbreviations: AT: Aravalli Terrane, BC: Bundelkhanda Craton, GBT: Great Boundary Thrust, HJT: Hindoli-Jahazpur Terrane, KSZ: Kaliguman Shear Zone, MT: Mangalwar Terrane, MC: Marwar Craton, NDT: North Delhi Terrane, PSZ: Phulad Shear Zone, RSZ: Rakhabdev shear zone, SDT: South Delhi Terrane, ShT: Sirohi Terrane. **(C)** Schematic diagram of the Bhilwara, Aravalli, and South Delhi orogenic cycles: The Archean crust was 2.8–3.5 Ga old, the relicts are left out as Mewar gneiss, Untala granite, Beawar gneiss, and Sandmata-Mangalwar gneisses. Hindoli group was probably a greenstone belt; all these were

(*Continued*)

FIGURE 1 | part of Marwar-Bundelkhanda Craton. **(D)** Subduction/collision at 2.6 Ga, between Bundelkhanda Craton and Marwar Craton, marking the Bhilwara orogeny. Berach granite, Gingla granite, and Jhiri granite produced from the remelting of the subducting slab. **(E)** Aravalli orogenic cycle initiated with opening of Aravalli basin and North Delhi basin on the Archean-Paleoproterozoic Craton, at ca. 2.0 Ga. Ahar river granite served as basement of Aravalli sediments. **(F)** Aravalli orogeny occurred at 1.7 Ga, subduction along Rakhabdev suture zone, ophiolites were obducted, Sandmata granulites intruded to gneissic basement, and Amet granite intruded. **(G)** South Delhi orogenic cycles initiated with opening of South Delhi basin at 1.0 Ga; the Sirohi basin may be at the western flank of the South Delhi basin; during rifting Sendra granite, Ranakpur diorite, Bilara granite intruded. **(H)** South Delhi orogeny at 0.88 Ga, subduction/collision, arc magmatism in form of Ambaji granite, Erinpura granite and Sewariya granite, Marwar Craton was metacratonized, postorogenic extension created normal faulting, opened Punagarh basin.

during the Aravalli orogeny. The North Delhi Terrane, of nearly equidimensional shape (Heron, 1953), consists of shallow water sedimentary and volcanic sequences deposited in several grabens (age ca. 2.5–1.7 Ga) (Kaur et al., 2006; Mehdi et al., 2015). The sediments were folded along NE-SW axis (Ray, 1974; Gupta et al., 1998), metamorphosed in greenschist facies (0.95 Ga, Pant et al., 2008), and intruded by several granite plutons ranging in age from ca. 2.5 Ga to 0.8 Ga (Kaur et al., 2006, 2013; Misra et al., 2020). The Aravalli orogeny could be synchronous with Columbia Supercontinent amalgamation event (monazite ages of Mangalwar Terrane, 1.8–1.7 Ga, Bhowmik and Dasgupta, 2012; Columbia assembly ca. 2.1 to 1.7 Ga, Meert and Santosh, 2017). Ca. 1.0 Ga Grenvillian orogeny overprinted the Bhilwara-Aravalli rocks in form of granulite facies metamorphism in the Sandmata granulite (ca. 0.94 Ga, Bhowmik et al., 2010), Mangalwar Terrane (ca. 0.99 Ga, Ozha et al., 2016), and northern part of Bhilwara belt (Kumar et al., 2019). The South Delhi orogenic cycle initiated during Meso-Neoproterozoic period following Grenvillian orogeny, when the Marwar Craton underwent rifting to form the South Delhi and Sirohi basins (**Figure 1G**). The NE-SW trending linear South Delhi Terrane (SDT, **Figure 1B**) shows variation in lithological association. The northern part consists of low grade pelite-quartzite-carbonate sequence, the central part is dominated by metavolcanics known as Phulad ophiolite, and the southern part exposes amphibolite-granulite facies rocks (Biswal et al., 1998a, b; Khan et al., 2005). Distinct erosional unconformity is preserved in the northern part where the SDT-metasediments unconformably overlie the gneissic-granulitic rocks of Mangalwar and Sandmata terranes (Heron, 1953). Deposition of the SDT-metasediments was constrained between ca.1.2–0.87 Ga by Singh et al. (2010) and ca.1.74–1.06 Ga by Wang et al. (2014), and the granulite facies metamorphism was constrained at ca. 0.87–0.85 Ga (Tiwari and Biswal, 2019a). Bimodal volcanics and synrift extensional granitoids (Sendra granite, Ranakpura diorite, Bilara granite, ca.1.0 Ga) occur in the entire stretch of the SDT (**Table 1**, Biswal et al., 1998a, b; Bhattacharjee et al., 1988; Pandit et al., 2003; Singh et al., 2010). The South Delhi orogeny is marked by westerly subduction and formation of island arc system with intrusion of Ambaji, Erinpura, and Sewariya granites at 0.88–0.86 Ga (**Figure 1H**). The terrane is marked by multiple stages of folding and many longitudinal thrusts and faults (Naha et al., 1984, 1987; Biswal, 1988; Mukhopadhyay, 1989; Mukhopadhyay and Martin, 1991; Ghosh et al., 1999, 2003; Dasgupta et al., 2012). The basement rocks were thrusted up and occur as tectonic slices, e.g., the granite gneisses at Beawar and Ajmer (Tobisch et al., 1994; Chattopadhyay et al., 2012) and granulitic outcrop at Pilwa-Chinwali (1.7–1.5 Ga to 1.0 Ga age, Fareeduddin et al., 1994; Bhowmik et al., 2018; Singh et al., 2020). The Sirohi Terrane occurs to the west of the SDT in the form of isolated remnants of low grade metasediments in the western trans-Aravalli plain (probable age of sediments ca. 1.0 Ga, Roy and Sharma, 1999; Purohit et al., 2012) within expansive ca. 0.86–0.76 Ga old granites (Erinpura granite: Just et al., 2011; Malani Igneous Suite: Dharma Rao et al., 2013). Deformation and metamorphic events were dated ca. 0.9–0.8 Ga (Arora et al., 2017). Postorogenic extensional volcano-sedimentary sequences of the Sindreth and Punagarh basins overlie the Sirohi Terrane (**Figure 1H**) (Sharma, 2005; De Wall et al., 2014; Schobel et al., 2017; Bhardwaj and Biswal, 2019; Tiwari et al., 2020) and Malani Igneous Suite intruded along extensional fractures (Sharma, 2005).

We studied a part of the SDT near Beawar-Rupnagar-Babra in Rajasthan (**Figure 2A**). The SDT, in this part, is flanked by the pre-Delhi rocks in the east and west (Heron 1953). Later studies interpreted the pre-Delhi rocks in the western flank were completely metacratonized by the intrusion of ca. ≤0.87 Ga old granites (Gupta et al., 1997; Singh et al., 2020). Further, an inlier of pre-Delhi rocks, called Beawar gneiss, divides the SDT into NW and SE synclines (Heron, 1953). The Beawar gneiss is as old as ca. 2.8 Ga (Tobisch et al., 1994; detrital zircon ages range from 2.5 to 1.6 Ga; Kaur et al., 2019) and was overprinted by later thermal events at 0.96 and 0.89 Ga (Kaur et al., 2020). Our study belongs to the NW syncline that Heron (1953) further subdivided into Barotiya and Sendra sequences (**Figure 2A**). While Barotiya sequence is dominated by conglomerate, mica schist, and amphibolite, the Sendra sequence consists of calc schist and mica schist. Both have undergone NE-SW folding and greenschist facies metamorphism. Mylonite and cataclasite are developed along ductile shear zones and faults. Several granite plutons, namely, Sewariya, Pratapgarh, Sumel, Chang, and Sendra plutons, intrude the belt (**Figure 2A**) (Sendra granite, ca. 0.98 Ga, Gangopadhyay and Mukhopadhyay, 1984; Tobisch et al., 1994; Pandit et al., 2003; Sewariya granite, ca. 0.86 Ga, Sivasubramaniam et al., 2019).

GEOLOGICAL SETTING OF THE STUDY AREA-PRESENT STUDY

Field Setting

Mapping of litho-units and meso-microfabric study of rocks were carried out and the structural map of the area (Singh et al., 2020) was updated with addition of a greater amount of structural data and stereoplots for areas like large scale fold hinges and shear

TABLE 1 | Granite ages, from the SDT.

Name of the granite	Age	Method	References
Granites, Bilara near Jodhpur	1101 ± 13 Ma	Zircon 207Pb/206Pb	Meert et al. (2013)
Plagiogranite Sirohi Terrane	1015 Ma	SHRIMP Zircon dating	Dharma Rao et al. (2013)
Diorites, Ranakpur	1012 ± 78 Ma	Sm-Nd Isochron age	Volpe and Macdougall (1990)
Xenocryst granite gneisses of Sirohi	992 ± 1.3 Ma	Pb-Pb Zircon Xenocryst	Purohit et al. (2012)
Rhyolite, Deri	987 ± 6 Ma	U-Pb zircon age	Deb et al. (2001)
Foliated granite Sirohi Terrane	966 Ma	SHRIMP Zircon dating	Dharma Rao et al. (2013)
Rhyolite flows in Ambaji granite	960 Ma	SHRIMP Zircon dating	Singh et al. (2010)
Sendra granite	840 Ma	Rb-Sr age	Choudhary et al. (1984)
Sendra granite	967.8 ± 1.2 Ma	Pb/Pb ages	Pandit et al. (2003)
Sendra granite	966 Ma	Nd-Sm	Tobisch et al. (1994)
Chang pluton	970 Ma	U/Pb age	Tiwana et al. (2019)
Godhra pluton	955 Ma	Rb/Sr age	Gopalan et al. (1979)
Erinpura granites	863 ± 23	Monazite dating	Just et al. (2011)
Granulite metamorphism, anatexis Ambaji	860 Ma	SHRIMP Zircon dating	Singh et al. (2010)
Granite gneisses, Ambaji	850 Ma	Rb-Sr age	Choudhary et al. (1984)
Rapakivi granite intrusion, Ambaji granulite	840 Ma	SHRIMP Zircon dating	Singh et al. (2010)
Foliated granite, Siyawa	836+7/–5 Ma	U-Pb Zircon age	Deb et al. (2001)
Granites, Sirohi	822.8 ± 0.8 Ma	Pb-Pb Zircon age	Purohit et al. (2012)
Granite, Tosam	818 ± 3.6 Ma	Ar-Ar ages	Murao et al. (2000)
Porphyritic granite Sirohi Terrane	808 Ma	SHRIMP dating	Dharma Rao et al. (2013)
Rhyolite, Tosam	793 ± 18 Ma	Ar-Ar ages	Murao et at. (2000)
Malani Igneous Suite	771 Ma	U-Pb and 40Ar/39Ar	Meert et al. (2013)
Sindreth volcanic rocks	765.9 ± 1.6 Ma	U-Pb Zircon age	Van Lente et al. (2009)
Microgranite, Ambaji	765 Ma	Rb-Sr age	Choudhary et al. (1984)
Sindreth rhyolite Sirohi Terrane	765 Ma	SHRIMP Zircon dating	Dharma Rao et al. (2013)
Malani Igneous Suite	765 Ma	Zircon age	Dharma Rao et al. (2012)
Balda granites	763 ± 22 Ma	Whole Rock Rb-Sr age	Sarkar et al. (1992)
Microgranite, Ambaji granulite	759 Ma	SHRIMP Zircon age	Singh et al. (2010)
Charnockite, Ambaji granulites	757.8 ± 0.9 Ma	Single zircon age	Roy et al. (2005)
Mt Abu granite	735 ± 15 Ma	Rb-Sr age	Crawford (1975)
Gabbar Hill granite near Ambaji	535 ± 15 Ma	Biotite mineral isochron	Crawford (1975)
Mt Abu, fabric formation	509 ± 2 Ma	Ar-Ar, Hb crystallization	Ashwal et al. (2013)
Present study			
Sewariya granite (TKB-1)	878 ± 9 Ma	Zircon, SHRIMP	Intrusion, Age of D1
Xenocryst from Sewariya granite (TKB-1)	1634 ± 22 Ma	Zircon, SHRIMP	Basement metamorphism
Rupnagar metarhyolite (TKB-2)	982 ± 3 Ma	Zircon, SHRIMP	Intrusion
Pratapgarh granite (TKB-3)	992 ± 12 Ma,	Zircon, SHRIMP	Intrusion
Sumel granite (TKB-4)	946 ± 18 Ma	Zircon, SHRIMP	Intrusion
Sumel granite (TKB-4)	270 ± 12 Ma	Zircon, SHRIMP	Pb-loss
Pre-Delhi metamorphism	1611 Ma	Monazite dating	
D1 deformation metamorphism	865 – 846 Ma	Monazite dating	
D2 deformation and shearing	81a – 680 Ma	Monazite dating	
Brittle shearing	588 Ma	Monazite dating	

zones. Large scale structures were interpreted with the help of structural cross sections. Mica schist and calcareous schist are the major metasedimentary units in the area (**Figures 2B,C**). The mica schist is marked by close spaced schistosity (S_1) (**Figures 3A,B**) and calcareous schist contains rib structure produced by differential weathering between carbonate layer and silicate layers (**Figures 3C–H**). The calcareous schist grades into impure marble and calcareous quartzite. The impure marble carries bedding parallel epidote-garnet skarnoid bands as at Rupnagar (**Figure 3D**). Metaconglomerate formation having width ranging from m to 10 m occurs within mica schist, in the west of Babra (**Figure 2B**). The metaconglomerate consists of alternate mica schist and quartzite layers with several ellipsoidal quartzite and granite pebbles (**Figures 3I,J**). The Phulad thrust passes along the metaconglomerate formation and converted the rock into a micaceous mylonite. The pebbles and quartzite layers within the thrust are flattened and stretched down-dip, forming boudin, mullion, and rodding structures. Further, meter scale slivers of basement pelitic-gneissic rocks (**Figure 3K**) occur within the thrust zone; they carry garnet, tourmaline, quartzofeldspathic pockets, and sillimanite needles visible on the schistosity surface.

Concordant bands of metarhyolite and amphibolite occur within mica schist and calcareous schist (thickness varying from few cm to m) near Rupnagar and Babra (**Figures 2B,C**, **3L,M**). These rocks are marked by flow layers (S_0) and filled-in vesicles (**Figure 3M**).

Several deformed granite plutons occur in the area, namely, Sendra, Chang, Pratapgarh, Sumel, and Sewariya plutons (**Figures 2A–C**). Heron (1953) included all of them within Erinpura granite while later workers (Bhattacharjee et al., 1993; Gupta et al., 1997; Pandit et al., 2003) classified them

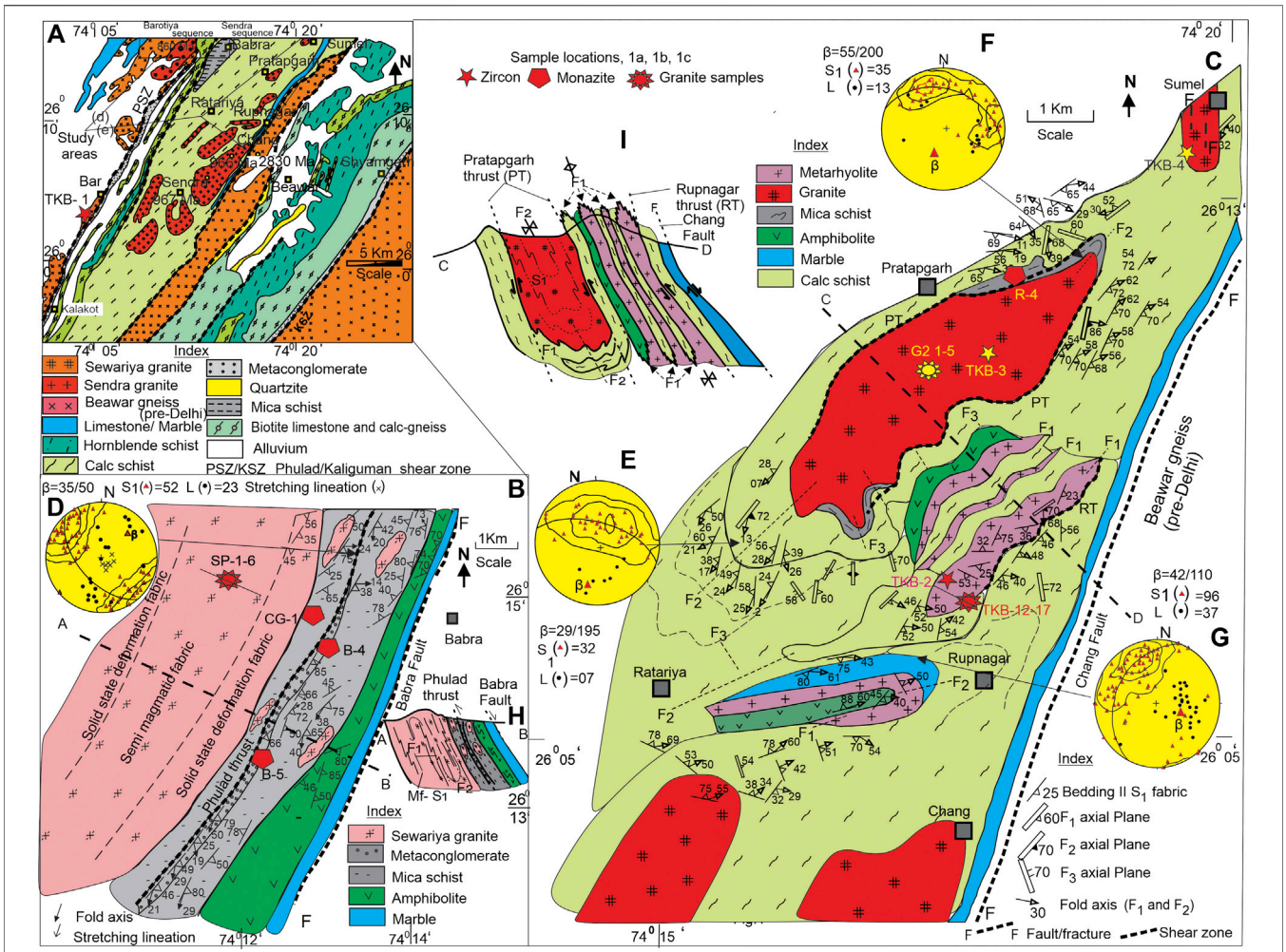

FIGURE 2 | (A) Geological map of the SDT around Beawar-Rupnagar-Babra; pre-Delhi gneiss outcrop exposed around Beawar, called Beawar gneiss, divides the SDT into NW and SE syncline. The study areas (marked by polygons) lie in the NW syncline around Babra and Rupnagar. **(B)** Geological map of the area west of Babra. **(C)** Geological map of the area west of Rupnagar. **(D–G)** Stereoplots of the S_1 fabric, F_1-F_2 axis, stretching lineation. **(H–I)** Geological cross sections. Sample locations are marked in the geological map, PT: Pratapgarh thrust, RT: Rupnagar thrust Geological Setting of the Study Area-Present Study.

into Sendra granite (Sendra, Chang, Pratapgarh, and Sumel pluton) and Erinpura granite (Sewariya pluton). Field relation suggests that the Sewariya granite is the youngest as its apophyses crosscut the metasediments as well as other granite plutons (**Figures 3F,N**). The Pratapgarh and Sumel plutons are coarse grained with prominent NE-SW trending S_1 fabric; it carries several metasedimentary and metavolcanic roof pendants and xenoliths which are folded and metamorphosed along with the pluton (**Figure 3N**). Sewariya pluton occurs as a linear body in the western part of the area (**Figures 2A,b**) containing magmatic/semimagmatic (S_m) and solid state deformation fabric, S_1 (**Figures 3O,Q**). Tourmalines are segregated into ellipsoidal to ribbon shape pockets (**Figure 3R**-inset 1) and amphibolite-mica schist xenoliths are more common in the central part of the Sewariya granite (**Figure 3R**-inset 2). The pluton shows distinct textural variation from core to the margin (**Figure 3R**). The core part of the pluton is characterized by magmatic/submagmatic fabric (S_m) due to shape preferred alignment of quartz, plagioclase, and K-feldspar minerals (**Figure 3R**). It is coplanar with S_1 fabric albeit the S_1 fabric anastomoses around the coarse grains of feldspar and quartz. The pluton exhibits an increase in intensity of deformation from core to the margin. The granite converts to a quartzofeldspathic gneiss near the host rock contact (**Figure 3R**). The pluton and host rock fabric are coupled as the S_m parallel S_1 fabric in the granite is coplanar with the S_1 fabric in the host rock and together participated in subsequent folding. This evidences the syntectonic emplacement of granite with D_1 deformation (cf. Vernon et al., 1989; Bouchez et al., 1990; Miller and Paterson, 1994; Paterson et al., 1998; Buttner, 1999; Biswal et al., 2007). Such gneisses occur at several places, e.g., Kalakot, Bar, and Babra, which were earlier identified as pre-Delhi gneiss (**Figure 2A**, Heron, 1953). At Bar (near Makarwali village, **Figure 2A**), there is a spectacular gradation of mica schist into granite gneiss. The mica schist contains quartzofeldspathic layers derived from lit-par-lit injection of Sewariya granite pluton; the

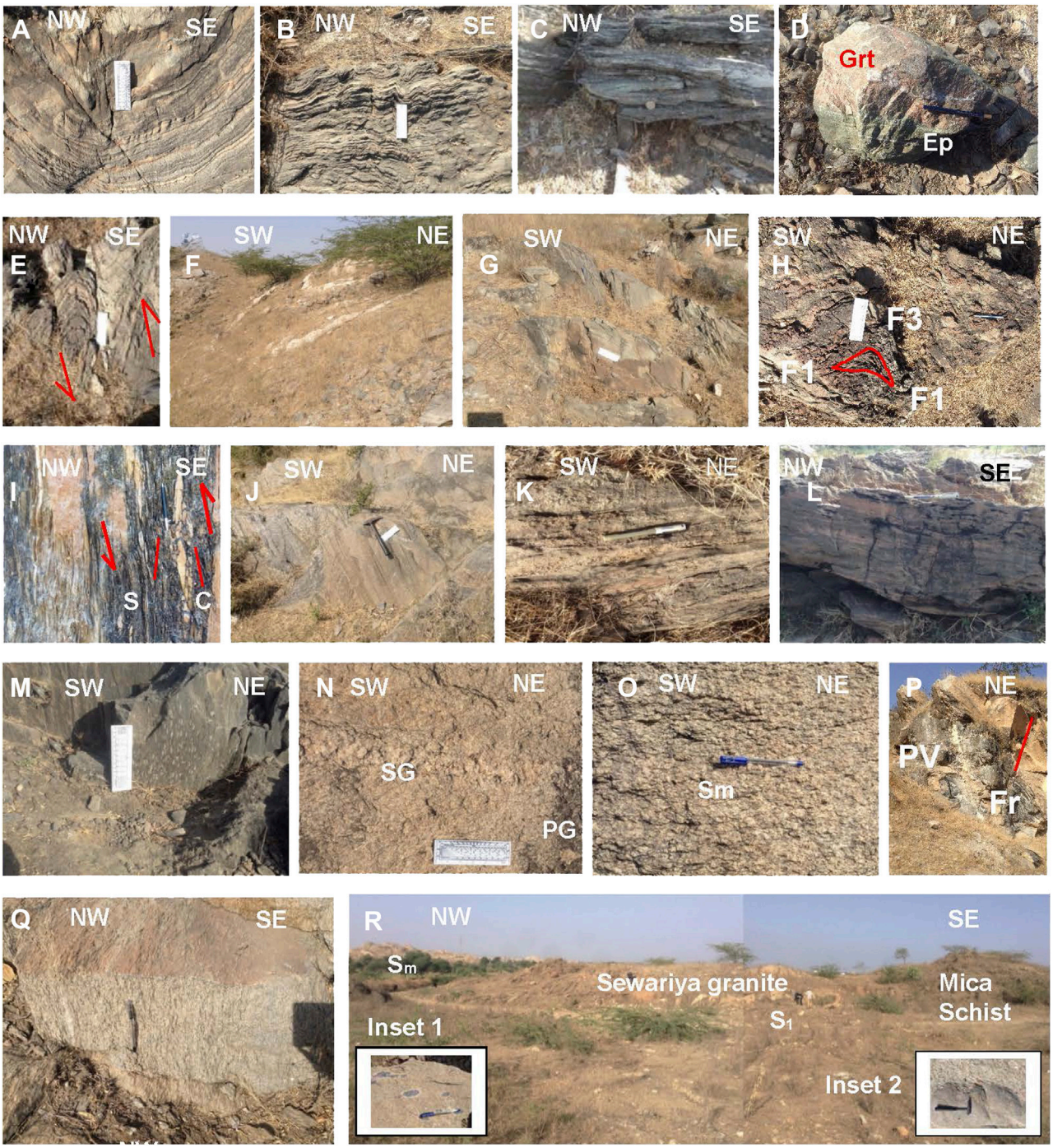

FIGURE 3 | (A) Mica schist, showing hinge zone of a large scale F_1 fold, S_1 fabric (scale parallel) is developed parallel to the axial plane of the fold, S_1 fabric crosscut the S_0 (bedding, color bandings), subhorizontal view, Rupnagar. **(B)** Mica schist showing crenulation cleavage (scale parallel) due to folding of S_1 by upright F_2, Rupnagar. **(C)** Calc schist showing recumbent F_1 fold (coins at the F_1 hinge), vertical view, Pratapgarh. **(D)** Epidote (Ep) garnet (Grt) skarnoid near Rupnagar. **(E)** Calc schist/impure marble showing upright F_2 fold, having axial plane parallel shear (NW vergence thrust, scale parallel), vertical view, Rupnagar. **(F)** Calc schist with Sewariya granite vein, folded by NNW-SSE trending F_3 fold (scale parallel), horizontal view, Pratapgarh. **(G)** Dome structure (type 1) due to interference between NE trending F_2 and NW trending F_3 folds, in calc schist, vertical view near Pratapgarh. **(H)** Crude type 2 int pattern due to F_3 (scale parallel) superimposed on F_1 near Rupnagar. **(I)** Metaconglomerate formation, sheared at the center, S-C fabric has small internal angle (15°), NW vergence thrusting, vertical view, Babra. **(J)** Mylonite surface, subvertical stretching lineation (hammer parallel) and low plunging intersection lineation (scale parallel), vertical view, Babra. **(K)** Garnet, staurolite, sillimanite bearing pockets within metaconglomerate, horizontal view, Babra. **(L)** Alternate metarhyolite (pink colored) and amphibolite layers (green colored), vertical view, Rupnagar. **(M)** Amphibolite carrying vesicles (white pockets), vertical view, Rupnagar. **(N)** Pratapgarh granite course grained (PG), intruded by Sewariya granite vein (SG), horizontal view, near Pratapgarh. **(O)** Sewariya granite from the core of the pluton showing magmatic fabric S_m, pen parallel, west of Babra. **(P)** Faulted rock along Chang fault, north of Rupnagar, brittle fractures (Fr) are present along which thin pegmatite veins are present (PV). **(Q)** Sewariya granite with solid state deformation fabric, S_1, close to the host rock contact. **(R)** Landscape view of Sewariya granite near Babra, on the NW side, in the core of the pluton, magmatic/submagmatic fabric, S_m, is more prominent and in the SE side near mica schist contact, solid state S_1 fabric is more prominent (scale parallel) (width of the photograph 2 km).

quartzofeldspathic layers increase in number and thickness and grade into granite gneiss.

Textural Study

Mica schist contains alternate thin quartzofeldspathic and micaceous bands, and the muscovite and biotite show shape preferred orientation defining the S_1 fabric in the rock (**Figure 4A**). The calcareous schist carries layers of tremolite-actinolite with shape preferred orientation parallel to S_1 (**Figure 4B**). Occasionally, plagioclase and epidote porphyroblasts with inclusions of tremolite and actinolite occur in the rock. The tectonic slivers within metaconglomerate contain garnet, staurolite, tourmaline, quartz, feldspar, and ± sillimanite assemblage (**Figure 4C**). Along the thrusts, micaceous mylonite is developed that contains quartz ribbons which are recrystallized into smaller grains (**Figure 4D**). Further, the tectonic slivers show tailed garnet and staurolite grains (**Figures 4E,F**) and the rock shows retrogression of sillimanite to muscovite and staurolite to biotite (**Figure 4E**).

The metarhyolite comprises quartz (40–50%), plagioclase (30–40%), hornblende, and epidote; the grain size varies between 100 and 120 μm (**Figure 4H**). Hornblende is euhedral and shows shape preferred orientation parallel to S_1 fabric. Epidote is produced from retrogression of hornblende during shearing (**Figure 4G**). Plagioclase retains its euhedral shape characteristic of magmatic origin. Quartz is subrounded and show bulging grain margin indicating low temperature dynamic recrystallization. Amphibolite shows granoblastic to well-foliated character (with S_1 fabric) and contains hornblende-epidote-biotite-quartz-plagioclase minerals (**Figure 4I**).

The Pratapgarh pluton is coarse grained containing microcline, quartz, and plagioclase that show an equigranular mosaic (grain size 450–500 μm) (**Figure 4J**). Biotite, muscovite, and rare garnet, sillimanite, and tourmaline are present in the rock; garnet and sillimanite represent the undigested phases. Microcline and plagioclase maintain euhedral shape, and the polysynthetic lamella in plagioclase is in random orientation to suggest the absence of any magmatic fabric in the rock. However, the rock shows low temperature deformation fabric indicated by bulging recrystallization of quartz and shape preferred orientation of mica minerals parallel to S_1 fabric. The Sumel pluton is inequigranular, coarse grained, and porphyritic containing plagioclase phenocrysts in the groundmass of K-feldspar, quartz, tourmaline, and biotite. Plagioclase still preserves euhedral shape indicating magmatic origin (**Figure 4K**). Biotite shows shape preferred orientation defining deformation fabric (S_1) in the rock. The pluton is marked by N-S trending pegmatite veins intruded along fractures and ductile shear zones. Absence of magmatic fabric and development of greenschist facies deformation fabric (S_1) similar to the metasediments point toward pre-D_1 intrusion of these plutons.

The Sewariya granite is coarse grained and consists of quartz, K-feldspar, plagioclase, muscovite, biotite, and tourmaline. The magmatic/submagmatic fabric S_m is best visible on the polished surface of the sample, having been defined by alignment of longer dimension of the euhedral plagioclase and K-feldspar crystals (**Figure 4L**). Some grains are oriented at an angle probably due to lack of space for rotation during flow of magma (cf. Bouchez et al., 1990). Under microscope the twin planes of these minerals are oriented parallel to the S_m. The K-feldspar and plagioclase phenocrysts contain mica inclusions in mutually perpendicular orientation, one parallel to cleavage and the other perpendicular to it (**Figure 4M**). Surrounding the feldspar phenocrysts, smaller quartz grains are dynamically recrystallized, which are characterized by chess board twinning and grain boundary migration. Plagioclase and K-feldspar occasionally show dynamic recrystallization into smaller grains (**Figure 4N**). Toward the margin of the pluton, the rock exhibits increase in degree of dynamic recrystallization and segregation into alternate quartzofeldspathic and mica rich bands (**Figures 4O,P**). Smaller grains of plagioclase, K-feldspar, and quartz are developed out of such dynamic recrystallization; quartz shows chess board twinning; all these features indicate higher temperature of deformation at about 650–700 °C (cf. Stipp et al., 2002; Passchier and Trouw, 2005).

Structures

Three stages of ductile deformation ($D_{1\text{-}3}$) and one stage of brittle deformation (D_4) affected the rocks. The D_1 deformation produced cm to m scale NE-SW axial oriented tight to isoclinal recumbent/reclined to upright F_1 folds (**Figures 3A,C**). These are developed not only in the metasediments but in the amphibolite, metarhyolite, and granite also. Due to syn-D_1 greenschist facies metamorphism (M_1), pervasive F_1 axial planar schistosity (S_1, **Figures 3A,B**) and intersection lineation between bedding and S_1 fabric (**Figure 3A**) are developed in all the rock types. The D_2 deformation developed cm to 10 m scale NE-SW trending upright F_2 folds (**Figures 3B,E**) coaxially with the F_1 (type 3 interference pattern, Ramsay, 1967). Crenulation cleavage and pucker axes associate with the F_2 fold (**Figures 3B** and **4B**) and axial planar thrusts were developed (**Figure 3D**). The F_2 fold bears testimony of buckling (parallel folding, disharmonic folding, etc., **Figure 3B**) and was ascribed to a NW-SE horizontal compression during D_2. The D_3 developed m to 10 m scale NW-SE to N-S trending F_3 folds, attributed to NE-SW shortening of the orogen (**Figure 3F**). Type 1 (**Figure 3G**) and type 2 interference patterns (**Figure 3H**) were produced due to superposition of F_3 on the F_2 and F_1 folds, respectively. Ductile deformation was followed by brittle deformation (D_4) which is represented by N-S and NNE-SSW brittle fractures; late-stage pegmatite veins intrude the fractures at places (**Figure 3P**).

Several NE-SW trending F_1 folds are mapped in the metarhyolite-amphibolite-calc schist sequence to the north of Rupnagar (**Figure 2C** and profile section **Figure 2I**); the S_1 fabric crosscut the litho-units at the F_1 hinge zone. The F_1 axial planes are refolded by NW-SE trending F_3 fold to produce type 2 interference pattern in map scale. Further, to the west of Rupnagar, the F_1 folds in marble-metarhyolite-amphibolite sequence are refolded by an F_2 fold producing type 3 interference pattern which is indicated by girdle distribution of S_1 fabric in stereoplot; the β axis lies in ESE direction (**Figure 2G**).

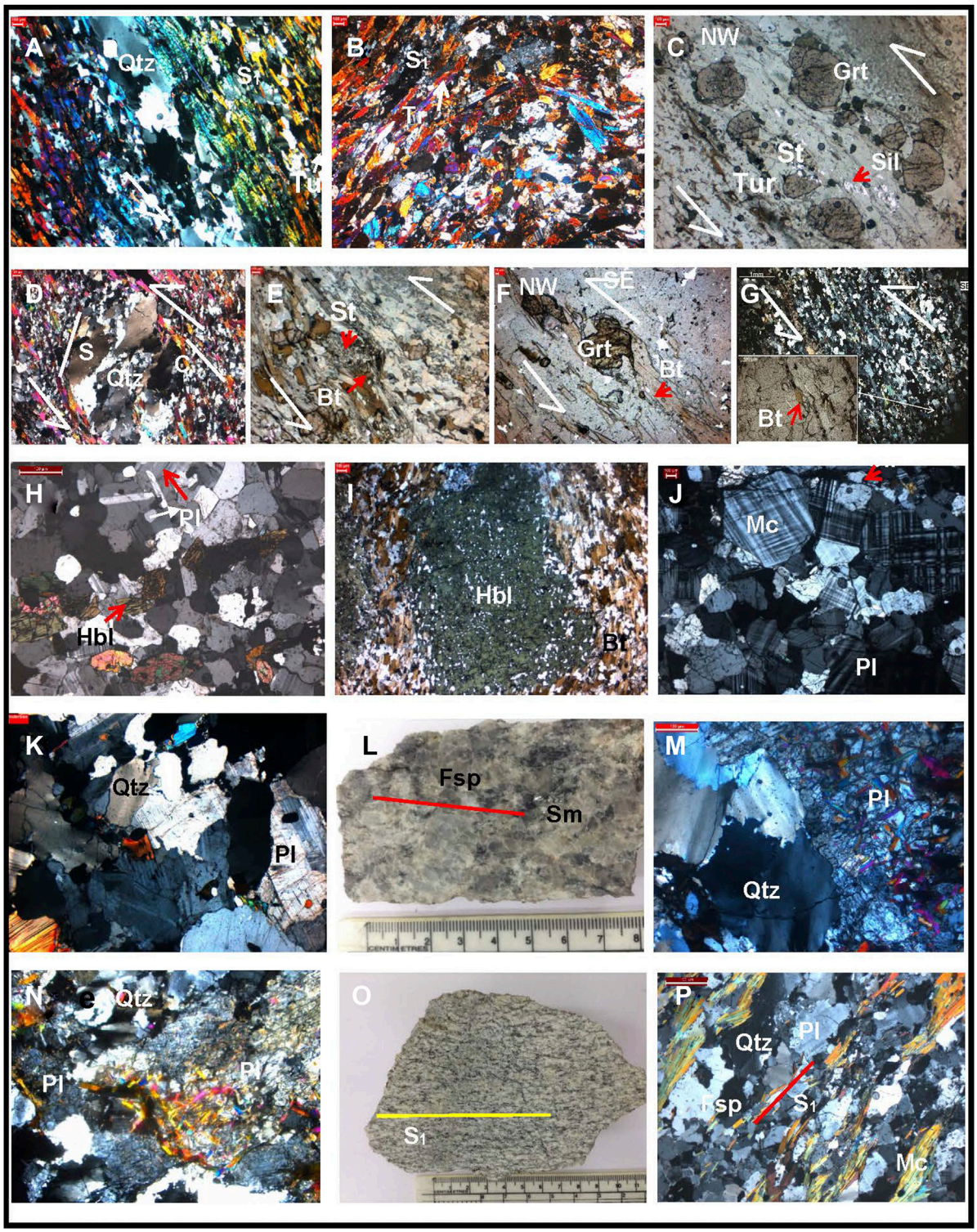

FIGURE 4 | Photomicrographs: **(A)** Mica schist with alternate muscovite + biotite and quartz rich layers, parallel to S_1. **(B)** Calc schist with tremolite, arranged parallel to S_1, the S_1 is folded by F_2 fold. **(C)** Garnet (Grt), staurolite (St), sillimanite (Sil), and tourmaline (Tur) assemblage in pelitic gneiss-tectonic slivers within metaconglomerate formation. Due to shearing along Phulad thrust, garnets show rotation in top-to-NW reverse sense. **(D)** Mica mylonite from Pratapgarh thrust, the quartz (Qtz) shows dynamic recrystallization, S fabric is indicated by long axis of the quartz, top-to-NW reverse sense of shearing, S^C is nearly 60° suggesting volume gain. **(E)** Staurolite changing to biotite (Bt) during shearing, Biotite is grown in the strain shadow of the staurolite porphyroclast, top-to-NW reverse sense of shearing. **(F)** Garnet porphyroclasts in the Phulad thrust show top-to-NW reverse slip, biotite develops in the tail of the porphyroclast, relict sillimanite (Sil) is present. **(G)**

(*Continued*)

FIGURE 4 | Epidote-biotite mylonite developed on metarhyolite, along Rupnagar thrust, top-to-NW shearing, inset shows detailed view of the biotite fish that indicates NW vergence shearing. **(H)** Rupnagar metarhyolite, medium grained, quartz shows bulging, magmatic hornblende (Hbl), plagioclase (Pl) are preserved. **(I)** Amphibolite with hornblende porphyroblast (Hbl) and biotite. **(J)** Pratapgarh granite coarse grained preserves magmatic microcline (Mc) and plagioclase (Pl). **(K)** Sumel pluton shows coarse grained, plagioclase (Pl) shows magmatic habit, quartz shows undulose extinction. **(L)** Sewariya granite, polished sample, Feldspar (Fsp) grains show magmatic fabric (S_m). **(M)** Thin section prepared from sample I, coarse plagioclase contains biotite inclusions, surrounding quartz grains show chess board extinction. **(N)** Thin section of Sewariya granite shows dynamic recrystallization of quartz, feldspar, and plagioclase surrounding coarse plagioclase grain. **(O)** Polished hand specimen of gneissic part of Sewariya granite close to country rock, solid state fabric S_1. **(P)** Thin section of the sample o, solid state fabric S_1 is prominent, mica (Mc) recrystallized parallel to it. Quartz (Qtz), K-feldspar (Fsp), and plagioclase (Pl) are dynamically recrystallized. Quartz shows chess board extinction.

The F_1-F_2 axes are rotated from NE direction toward ESE direction by the F_3 fold. Further, F_2 folds are present to the NE of Ratariya and Pratapgarh in the calc and mica schist units; the core of the fold is occupied by the Pratapgarh granite pluton (profile section **Figure 2I**). The F_1 fold and S_1 fabric in metasediments as well as in the granite are refolded around the hinge zone of the F_2 fold. The axis of the fold is oriented toward SSW as indicated by the β axis in stereoplot (**Figures 2E,F**). The lineation plots do not coincide with the β axis suggesting that the lineations are rotated to a large extent by the F_3 fold. The entire structure surrounding the Pratapgarh pluton represents dome and basin structure in large scale. In addition, the mica schist amphibolite sequence describes large scale F_2 fold with NNE-SSW trending β axis to the west of Babra (**Figure 2D**, structural profile **Figure 2H**). The stereoplot shows an incomplete girdle suggesting either F_2 hinges are too tight or they are obliterated by thrusting. The lineations in the stereoplot show concentration in NE as well as SW quadrant indicating plunge reversal due to the F_3 folding. In this domain, the Sewariya pluton is marked by F_1 fold and S_1 fabric. The S_1 fabric remains parallel with the litho-contact between the pluton and mica schist as well as the S_1 within mica schist. In both the mapped areas, west of Babra as well as around Rupnagar (**Figures 2B,C**), the litho-units are marked by multiple phases of folding; coaxial folding is predominant. Therefore, the S_1 fabric shows girdle distribution in stereoplots (**Figures 2D–G**). But the profile sections (**Figures 2H,I**) show uniform dip toward SE. This is interpreted as due to the effect of NW verging thrusts on large scale structure of the area.

Further, the map depicts large scale D_2 thrusts at several localities, in form a retro-wedge thrust belt (Sections A-B and C-D, **Figures 2H,I**, cf. Naylor and Sinclair, 2008). The most prominent amongst them is Phulad thrust passing along the metaconglomerate-mica schist formations west of Babra (**Figure 2A**). The thrust is marked by quartz-biotite mylonite with crudely defined S-C fabric (**Figure 3I**). The mylonitic foliation dips to SE and the stretching lineation is nearly down-dip (**Figure 2D**, **3J**). The stretching lineation is defined by muscovite and biotite minerals. The conglomerate pebbles are stretched parallel to stretching lineation. Apart from that, large number of boudins (**Figure 3I**), mullions, and rodding of quartzite, granite, and gneisses associate with stretched pebbles. These boudins are long drawn out on both vertical and horizontal section; vertical stretched axis is 5–10 times longer than the horizontal stretched axis. Though the boudin long axes are parallel with the mylonitic foliation, these are tilted with a smaller angle with mylonitic foliation (~15°) nearly in more than 50% of cases (**Figure 3I**). The boudins can be classified as symmetrical-drawn boudins to asymmetrical-shear boudins (cf. Goscombe et al., 2004) suggesting effect of vertical shearing in the formation of boudin structures. As the boudins are detached both horizontally and vertically, they can be termed as chocolate boudins (Ghosh, 1988). Vertical shearing with large component of pure shear component during D_2-thrusting has flattened the boudins and pebbles and made them near parallel to the mylonitic foliation (**Figure 3I**, Dasgupta et al., 2012). A low plunging intersection lineation between S and C fabric is developed on C-surface in a few instances (**Figure 3J**). The lensoidal quartz aggregates show dynamic recrystallization of quartz grains by subgrain rotation; the quartz grains are oriented at an angle to the mylonitic foliation (C). Temperature of deformation is around 450°C (e.g., Stipp et al., 2002). Lensoidal quartz aggregates, mica fishes, and S-C fabric on the XZ section of the mylonites indicate top-to-NW sense of thrust-slip kinematics (**Figure 3I**). The upper amphibolite grade tectonic slivers contain several rounded garnet and tourmaline grains. Garnet contains quartz-biotite inclusion trails (**Figure 4C**). The orientation of such inclusion trails varies from grain to grain suggesting variable amount of rotation of host garnet grains during D_2 shearing. Sillimanite and staurolite grains are retrogressed during shearing to muscovite and biotite to form porphyroclastic tail in the strain shadow zone of the garnet (**Figures 4C,E,F**). The sigma type garnet porphyroclasts indicate top-to-NW vergence thrusting (**Figures 4C,E–G**). In addition, a pair of thrusts occurs on western and eastern edge of the Pratapgarh granite pluton, both jointly named as Pratapgarh thrust. The western thrust passes through the mica schist. The lensoidal aggregate contains dynamically recrystallized quartz grains (**Figure 4D**). These grains show top-to-NW thrust sense of shear. The S fabric is at high angle (60°) to C fabric, which suggests there is volume gain during thrusting due to fluid injection (e.g., Ramsay and Huber, 1987). Rupnagar thrust occurs on the eastern edge of the metarhyolite formation (**Figure 2A**). The metarhyolite is sheared and produced muscovite-biotite-quartz-epidote assemblage. The mylonite contains SE plunging stretching lineations, and the S-C fabric indicates top-to-NW thrusting (**Figure 4G**). In addition to these ductile shear zone, brittle fault, namely, Chang fault, occurs at the contact between the pre-Delhi granite gneiss and metasedimentary sequence east of Rupnagar and Babra fault, west of Babra. The fault zone is marked by crushed rock of the amphibolite and marble (**Figure 3P**).

Metamorphism

The rock types show greenschist facies metamorphism. Mica schist and calcareous schist contain muscovite, biotite,

tremolite-actinolite, and epidote minerals characteristic of greenschist facies assemblage (**Figures 4A,B**). Interbedded metarhyolite contains quartz grains which show bulging; plagioclase and K-feldspar still preserve magmatic habit (**Figure 4H**); the amphibolite band consists of hornblende, albite, and epidote (**Figure 4I**). Pratapgarh-Sumel granite shows growth of mica and grain boundary migration in quartz; feldspar retains magmatic habit (**Figure 4J**). All these corroborate to greenschist facies of metamorphism that represents the peak metamorphism in the area (M_1) syntectonic with the D_1 deformation. The Sewariya granite shows dynamic recrystallization of plagioclase and K-feldspar (**Figures 4M,N,P**) indicating higher temperature of metamorphism (M_1), nearly 700°C (Pryer, 1993; Kruhl, 1996; Rosenberg and Stuniz, 2003), but under similar pressure condition as greenschist facies. The D_2-D_3 indicates greenschist facies metamorphic condition. This is indicated by the crystallization of mica along the axial plane of the folds. The pelitic gneiss slivers within metaconglomerate show upper amphibolite facies metamorphism as they contain garnet-staurolite-tourmaline-quartz-feldspar-sillimanite assemblage (**Figures 4C,E,F**). During D_2 shearing, fluid activity along the thrust retrograded sillimanite to muscovite, staurolite to biotite, and hornblende to epidote (**Figures 4E–G**).

MATERIALS AND METHOD FOR GEOCHEMISTRY AND GEOCHRONOLOGY

Principle

Geochronology, geochemistry, and tectonic fabric of a granite serve as important proxies for dating an orogeny. For example, rifting of continent creates synsedimentary bimodal volcanism and granite intrusion in the basin (e.g., New England Orogen, Allen et al., 1998; Liu and Han, 2019). Further, when the basin closes through subduction/collision the rocks undergo high grade metamorphism and melting at depth producing synorogenic granites (Finnacca et al., 2019). Postorogeny granite is emplaced in extensional setting (Pearce, 1996; Zhang et al., 2018). Granites intruding at different period of orogenesis are distinguished by their geochemical signature and tectonic fabric. For instance, the preorogenic granite reflects extensional or rift setting geochemistry and it undergoes ductile deformation recording multiple solid state deformation fabric during orogenesis. Synorogenic granite shows S type geochemistry and contains magmatic/semimagmatic fabric coupled with solid state deformation fabric (Bouchez et al., 1990; Chappell and White, 1992; Paterson et al., 1998). Postorogenic granite lacks solid state deformation fabric. The granites are dated by zircon geochronology because zircon has the higher closure temperature to U-Th -Pb system (>900°C.; Dahl, 1997; Cherniak and Watson, 2001). However, zircon cannot reset the age in response to low temperature shearing. For dating fluid induced low temperature deformation, monazite geochronology is most suitable. Monazite crystallizes in response to fluid activity (alkali rich) at different period of deformation and develops compositional domains corresponding to each phase of growth (Williams and Jercinovic, 2002; Pyle et al., 2003; Foster et al., 2004; Mahan et al., 2006). As the closure temperature of monazite for Th-U-total Pb is ca. 800 °C, each domain retains its age of formation and can be used as geochronometer (Cherniak et al., 2004; Cherniak and Pyle, 2008).

Geochemistry

Geochemistry of granite and metarhyolite was carried out with 15 samples collected at 100 m interval across the strike of the pluton (**Figures 2B,C**). Major elements were analyzed for all samples; however, trace element for seven samples was carried out in an ICP-AES (ARCOS, Simultaneous ICP Spectrometer) at the Sophisticated Analytical Instrument Facility, Indian Institute of Technology, Bombay, adopting the following procedure, and discriminatory diagrams were plotted (**Table 2**, **Figure 5**). A 0.25 g of powdered sample was fused with 0.75 g lithium metaborate and 0.50 g lithium tetraborate in platinum crucibles at a temperature of 1,050°C in a muffle furnace. After cooling, the crucible was immersed in 80 ml of 1 M HCl contained in a 150 ml glass beaker and then magnetically stirred until the fusion bead dissolved completely. Then the sample volume was made up to 100 ml in a standard volumetric flask. The same procedure was adopted to make standard solutions and blank sample. The standards used for the analyses include BIR-1 (Basalt), BHVO-2 (Basalt), BCR-2 (Basalt), AGV-2 (Andesite), and GSP-2 (Granodiorite) (USGS Reference standards, 2005). Major and trace elements and LOI were estimated from the above solution by ICP-emission spectrometry.

Zircon U-Pb Geochronology

Zircon geochronology is performed on four granite and metarhyolite samples, collected one from each pluton (Sewariya pluton, near Bar, **Figure 2A**, Sample No TKB-1; Rupnagar metarhyolite, Sample No TKB-2; Pratapgarh pluton, Sample No TKB-3; Sumel pluton, Sample No TKB-4, **Figures 2B,C**). Textural study of zircon was carried out on CL images (**Figure 6**). Magmatic zircon was distinguished by its euhedral shape with rings, from xenocrystic zircon that has irregular geometry (Biswal et al., 2007). A U-Pb isotope of the zircon was estimated on the SHRIMP ion microprobe at the John de Laeter Center for Mass Spectrometry at Curtin University in Perth, Australia. Zircon of all shapes and sizes was handpicked and mounted in epoxy resin together with natural zircon standard BR266 (Stern, 2001), TEMORA-2 (Black et al., 2003, 2004), and CZ3 (Pidgeon et al., 1994). The samples were loaded in the SHRIMP sample lock 24 h prior to analysis and pumped to ~5 × 10–7 Torr to allow degassing. Analytical procedure of the SHRIMP follows methods as described in detail by Claoue-Long (1994). Working conditions for both sessions included a primary beam current of 2–3 nA, slightly elliptical spot size of ~25–30 μm, the sensitivity of >20 counts per ppm Pb and per nA primary beam current, and a mass resolution of >4,500. Measurements were conducted on Zr2O+, 204Pb+, background, 206Pb+, 207Pb+, 208Pb+, 238U+, 232ThO+, and 238UO2 + in sets of six scans, with a total analysis time of about 15 min per sample spot. Analyses of unknown and BR266 standard zircon were interspersed at a ratio 3:1, allowing calibration of 238U/206Pb

TABLE 2 | Major element geochemistry of the granites. Few samples have been analyzed for trace elements. LOI is negligible (<0.001%).

	TKB12	TKB13	TKB14	TKB16	TKB17	1G2	2G2	3G2	4G2	5G2	SP1	SP3	SP4	SP5	SP6
LOCATION	**Rupnagar metarhyolite**					**Pratapgarh granite**						**Sewariya granite**			
SiO2	78.126	70.652	70.527	76.597	74.551	75.512	75.683	76.523	76.318	75.316	75.476	73.318	75.827	76.296	78.683
TiO2	0.126	0.27	0.378	0.037	0.018	0.038	0.044	0.033	0.032	0.034	0.09	0.249	0.139	0.14	0.176
Al2O3	10.688	15.832	15.126	11.559	12.621	12.835	12.266	12.48	12.589	12.872	12.786	13.733	12.452	12.247	10.814
Fe2O3(t)	0.91	0.855	0.408	0.989	0.731	0.674	0.921	0.585	0.519	0.759	0.813	1.038	0.74	0.975	0.921
MnO	0.017	0.017	0.008	0.018	0.009	0.052	0.057	0.043	0.047	0.053	0.023	0.033	0.024	0.016	0.03
MgO	0.244	0.304	0.286	0.167	0.157	0.058	0.055	0.051	0.05	0.044	0.196	0.571	0.219	0.215	0.284
CaO	0.479	0.338	1.279	0.056	0.129	0.792	0.772	0.797	0.806	0.758	0.533	1.612	0.822	0.466	0.686
Na2O	4.533	4.328	5.595	5.891	5.599	3.751	3.812	3.928	3.834	3.853	2.762	3.178	2.847	2.165	2.497
K2O	3.868	6.394	5.376	3.677	5.174	4.928	4.537	4.377	4.756	4.779	5.543	4.022	5.274	5.406	3.922
P2O5	0.008	0.008	0.017	0.009	0.009	0.012	0.011	0.011	0.01	0.013	0.151	0.17	0.173	0.121	0.144
LOI	0.43	0.61	0.51	0.16	0.11	0.26	0.14	0.36	0.11	0.28	0.53	0.54	0.47	0.99	0.47
SUM	99.429	99.608	99.51	99.16	99.108	98.912	98.298	99.188	99.071	98.761	98.903	98.464	98.987	99.037	98.627
CIPW															
Quartz	37.88752	10.99853	15.53595	33.06094	27.45183	33.12	34.6	35.23	34.23	32.97	37.21	35.62	37.48	41.98	47.64
Anorthite	0	0	0.256329	0	0	0	0	0	0	0	0	0	0	0	0
Na2SiO3	0.443306	0	0	1.772851	2.062275	0	0	0	0	0	0	0	0	0	0
Acmite	2.632737	1.698851	0	2.864186	2.111976	0	0	0	0	0	0	0	0	0	0
Diopside	1.289501	0.591337	1.558147	0.133484	0.427471	0	0.32	0.27	0.27	0	0	0	0	0	0
Sphene	0.263727	0.607271	0.904838	0.042878	0.021439	0	0	0	0	0	0	0	0	0	0
Hypersthene	0	0.473099	0	0.361549	0.200356	0.07	0	0	0	0.1	0.5	1.42	0.55	0.55	0.7
Albite	33.43823	34.71066	47.38544	38.97099	36.12746	35.37	35.21	36.73	35.51	36.28	25	33.78	27.07	19.91	23.66
Orthoclase	22.87025	49.58176	31.79379	21.74742	30.55276	29.13	26.83	25.88	28.13	28.25	32.74	23.76	31.14	31.97	23.17
Wollastonite	0	0	1.117903	0	0	0	0.16	0.03	0.21	0	0	0	0	0	0
Apatite	0.023169	0.023169	0.046339	0.023169	0.023169	0.02	0.02	0.02	0.02	0.02	0.35	0.39	0.39	0.28	0.32
Ilmenite	0.042783	0.042783	0.021391	0.042783	0.021391	0.08	0.08	0.06	0.06	0.06	0.04	0.06	0.04	0.04	0.06
Corundum	0	0	0	0	0	0	0	0	0	0	1.65	1.63	0.97	2.26	1.53
Rutile	0	0	0	0	0	0	0	0	0	0	0.07	0.22	0.12	0.12	0.15
Hematite	0	0.272796	0.41	0	0	0.64	0.86	0.56	0.47	0.71	0.81	1.04	0.74	0.98	0.92
Magnetite	0	0	0	0	0	0.05	0.08	0.04	0.08	0.08	0	0	0	0	0
SUM	98.89123	99.00026	99.03013	99.02026	99.00013	98.48	98.16	98.82	98.98	98.47	98.37	97.92	98.5	98.09	98.15
A/NK	0.917054	#DIV/0!	1.005838	0.844858	0.851298	1.114304	1.095718	1.113122	1.09772	1.116922	1.210947	1.431621	1.196545	1.299022	1.29296
A/CNK	0.853185	#DIV/0!	0.870921	0.838606	0.838016	0.99028	0.973444	0.985519	0.973147	0.99743	1.108981	1.096118	1.046049	1.191731	1.124905
Na2O/K2O	1.171923	0.676885	1.040737	1.602121	1.082141	0.761161	0.840203	0.897418	0.80614	0.806236	0.498286	0.790154	0.539818	0.400481	0.636665
Trace elements															
Sc	7.384	9.284	8.776	10.555	5.775	3.221	2.665	3.618	3.599	3.471	2.445	4.73	2.823	2.793	3.461
Cr	285.071	332.427	188.665	259.347	166.635	ND	ND	ND	ND	ND	ND	ND	ND	ND	ND
Ni	0	162.717	0	0	55.31	ND	ND	ND	ND	ND	ND	ND	ND	ND	ND
Cu	182.216	112.515	199.345	0	0	ND	ND	ND	ND	ND	ND	ND	ND	ND	ND
Zn	126.639	138.276	0	0	0	54.326	41.451	38.787	37.017	40.96	46.628	57.674	56.232	58.329	65.825
Rb	96.495	205.082	122.232	103.374	142.536	119.429	122.329	ND	ND	ND	ND	ND	ND	ND	ND
Sr	74.883	162.463	170.489	4.963	5.551	23.97	16.476	14.568	17.496	16.526	11.374	48.241	3.038	13.344	0.933
Y	70.464	74.695	50.537	69.944	37.433	91.352	82.352	ND	ND	ND	ND	ND	ND	ND	ND
Zr	386.648	638.98	670.185	100.038	76.231	48.759	51.271	36.238	43.722	43.943	29.725	130.46	59.312	69.237	92.05
Nb	13.125	12.021	11.862	12.069	11.659	12.365	12.621	ND	ND	ND	ND	ND	ND	ND	ND
Ba	574.892	1,498.938	1,115.323	453.445	599.166	475.123	475.123	ND	ND	ND	ND	ND	ND	ND	ND
Th	24.9	30.258	14.419	5.881	5.722	1.54	1.53	ND	ND	ND	ND	ND	ND	ND	ND
La	46.218	34.162	12.442	9.52	2.782	13.498	12.319	ND	ND	ND	ND	ND	ND	ND	ND

(Continued on following page)

TABLE 2 | (*Continued*) Major element geochemistry of the granites. Few samples have been analyzed for trace elements. LOI is negligible (<0.001%).

	TKB12	TKB13	TKB14	TKB16	TKB17	1G2	2G2	3G2	4G2	5G2	SP1	SP3	SP4	SP5	SP6
LOCATION		**Rupnagar metarhyolite**					**Pratapgarh granite**					**Sewariya granite**			
Ce	104.05	106.703	37.524	31.721	11.907	46.429	41.874	ND	ND	ND	ND	ND	ND	ND	ND
Pr	11.828	9.198	3.732	5.156	1.8	31.189	30.256	ND	ND	ND	ND	ND	ND	ND	ND
Nd	44.072	34.826	13.274	22.122	6.384	9.21	7.64	ND	ND	ND	ND	ND	ND	ND	ND
Sm	9.675	73.627	3.679	8.384	2.663	7.264	6.12	ND	ND	ND	ND	ND	ND	ND	ND
Eu	1.581	2.074	1.382	0.894	0.802	10.121	10.491	ND	ND	ND	ND	ND	ND	ND	ND
Gd	10.259	8.284	3.975	6.874	2.952	0.659	0.981	ND	ND	ND	ND	ND	ND	ND	ND
Tb	2.35	2.178	1.243	1.99	0.951	9.488	10.676	ND	ND	ND	ND	ND	ND	ND	ND
Dy	4.223	4.551	10.228	4.034	14.104	2.789	1.984	ND	ND	ND	ND	ND	ND	ND	ND
Ho	1.187	1.203	2.435	1.13	3.272	13.697	12.654	ND	ND	ND	ND	ND	ND	ND	ND
Er	2.73	2.869	7.342	2.806	9.087	3.322	3.189	ND	ND	ND	ND	ND	ND	ND	ND
Tm	0.772	0.737	1.311	0.832	1.726	10.855	11.298	ND	ND	ND	ND	ND	ND	ND	ND
Yb	2.403	2.33	6.772	3.897	9.609	1.747	1.894	ND	ND	ND	ND	ND	ND	ND	ND
Lu	0.608	0.57	1.211	0.89	1.591	10.332	11.255	ND	ND	ND	ND	ND	ND	ND	ND
Σ REE	241.956	283.312	106.55	100.25	69.63	170.6	162.631								
(La/Lu)N	7.832698	6.175502	1.058644	1.102175	0.180173	0.134614	0.11278								
Eu/Eu*	0.037274	0.010563	0.08498	0.027006	0.067356	0.530299	0.622572								

ratios and U content using an age of 559 Ma and U content of 909 ppm (Stern, 2001). TEMORA-2 and CZ3 were used as control standards and yielded 206Pb/238U ages within the error of those reported for them (Pidgeon et al., 1994; Black et al., 2003, 2004). Common Pb correction is based on measure nonradiogenic 204Pb isotope, and a common Pb composition applied following the Pb-evolution model of Stacey and Kramers (1975). Because analyses that recorded high counts on 204Pb during the first scan were aborted, corrections are small and insensitive to the choice of common Pb composition. Nevertheless, some analyses were characterized by very low contents of U, which, combined with the relatively young age, lead to low amounts of radiogenic Pb. In these cases, proportions of common Pb can become relatively high, even though counts on 204Pb were barely above background. Because of the low signal-to-noise ratio of the 204Pb signal, 204-correction suffers from imprecision particularly in these cases, and we, therefore, report uncorrected ratios in the table (**Table 3**) and in some cases used these uncorrected values to regress the data to common Pb and constrain an intercept age. Standard calibration errors are reported in **Table 3** but were not included in single spot ages and pooled age calculations. Single spot ages are reported at the 1σ confidence level, while pooled ages are reported at 95% confidence (**Figure 7**).

Th-U-Total Pb Monazite Geochronology

Monazite geochronology was carried out on monazite grains in the mica schist samples (sample location in **Figures 2B,C**; BSE and X-ray images in **Figures 8**, **9**, analytical data in **Table 4**). Monazite developed during metamorphism of the mica schist. Either a detrital monazite was recrystallized or elements like REE, Th, U, and P present in different minerals reacted in Ca poor condition producing monazite grains (Wawrzenitz et al., 2012). Crystallization of monazite occurred along with other minerals like quartz, feldspar, and biotite. The monazite grains have equant shape and are aligned parallel to S_1 fabric that results from dislocation creep, Sample No. B5 and R4 (cf. Passchier and Trouw, 2005). Subsequently, fluid action along the shear zone reprecipitates the monazite by dissolution precipitation creep (e.g., Wawrzenitz et al., 2012). Those monazites are elliptical in shape and aligned parallel to the mylonitic fabric, Sample No. CG1 and B4. Further, monazites undergo reprecipitation during brittle deformation due to fluid action and those monazites contain fractures. All these microfabrics of monazite in relation to host rock fabric were studied under BSE images and the events of crystallization/precipitation of monazite were identified.

Nine samples were analyzed, and 194 spot analyses were performed. Finally, we presented four representative samples (CG1, B4, B5, and R4) where the monazite shape could be unequivocally correlated with a particular deformation event. We used the Cameca SX-FIVE Electron Probe Micro-Analyzer (with five WDS spectrometers including LLIF and LPET crystals) for monazite geochronology, in the Department of Earth Sciences, IIT, Bombay. The single point/average method was used for finding the dates of the monazite grains (Montel et al., 1996). The age analyses were conducted at an

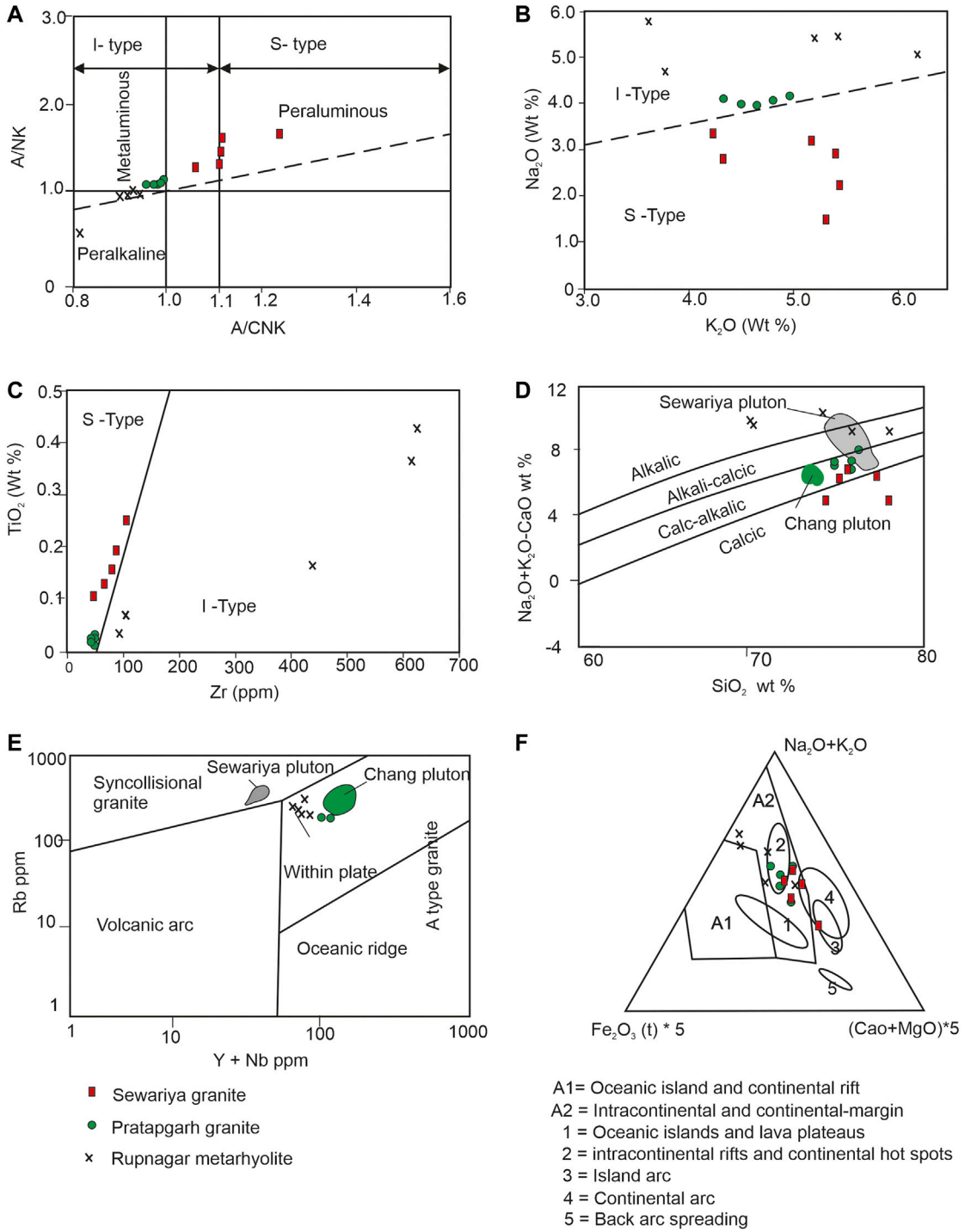

FIGURE 5 | (A) A/NK vs. A/CNK plot, **(B)** Na_2O vs. K_2O, **(C)** TiO_2 vs. Zr plot, peraluminous, meta-aluminous, peralkaline, I type, S type granite fields are after Chappell and White (1992), **(D)** $Na_2O + K_2O$-CaO vs. SiO_2 plot, alkalic-alkali-calcic, calc-alkalic, and calcic fields are after Frost et al. (2001), **(E)** Rb vs. Y + Nb plot within plate, syncollisional, volcanic arc, oceanic ridge granite fields are after Pearce (1996), **(F)** $Na_2O + K_2O$–(CaO + MgO)*5 Fe_2O_3 (t) * 5 ternary plot, fields of A1, A2, rift, island arc granites are after Grebennikov (2014).The fields of Chang and Sewariya plutons in **Fig. 5D** and **5E** are after Tiwana et al., 2019 and Ray et al. (2015), respectively.

accelerating voltage of 20 keV and a 200 nA prob current with 1μm beam diameter (Wawrzenitz et al., 2012). X-ray element mapping for Ce, La, Y, Pb, Th, and U in monazite was acquired with an accelerating voltage of 20 keV, beam current of 100 nA, and spatial resolution of 1–3 μm/pixel dwell times varying between 50 and 80 ms/pixel. Both natural and synthetic glass

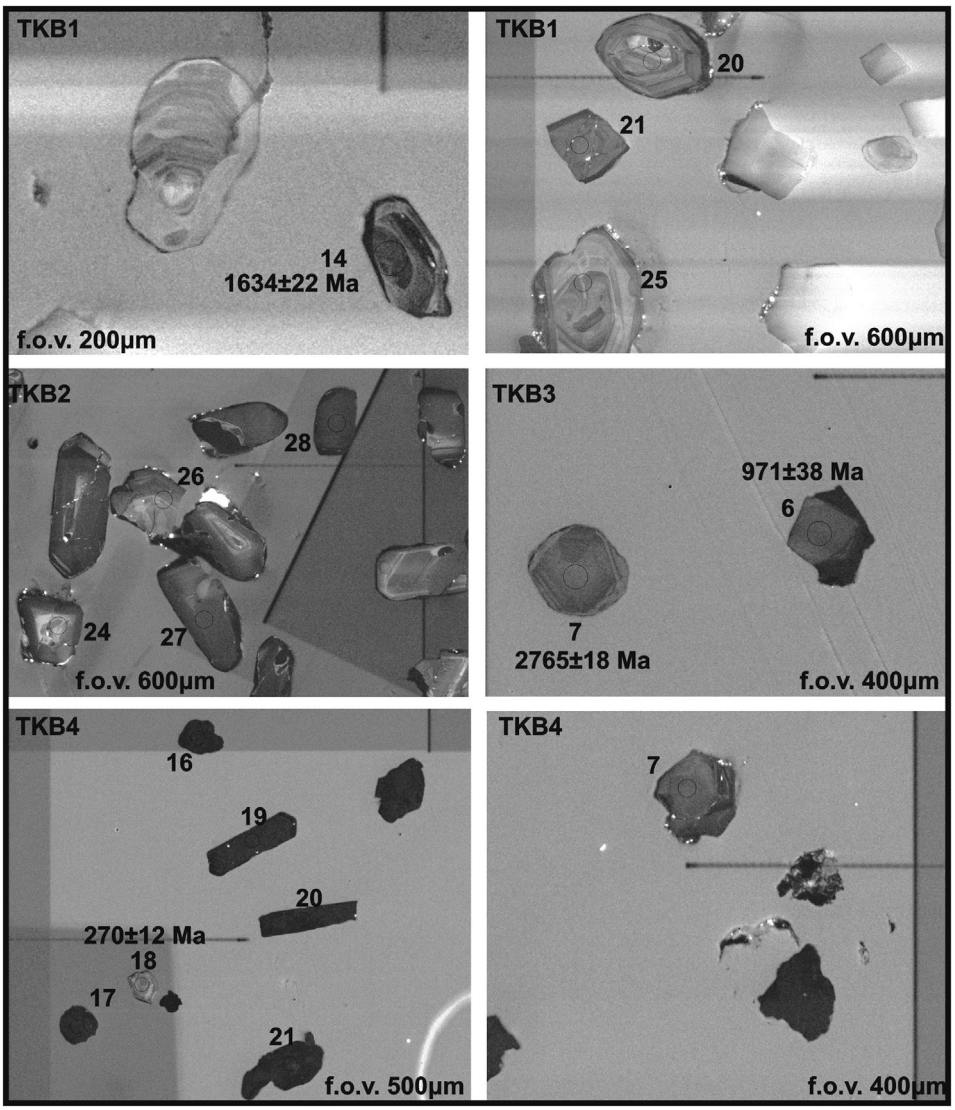

FIGURE 6 | CL images of zircon, sample numbers TKB-1, TKB-2, TKB-3, and TKB-4.

standards were used in calibrating major and trace elements in monazite. PbMa, ThMa, and UMb spectral lines were calibrated with crocoite (PbCrO4), Th glass (ThO2-5 wt.%), and U glass (UO2-5 wt.%) standards and simultaneously analyzed in two spectrometers for 240, 160, and 160 s, respectively, using subcounting methodology (cf. Spear and Wark, 2009; Prabhakar, 2013). The total counts of PbMa were acquired in the exponential mode to better define the distantly located background positions (Jercinovic and Williams, 2005; Jercinovic et al., 2008; Spear and Wark, 2009; Gonçalves et al., 2016). Background values for Th, U, Pb, and K are calculated from a nonlinear regression of high-precision wavelength dispersive scans (Jercinovic et al., 2008; Williams et al., 2006). Background values for the rest of the elements are based on linear interpolation of intensities between paired off-peak wavelength positions. The matrix effects (ZAF) were reduced with X-PHI method (Merlet, 1992). The significant peak interference of ThM2-O4, ThMζ1, ThMζ2, YLC2, YLC3, and LaLa on PbMa and ThMc and ThM3-N4 on UMb was corrected during quantification following the values given in **Supplementary Table S1** (Tiwari and Biswal, 2019a). More details on monazite dating protocol and interference corrections were outlined by Pant et al. (2009), Prabhakar (2013), Deshmukh et al. (2017), Chatterjee et al. (2017), Pandey et al. (2013), and Tiwari and Biswal, (2019a). By applying these conditions, detection limit was achieved as 100 ppm for Th, 110 ppm for U, and 80 ppm for Pb.

BSE images and X-ray mapping of all monazite grains in individual samples were documented. Individual domains were identified from such images, and two to three points in each domain were chemically analyzed (**Table 4**). PbO vs. ThO_2* diagram plotted (ThO_2* measured ThO_2 plus ThO_2 equivalent

TABLE 3 | Zircon U-Pb SHRIMP data (2σ error of the mean of 0.94%) samples TKB-1 (26,015′50′′/74,013′06″), TKB-2 (26,010′36′′/74,017′30″), TKB-3 (26,012′24′′/74,018′15″), and TKB-4 (26,013′36′′/74,019′48″).

Spot	% 206Pbc	ppm (U)	Ppm (Th)	232Th/ 238U	±%	206Pb/ 238U (Age)		207Pb/ 206Pb (Age)		208Pb/ 232Th (Age)		% Discordant	207Pb*/ 206Pb*	±%	207Pb*/ 235U	±%	206Pb*/ 238U	±%
TKB1																		
TKB1.30	0.06	296	86	0.30	0.88	895	±18	897	±23	892	±26	+0	0.0690	1.1	1.42	2.4	0.149	2.1
TKB1.29	0.09	190	56	0.30	1.11	881	±18	874	±30	920	±31	−1	0.0682	1.5	1.38	2.6	0.146	2.2
TKB1.20	0.45	170	101	0.61	0.34	887	±18	793	±49	841	±27	−13	0.0656	2.3	1.33	3.2	0.148	2.2
TKB1.24	0.06	151	55	0.38	0.42	882	±18	888	±32	889	±35	+1	0.0686	1.5	1.39	2.7	0.147	2.2
TKB1.25	2.02	250	94	0.39	7.65	832	±21	954	±180	664	±135	+14	0.0709	8.8	1.35	9.2	0.138	2.7
TKB1.26	1.49	287	470	1.69	2.85	744	±16	929	±69	501	±20	+21	0.0700	3.4	1.18	4.1	0.122	2.3
TKB1.27	0.15	292	137	0.49	0.82	885	±17	879	±27	868	±31	−1	0.0683	1.3	1.39	2.5	0.147	2.1
TKB1.19	0.13	132	72	0.56	0.39	873	±23	793	±40	846	±30	−11	0.0656	1.9	1.31	3.4	0.145	2.8
TKB1.21	0.37	300	70	0.24	1.13	857	±20	880	±36	872	±44	+3	0.0684	1.8	1.34	3.0	0.142	2.5
TKB1.22	0.00	127	101	0.82	4.14	885	±22	874	±33	913	±76	−1	0.0682	1.6	1.38	3.1	0.147	2.7
TKB1.23	0.09	184	61	0.34	0.39	879	±18	910	±30	886	±27	+4	0.0694	1.4	1.40	2.6	0.146	2.2
TKB1.14	0.09	434	209	0.50	1.39	1,619	±32	1,634	±11	1,497	±40	+1	0.1006	0.6	3.96	2.3	0.285	2.2
TKB1.15	0.33	213	117	0.57	6.25	849	±17	873	±38	308	±25	+3	0.0681	1.9	1.32	2.8	0.141	2.1
TKB1.16	0.15	118	60	0.53	0.47	874	±18	902	±42	883	±29	+3	0.0691	2.0	1.38	3.0	0.145	2.3
TKB1.17	0.28	187	88	0.49	1.06	884	±21	844	±54	872	±30	−5	0.0672	2.6	1.36	3.6	0.147	2.5
TKB1.18	0.10	162	83	0.53	0.36	884	±18	899	±32	887	±25	+2	0.0690	1.5	1.40	2.7	0.147	2.2
TKB1.9	0.08	193	78	0.42	0.33	879	±18	887	±28	864	±24	+1	0.0686	1.3	1.38	2.5	0.146	2.1
TKB2																		
TKB2.1	0.14	157	147	0.97	0.3	958	±19	1,015	±31	938	±24	6	0.073	1.5	1.61	2.7	0.16	2.2
TKB2.2	0.41	115	101	0.9	1.22	981	±20	891	±49	955	±29	−11	0.0687	2.4	1.56	3.3	0.164	2.2
TKB2.3	0.04	197	185	0.97	0.26	983	±21	975	±23	1,005	±25	−1	0.0716	1.1	1.63	2.6	0.165	2.3
TKB2.4	0.35	151	134	0.92	0.3	975	±20	1,008	±38	954	±25	3	0.0728	1.8	1.64	2.9	0.163	2.2
TKB2.5	0.13	207	346	1.73	2.31	956	±19	988	±26	587	±19	3	0.0721	1.3	1.59	2.5	0.16	2.1
TKB2.6	0.16	330	355	1.11	0.2	990	±19	957	±22	982	±22	−4	0.071	1.1	1.63	2.3	0.166	2.1
TKB2.7	0.03	206	212	1.06	0.25	985	±24	988	±22	993	±27	0	0.0721	1.1	1.64	2.8	0.165	2.6
TKB2.8	0.18	195	227	1.2	0.25	971	±19	979	±29	857	±20	1	0.0717	1.4	1.61	2.6	0.163	2.1
TKB2.9R	0.13	355	472	1.38	0.58	997	±19	951	±20	989	±22	−5	0.0708	1	1.63	2.3	0.167	2.1
TKB2.10R	0.01	483	681	1.46	0.45	981	±19	1,000	±14	972	±22	2	0.0725	0.7	1.64	2.2	0.164	2.1
TKB2.11C	0.26	283	367	1.34	3.35	948	±19	1,010	±27	846	±35	7	0.0729	1.3	1.59	2.5	0.158	2.1
TKB2.12	0.03	230	207	0.93	0.25	1,019	±20	957	±22	1,033	±24	−7	0.071	1.1	1.68	2.4	0.171	2.1
TKB2.14	–	443	512	1.19	0.28	986	±19	1,001	±14	973	±21	2	0.0725	0.7	1.65	2.2	0.165	2.1
TKB2.13C	0.06	198	194	1.01	0.7	970	±19	995	±23	965	±23	3	0.0723	1.1	1.62	2.4	0.162	2.1
TKB2.15	9.51	158	139	0.91	0.3	1,070	±27	838	±221	2095	±88	−30	0.067	10.6	1.67	11	0.18	2.8
TKB2.16	0.29	149	113	0.79	0.59	982	±20	941	±39	965	±27	−5	0.0704	1.9	1.6	2.9	0.165	2.2
TKB2.17	0.36	307	239	0.8	0.2	830	±18	924	±28	161	±8	11	0.0698	1.3	1.32	2.7	0.137	2.3
TKB2.18	0.12	220	226	1.06	0.24	982	±19	959	±25	973	±22	−3	0.071	1.2	1.61	2.4	0.165	2.1
TKB2.19	0.03	193	183	0.98	0.26	991	±20	1,003	±23	979	±23	1	0.0726	1.1	1.66	2.4	0.166	2.1
TKB2.20	0.81	373787	2E+06	5.23	0.5	1,357	±37	846	±89	1,099	±35	−67	0.0673	4.3	2.17	5.2	0.234	3
TKB2.21	--	292	301	1.06	0.49	986	±19	1,013	±18	971	±22	3	0.073	0.9	1.66	2.3	0.165	2.1
TKB2.22	0.05	137	107	0.81	0.72	944	±19	1,047	±27	950	±25	11	0.0742	1.4	1.61	2.6	0.158	2.2
TKB2.23	0.06	230	223	1	0.27	967	±19	973	±23	950	±22	1	0.0715	1.1	1.6	2.4	0.162	2.1
TKB2.24	0.06	386	427	1.14	0.18	978	±19	1,008	±16	964	±21	3	0.0728	0.8	1.64	2.2	0.164	2.1

(Continued on following page)

TABLE 3 | (*Continued*) Zircon U-Pb SHRIMP data (2σ error of the mean of 0.94%) samples TKB-1 (26,015′50′′/74,013′06″), TKB-2 (26,010′36′′/74,017′30″), TKB-3 (26,012′24′′/74,018′15″), and TKB-4 (26,013′36′′/74,019′48″).

Spot	% 206Pbc	ppm (U)	Ppm (Th)	232Th/238U	±%	206Pb/238U (Age)		207Pb/206Pb (Age)		208Pb/232Th (Age)		% Discordant	207Pb*/206Pb*	±%	207Pb*/235U	±%	206Pb*/238U	±%
TKB2.25	--	249	241	1	0.76	985	±19	978	±18	977	±23	−1	0.0717	0.9	1.63	2.3	0.165	2.1
TKB2.26	0.1	256	262	1.06	0.22	984	±19	958	±22	964	±22	−3	0.071	1.1	1.61	2.4	0.165	2.1
TKB2.27	0.12	439	546	1.28	0.41	997	±19	967	±17	959	±21	−3	0.0713	0.8	1.65	2.2	0.167	2.1
TKB2.28	0.05	421	469	1.15	0.17	976	±19	1,027	±15	967	±21	5	0.0735	0.8	1.66	2.2	0.163	2.1
TKB2.29	0.26	181	170	0.97	0.27	970	±19	948	±33	944	±23	−2	0.0707	1.6	1.58	2.7	0.162	2.2
TKB2.30	0.13	256	252	1.02	0.22	987	±19	968	±23	973	±22	−2	0.0714	1.1	1.63	2.4	0.165	2.1
TKB3																		
TKB3.1	0.54	1,248	29	0.02	3.42	860	±16	910	±26	3,806	±484	6	0.0694	1.2	1.37	2.4	0.143	2
TKB3.2	0.06	1,200	247	0.21	14	895	±35	935	±10	921	±186	5	0.0702	0.5	1.44	4.2	0.149	4.2
TKB3.5	6.15	524	978	1.93	0.97	565	±18	906	±102	648	±24	39	0.0692	5	0.87	6	0.092	3.3
TKB3.6	0.03	248	386	1.61	0.21	971	±19	1,005	±20	932	±21	4	0.0727	1	1.63	2.3	0.163	2.1
TKB3.7	0.06	120	86	0.74	0.36	2,697	±49	2,765	±9	2,665	±61	3	0.1927	0.5	13.8	2.3	0.519	2.2
TKB3.8	9.99	500	128	0.27	0.89	177	±4	1,431	±171	1,573	±60	89	0.0903	9	0.35	9.3	0.028	2.3
TKB3.23	3.77	1,383	1,011	0.76	1.05	990	±19	935	±51	1,574	±55	−6	0.0702	2.5	1.61	3.2	0.166	2
TKB3.9	7.73	1802	248	0.14	2.29	404	±11	980	±67	2,724	±105	61	0.0718	3.3	0.64	4.3	0.065	2.7
TKB3.10	--	473	561	1.23	0.6	976	±19	1,033	±14	963	±21	6	0.0737	0.7	1.66	2.2	0.163	2.1
TKB3.11	0.03	198	282	1.47	0.24	968	±19	1,024	±22	945	±21	6	0.0733	1.1	1.64	2.4	0.162	2.1
TKB3.12	0.29	100	134	1.38	17	963	±22	963	±50	929	±225	0	0.0712	2.5	1.58	3.5	0.161	2.5
TKB3.13	0.05	692	53	0.08	2.66	1,009	±36	999	±104	942	±50	−1	0.0724	5.1	1.69	6.4	0.169	3.9
TKB3.14	0.02	320	334	1.08	0.32	996	±19	988	±18	973	±21	−1	0.0721	0.9	1.66	2.3	0.167	2.1
TKB3.16	21.71	11,915	21,102	1.83	6.54	532	±39	1,686	±874	306	±89	71	0.1034	47.3	1.23	47.9	0.086	7.6
TKB3.24	0.39	169	134	0.82	0.53	431	±9	413	±79	432	±14	−5	0.055	3.5	0.53	4.1	0.069	2.2
TKB3.25	0.06	495	131	0.27	0.39	1,389	±26	1,407	±10	1,353	±31	1	0.0892	0.5	2.96	2.1	0.24	2.1
TKB3.20	–	305	275	0.93	0.7	274	±6	248	±44	271	±8	−11	0.0512	1.9	0.31	3	0.043	2.3
TKB3.21	1.12	852	646	0.78	2.33	1,033	±20	914	±42	871	±33	−14	0.0695	2	1.67	3	0.174	2.1
TKB3.18	–	112	57	0.53	0.42	2,358	±45	2,591	±11	2,478	±61	11	0.1734	0.6	10.56	2.3	0.442	2.3
TKB3.4	2.95	565	1,071	1.96	1.33	756	±21	1,035	±84	807	±28	29	0.0738	4.1	1.27	5.1	0.124	2.9
TKB4																		
TKB4.1	0.14	167	121	0.75	0.67	951	±19	974	±32	970	±26	3	0.0716	1.5	1.57	2.7	0.159	2.2
TKB4.2	2.65	2,576	14	0.01	0.66	800	±19	804	±162	39.2	±4,054	1	0.0659	7.7	1.2	8.2	0.132	2.6
TKB4.3	0.27	30	63	2.14	0.61	2,841	±67	2,981	±17	2,646	±93	6	0.22	1.1	16.8	3.1	0.554	2.9
TKB4.4	0.07	776	648	0.86	3.66	919	±17	954	±14	970	±65	4	0.0709	0.7	1.5	2.1	0.153	2
TKB4.6	0.45	1,468	1,232	0.87	11	773	±35	994	±33	591	±87	24	0.0723	1.6	1.27	5.1	0.127	4.9
TKB4.5	23.43	1885	23	0.01	2.06	1,050	±36	954	±152	7,097	±2,442	−11	0.0709	7.4	1.73	8.3	0.177	3.7
TKB4.7	0.12	386	119	0.32	0.27	625	±12	636	±29	593	±18	2	0.0609	1.4	0.85	2.5	0.102	2.1
TKB4.17	30.89	1,698	11	0.01	2.8	1,050	±30	896	±224	11,891	±5,058	−19	0.0689	10.9	1.68	11.3	0.177	3
TKB4.16	36.8	4,253	137	0.03	1.86	835	±20	1,022	±95	2,717	±587	19	0.0733	4.7	1.4	5.4	0.138	2.6
TKB4.15	35.62	4,421	71	0.02	1.7	703	±21	1,096	±85	4,614	±885	38	0.076	4.2	1.21	5.3	0.115	3.2
TKB4.14	11.61	3,760	25	0.01	1.39	1,032	±35	895	±112	5,940	±2,862	−17	0.0689	5.4	1.65	6.5	0.174	3.7
TKB4.13	37.03	4,903	253	0.05	1.68	751	±23	1,072	±77	1780	±321	32	0.0751	3.8	1.28	5	0.124	3.2
TKB4.12	3.43	2,728	15	0.01	1.8	755	±31	749	±298	-2,756	-9,261	−1	0.0642	14.1	1.1	14.8	0.124	4.3
TKB4.18	0.48	371	280	0.78	0.22	270	±6	210	±85	260	±9	−30	0.0503	3.7	0.3	4.3	0.043	2.3
TKB4.19	33.63	4,041	88	0.02	7.12	1,245	±33	983	±288	8,141	±2,535	−29	0.0719	14.1	2.11	14.4	0.213	2.9
TKB4.20	2.67	2,936	19	0.01	2.03	774	±15	789	±52	673	±1,364	2	0.0655	2.5	1.15	3.2	0.128	2

(Continued on following page)

TABLE 3 | *(Continued)* Zircon U-Pb SHRIMP data (2σ error of the mean of 0.94%) samples TKB-1 (26,015′50″/74,013′06″), TKB-2 (26,010′36″/74,017′30″), TKB-3 (26,012′24″/74,018′15″), and TKB-4 (26,013′36″/74,019′48″).

Spot	% 206Pbc	ppm (U)	Ppm (Th)	232Th/238U	± %	206Pb/238U (Age)		207Pb/206Pb (Age)		208Pb/232Th (Age)		% Discordant	207Pb*/206Pb*	± %	207Pb*/235U	± %	206Pb*/238U	± %
TKB4.21	36.39	3,691	17	0	3.67	1,050	±39	1,014	±125	21,350	±1924	−4	0.073	6.1	1.78	7.3	0.177	4
TKB4.22	29.78	3,045	181	0.06	11	858	±20	976	±94	1,371	±382	13	0.0716	4.6	1.41	5.2	0.142	2.5
TKB4.23	4.91	3,647	23	0.01	2.11	1,284	±31	916	±117	4,094	±3,981	−44	0.0696	5.7	2.11	6.3	0.22	2.6
TKB4.24	26.09	2,334	18	0.01	0.62	888	±37	1,101	±211	10,152	±1913	21	0.0762	10.5	1.55	11.4	0.148	4.4
TKB4.25	27.17	2,506	24	0.01	7.05	1,003	±26	718	±215	2,880	±4,257	−43	0.0633	10.1	1.47	10.5	0.168	2.7
TKB4.26	3.45	2,210	10	0	0.85	674	±14	862	±124	3,283	±3,244	23	0.0678	6	1.03	6.4	0.11	2.2
TKB4.27	11.75	3,309	39	0.01	13	688	±17	872	±129	2,110	±1,095	22	0.0681	6.2	1.06	6.8	0.113	2.6
TKB4.28	–	324	118	0.38	1.67	1,077	±23	1,190	±17	1,173	±59	10	0.0797	0.9	2	2.5	0.182	2.4
TKB4.8	15.46	2,441	17	0.01	0.58	780	±17	893	±73	3,657	±1,643	13	0.0688	3.5	1.22	4.2	0.129	2.3
TKB4.10	3.38	1,281	4	0	5.35	822	±16	916	±173	5,697	±7,863	11	0.0696	8.4	1.31	8.7	0.136	2.1

of measured UO_2). Data points are arrayed linearly to provide an isochron; the slope of the line (m) is used to calculate the age of the event (Suzuki and Dunkley, 2014).

Further, from the analytical data the spot age is computed using the formulation of Montel et al. (1996). From the individual age and associated error data, the inverse-variance weighted mean and 2σ error were calculated using Gaussian distribution and Isoplot logarithm tool (Sambridge and Compston, 1994; Ludwig, 2012). The entire population of unmixed ages of monazite of an individual sample was used to construct a probability density diagram by Isoplot. Dates constrained by weighted means of monazite dates in Isoplot are interpreted to constrain the age of monazite growth in single or multiple events depending upon number of peaks.

RESULT OF GEOCHEMISTRY AND GEOCHRONOLOGY

Geochemistry

Metarhyolite

A higher % of SiO_2 (70.52–78.12%), moderate to high Fe_2O_3 (0.4–0.98), moderate to high Al_2O_3 (10.68–15.83), and higher Na_2O compared to K_2O characterize the metarhyolite (**Table 2**). The A/NK and A/CNK values are <1.0 and CIPW norm shows presence of normative quartz, diopside, albite, and ilmenite. The samples lie in the peralkaline field in the A/NK vs. A/CNK plot (**Figure 5A**), I type field in the Na_2O vs. K_2O and TiO_2 vs Zr plots (**Figures 5B,C**) (cf. Chappell and White, 1992), and alkali-calcic to alkalic field in Na_2O + K_2O-CaO vs. SiO_2 plot (**Figure 5D**) (cf. Frost et al., 2001). $(La/Lu)_N$ is extremely variable ranging from 0.11 to 7.83 suggesting low to moderate REE differentiation and Eu/Eu* value ranges from 0.01 to 0.62 suggesting -ve Eu anomaly (**Table 2**). Rb vs. Y + Nb plot indicates "within plate magmatism" (**Figure 5E**) (Pearce, 1996) and Na_2O + K_2O–(CaO + MgO)*5 Fe_2O_3 (t) * 5 ternary plot (**Figure 5F**) shows the samples lie in "intracontinental-continental margin and intracontinental rift and continental hot spots setting" (Grebennikov, 2014). The Zr values range in 48.75–670.18 ppm indicating Zr saturation temperature is around 750 to 800°C (cf. Watson and Harrison, 1983).

Pratapgarh Pluton

Higher % of SiO_2 (75.51–76.52), moderate to high Fe_2O_3 (0.51–0.92), moderate to high Al_2O_3 (12.26–12.87), and lower Na_2O compared to K_2O characterize the Pratapgarh granite. It shows A/NK > 1.0 and the A/CNK values <1.0 (**Table 2**). The CIPW norm shows these are quartz, diopside, albite, and ilmenite normative. The samples lie in the meta-aluminous field of the A/NK vs. A/CNK plot (**Figures 5A,** I type field of the Na_2O vs. K_2O and TiO_2 vs. Zr plot (**Figures 5B,C**) (Chappell and White, 1992) and calc-alkaline field in Na_2O + K_2O-CaO vs. SiO_2 plot (**Figures 5D**) (cf. Frost et al., 2001). The $(La/Lu)_N$ is 0.11–0.13 suggesting low degree of REE differentiation and Eu/Eu* value is 0.53 and 0.62 suggesting -ve Eu anomaly (**Table 2**). Rb vs. Y + Nb plot indicates "within plate magmatism" (**Figure 5E**) (Pearce,

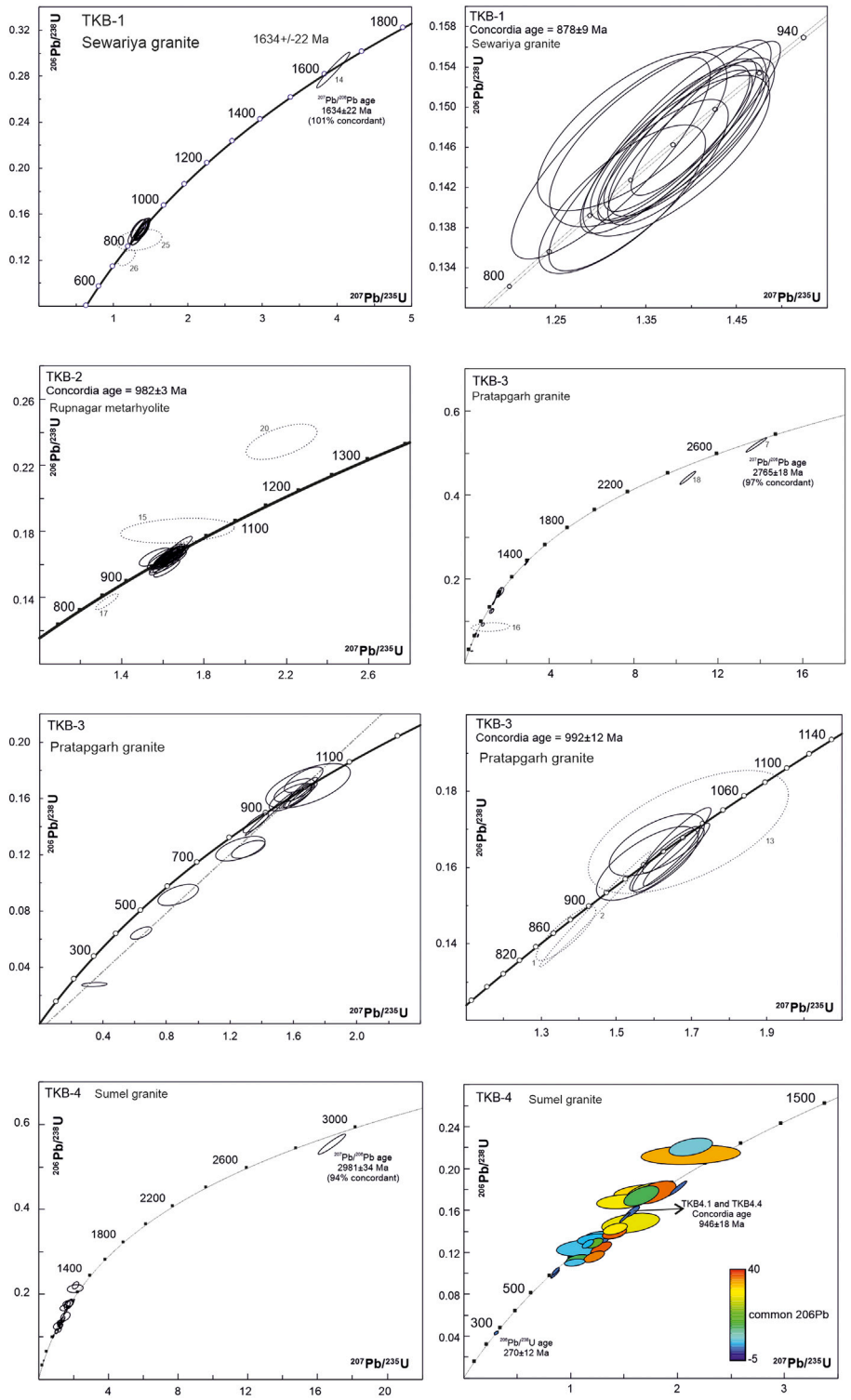

FIGURE 7 | Zircon U-Pb data for samples TKB-1, TKB-2, TKB-3, and TKB-4 locations are in **Figure 2**. Errors are at 1σ confidence level.

1996) and Na_2O + K_2O–(CaO + MgO)*5 Fe_2O_3 (t) * 5 ternary plot (**Figure 5F**) shows the sample lies in "intracontinental-continental margin and intracontinental rift and continental hot spots setting" (Grebennikov, 2014). Zr values range in 47–670 ppm indicating Zr saturation temperature is around 750 to 800 °C (cf. Watson and Harrison, 1983).

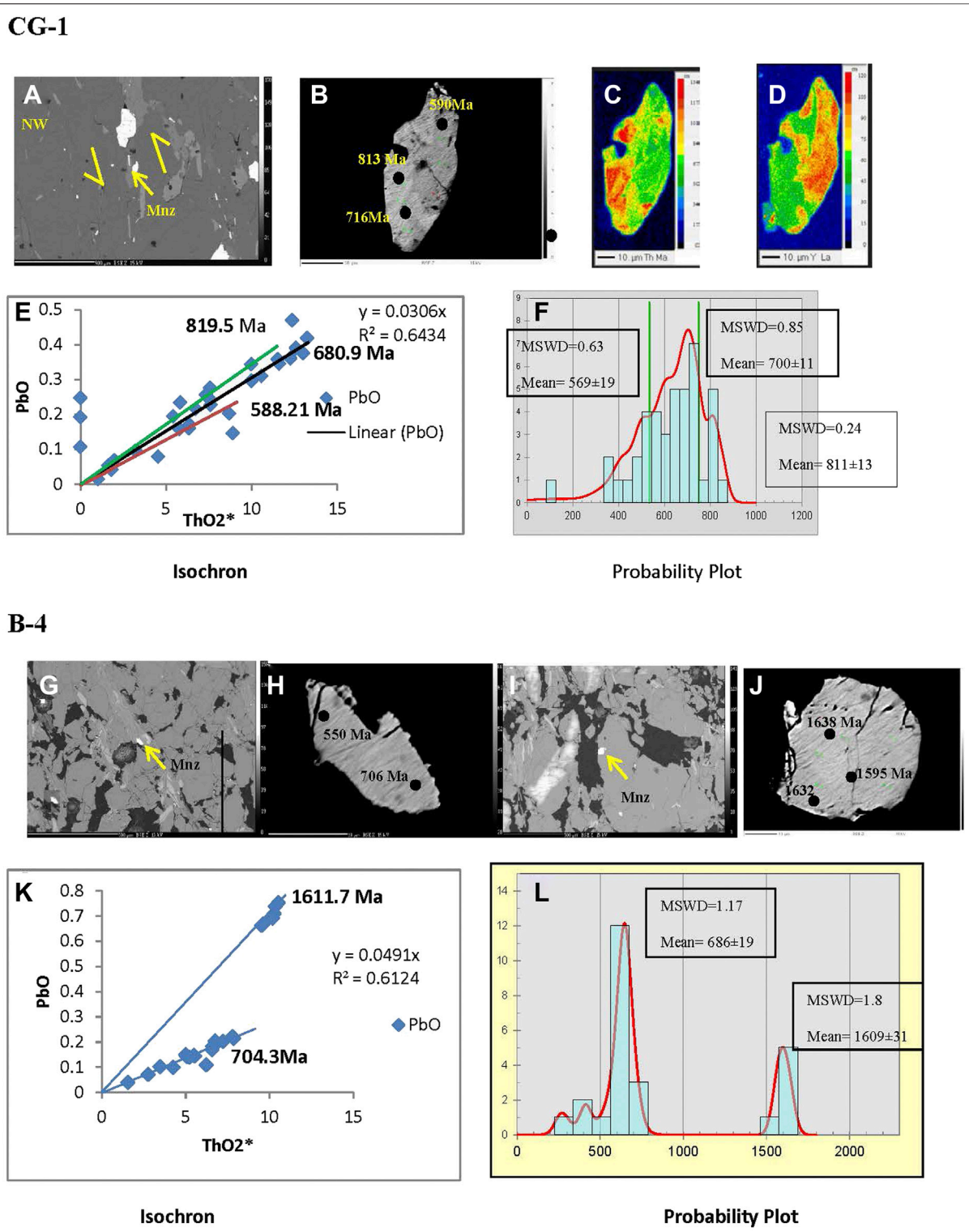

FIGURE 8 | Sample No. CG-1, **(A)** BSE image of mica schist mylonite with elliptical monazite grains, from Phulad thrust, from the inclination of the monazite grain, a top-to-NW sense of shear is indicated, **(B)** 813 and 716 ages are obtained from the high Th and low Y domain, 590 Ma age from fractured part of the grain, which is low in Th and high in Y (X-ray maps in **(C and D)**). **(E)** Isochron shows three ages 819, 680, and 588 Ma. **(F)** Probability curve shows three peaks as 811, 700, and 569 Ma. First two ages from 'e and f' correspond to D_2 and last age corresponds to brittle deformation. Sample No. B-4 **(G and I)** BSE images of the upper amphibolite slivers containing elliptical and rounded monazite grains, within Phulad thrust. **(H)** Elliptical grain is fractured in the top end. The grain yields 706 Ma and 550 Ma indicating age of D_2 and brittle deformation. **(J)** Rounded grain does not show chemical variation and yields higher ages ca. 1,638 Ma that indicates pre-Delhi metamorphism. **(K)** Isochron and (L) probability graph display two age clusters, 1,611–704 Ma and 1,609–686 Ma, related to pre-Delhi metamorphism and D_2 ages.

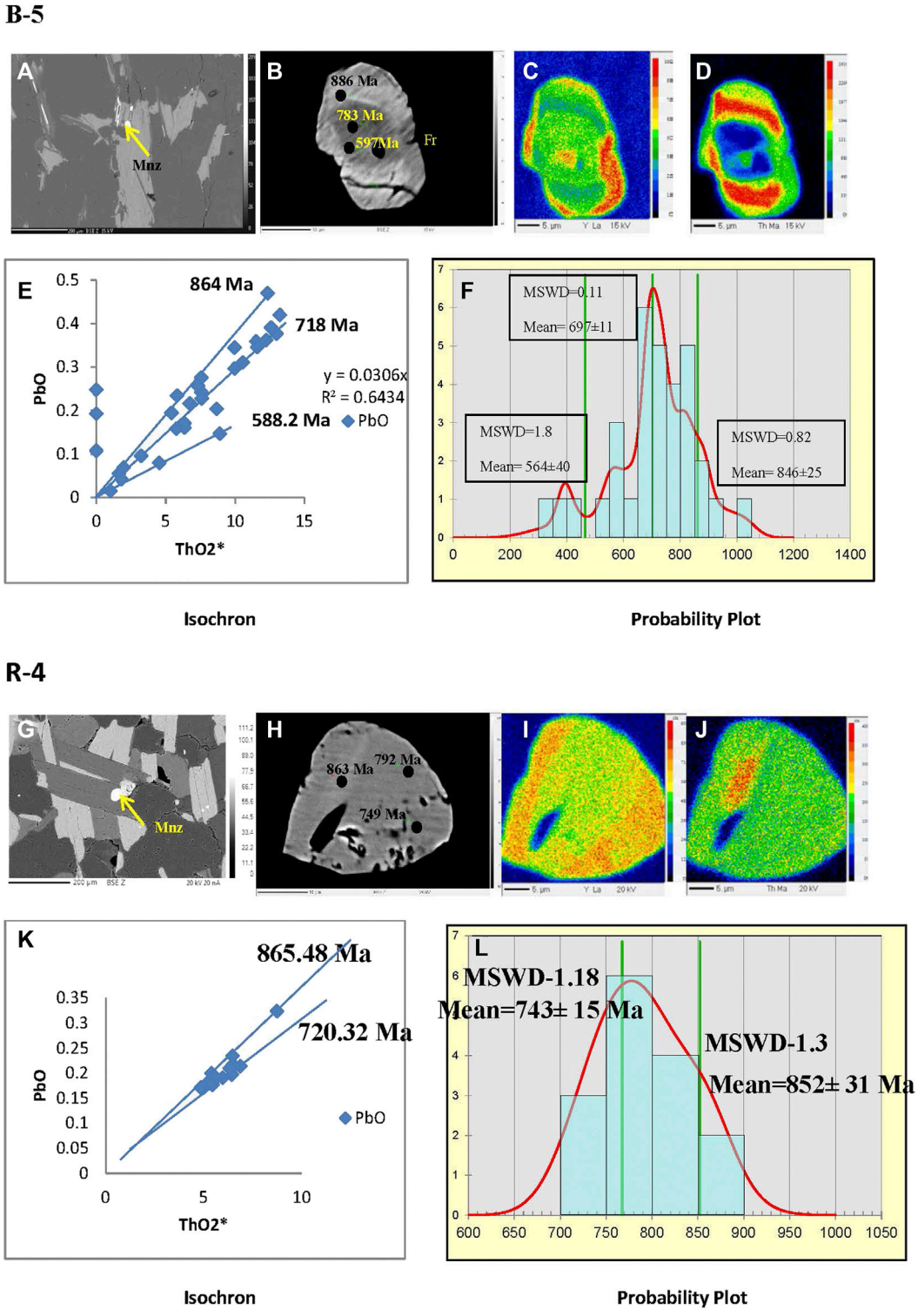

FIGURE 9 | Sample B-5, collected from mica schist: **(A)** Monazite under BSE image shows more or less equant shape and compositional domains. **(B)** The lighter domain that occurs outside is Y poor and Th rich (X-ray images, **(C)**, **(D))** yielding higher ages as 886 Ma, indicating the age of the D_1. The darker domains, at the center, are Y rich and Th poor and yield 783 and 597 Ma ages, indicating D_2 and brittle deformation ages, respectively; there is minor fracture at the edge (Fr); fluid migrated through the fracture and rejuvenated the age. **(E and F)** Isochron and probability curve yield three clusters as 864, 718, 588 Ma, 846, 697, 564 Ma corresponding to D_1, D_2 shearing and brittle shearing ages, respectively. Sample R-4. Mica schist near Pratapgarh, Monazites are nearly rounded to equant shape and have domains **(G** to **J)**. **(K and L)** Isochron and probability curve yield two distinct ages 865–720 Ma and 852–743 Ma corresponding to D_1–D_2 ages, respectively.

TABLE 4 | EPMA analytical result of monazite for the samples CG-1 (26,014′12′′/,74,013′25″), B-4 (26,013′44′′/,74,013′12″), B-5 (26,013′27′′/,74,013′12″), and R-4 (26,012′56′′/,74,018′30″).

CG1 Point	Al_2O_3	SiO_2	P_2O_5	CaO	FeO	Y_2O_3	La_2O_3	Ce_2O_3	Pr_2O_3	Nd_2O_3	Sm_2O_3	Eu_2O_3	Gd_2O_3	Tb_2O_3	Dy_2O_3	Tm_2O_3	PbO	ThO_2	UO_2	Total	Age (Ma)	Age err
1/1	0	0.264	30.409	0.999	0	1.344	15.06	29.664	3.263	11.397	2.222	0.248	1.05	0.053	0.316	0.083	0.143	3.798	0.252	100.566	720	46
2/1	0.001	0.224	30.521	0.653	0	1.365	16.024	29.913	3.349	11.454	2.244	0.251	1.033	0.039	0.304	0.157	0.094	3.084	0.067	100.776	663	52
3/1	0.022	0.331	30.39	0.66	0	1.095	16.13	30.282	3.269	11.701	2.147	0.234	1.077	0.006	0.306	0.124	0.092	3.407	0.074	101.345	590	47
4/1	0.018	0.795	29.168	0.532	0	0.455	16.525	30.304	3.283	11.635	1.816	0	0.654	0	0.075	0.063	0.16	5.053	0.126	100.662	686	40
5/1	0.014	1.064	29.061	0.724	0	0.487	16.045	29.178	3.131	11.04	1.735	0.009	0.708	0	0.07	0.04	0.237	6.229	0.17	99.945	813	36
6/1	0.025	0.77	30.016	0.513	0	0.375	16.854	30.729	3.228	11.649	1.776	0.093	0.663	0	0.093	0.015	0.149	4.519	0.106	101.573	716	44
7/1	0.066	0.791	30.954	1.214	0	1.416	14.189	27.668	3.106	10.891	2.178	0.305	1.173	0.046	0.406	0.119	0.208	5.876	0.399	101.005	677	32
8/1	0.006	0.338	31.537	0.68	0	1.438	15.419	30.033	3.174	11.321	2.335	0.349	1.191	0.048	0.379	0.12	0.117	2.821	0.426	101.732	649	47
9/1	0.82	2.464	26.47	0.952	0.008	1.516	14.435	28.285	3.051	11.01	2.281	0.329	1.139	0.018	0.328	0.15	0.143	3.571	0.55	97.519	621	39
10/1	0.674	0.479	30.105	1.137	0	1.476	14.302	27.81	3.105	10.625	2.2	0.335	1.368	0.081	0.485	0.088	0.224	4.886	0.762	100.141	705	33
11/1	0.034	0.534	28.723	1.355	0	1.535	13.691	26.481	3.037	10.538	2.183	0.262	1.277	0.034	0.413	0.116	0.27	7.286	0.561	98.33	692	27
12/1	0.106	0.424	30.062	0.939	0	1.285	14.808	28.548	3.156	11.17	2.279	0.316	1.235	0.003	0.337	0.095	0.166	4.629	0.42	99.976	647	36
13/1	0.06	0.37	28.809	0.665	0	1.299	15.42	29.344	3.169	11.132	2.247	0.296	1.188	0.045	0.334	0.095	0.118	2.869	0.463	97.922	627	45
14/1	1.108	0.378	29.892	0.704	0	1.223	15.574	29.883	3.167	11.378	2.321	0.356	1.222	0.036	0.383	0.148	0.097	2.614	0.406	100.89	577	46
15/1	0.051	0.29	28.749	0.574	0	1.356	15.744	29.792	3.283	11.247	2.326	0.277	1.162	0.009	0.359	0.104	0.079	2.073	0.468	97.943	515	46
16/1	0.003	1.084	28.37	1.957	0	1.241	12.346	22.619	2.771	10.275	2.239	0.294	1.724	0.055	0.427	0.133	0.436	12.449	0.009	98.431	815	22
17/1	0	0.75	28.833	1.63	0	1.485	12.754	24.716	2.946	10.379	2.243	0.28	1.56	0.03	0.419	0.153	0.327	8.404	0.281	97.189	817	28
18/1	0.072	1.224	28.442	2.213	0	1.552	11.918	23.254	2.665	9.607	2.081	0.276	1.569	0.069	0.521	0	0.495	12.361	0.325	98.643	858	22
20/1	0.041	0.599	29.386	1.52	0	1.692	13.338	26.485	2.991	10.569	2.259	0.34	1.416	0.05	0.507	0.117	0.277	6.664	0.697	98.947	722	28
21/1	0.081	1.08	27.888	1.969	1.984	1.42	12.352	24.176	2.684	9.602	2.084	0.29	1.361	0.062	0.443	0.118	0.397	11.001	0.402	99.394	752	23
22/1	0.148	0.405	28.069	1.452	0.776	1.456	13.742	26.783	2.984	10.569	2.194	0.272	1.191	0.087	0.347	0	0.246	6.159	0.618	97.499	702	30
23/1	0.388	0.783	27.717	1.604	0.804	1.542	12.977	25.589	2.933	10.443	2.163	0.342	1.248	0.044	0.339	0	0.199	6.089	0.513	95.716	601	27
24/1	0	0.35	29.954	1.461	0.023	1.499	14.264	27.389	2.912	10.659	2.226	0.308	1.308	0.095	0.409	0	0.265	6.533	0.635	100.293	718	29
25/1	0.003	0.24	30.135	0.588	0	1.463	15.837	30.094	3.271	11.29	2.215	0.289	1.132	0.003	0.37	0.084	0.096	2.643	0.566	100.319	502	39
26/1	0.011	0.218	30.144	0.576	0	1.718	15.879	29.496	3.232	11.045	2.252	0.234	1.079	0.004	0.437	0.03	0.163	1.792	1.815	100.125	496	27
27/1	0.038	0.421	29.646	1.298	0.457	1.397	14.817	29.692	3.033	11.04	2.275	0.315	1.149	0	0.33	0.078	0.137	2.389	0.487	99	796	53
28/1	0.199	0.706	31.316	0.715	0	0.633	16.422	29.64	3.2	11.492	1.888	0	0.833	0	0.117	0.061	0.148	4.201	0.204	101.774	710	43
29/1	0.084	0.659	26.397	0.624	0	0.681	15.756	29.459	3.242	11.61	1.955	0.046	0.836	0.021	0.19	0.056	0.14	4.746	0.128	96.63	635	39
30/1	0.028	0.178	29.877	0.721	0	1.516	15.748	29.968	3.296	11.259	2.199	0.281	1.097	0	0.305	0.125	0.05	2.158	0.098	98.905	475	52
31/1	0.039	0.156	27.823	0.576	0	1.645	15.415	29.976	3.368	11.78	2.294	0.309	1.052	0.045	0.339	0.162	0.036	1.64	0.113	96.769	419	53
32/1	0.1	0.304	27.642	0.761	0	1.561	15.046	28.516	3.195	11.316	2.226	0.294	1.153	0.026	0.328	0.121	0.091	3.342	0.138	96.16	564	43
33/1	0.04	0.76	28.625	1.596	0	1.574	13.245	25.929	2.942	10.572	2.204	0.235	1.296	0.077	0.372	0.118	0.311	8.404	0.411	98.711	743	26
34/1	0.024	0.676	28.489	1.522	0	1.574	13.33	26.176	2.939	10.668	2.167	0.301	1.316	0.058	0.387	0.197	0.298	7.445	0.365	97.933	803	29
35/1	7.47	79.071	0.451	0.133	5.17	0	0.316	2.367	0.106	0.183	0.073	0.005	0	0	0.27	0.036	0.031	5.56	0.734	101.975	93	21
38/1	0.123	1.918	36.814	7.744	0	1.321	15.024	29.11	2.377	11.6	2.349	0.341	1.328	0.059	0.487	0.174	0.093	2.635	0.817	114.313	414	33
39/1	0.006	0.19	29.417	0.445	0	0.436	12.82	30.205	3.733	14.41	2.875	0.586	0.876	0	0	0.192	0.022	1.403	0	97.614	370	67
40/1	0.265	0.183	29.193	0.567	0	0.536	11.592	30.067	3.757	14.999	3.095	0.705	1.02	0	0.025	0.183	0.016	1.076	0	97.28	349	74
41/1	0	0.29	29.44	0.457	0	0.444	16.927	30.605	3.348	11.656	1.988	0.07	0.808	0	0.059	0.149	0.032	1.489	0	97.764	504	70
42/1	0.009	0.255	30.266	0.754	0	1.602	15.456	29.837	3.185	11.444	2.373	0.336	1.425	0	0.423	0.114	0.099	3.15	0.265	100.993	576	44
43/1	0.035	0.201	30.594	0.801	0	1.518	15.805	29.937	3.208	11.199	2.378	0.381	1.335	0.059	0.445	0.204	0.072	2.291	0.207	100.67	565	53
44/1	0.071	1.312	30.372	0.697	0	1.399	16.345	30.252	3.254	11.401	2.373	0.309	1.117	0.071	0.324	0.12	0.051	1.677	0.179	101.324	526	60
45/1	0.189	0.313	31.427	0.746	0	1.05	16.055	30.507	3.178	10.743	2.24	0.312	1.121	0.022	0.255	0.138	0.099	2.749	0.146	101.29	719	58
B4																						
1/1	0	0.302	30.646	1.808	0	1.191	13.522	26.641	3.09	10.229	2.101	0.059	1.089	0	0.309	0.109	0.71	7.227	0.838	99.871	1,585	37
2/1	0	0.325	30.743	1.797	0	1.172	13.755	26.86	3.089	10.176	2.04	0.087	1.123	0	0.286	0.147	0.738	7.056	0.902	100.297	1,632	37
3/1	0.001	0.37	30.623	1.823	0	1.139	13.86	26.838	3.041	10.113	1.971	0.113	1.014	0	0.21	0.124	0.753	7.118	0.933	100.044	1,638	36
4/1	0	0.281	30.514	1.537	0	1.496	15.219	27.433	2.905	9.677	1.813	0.009	0.887	0	0.299	0.069	0.663	5.92	0.994	99.715	1,595	38

(Continued on following page)

TABLE 4 | (*Continued*) EPMA analytical result of monazite for the samples CG-1 (26,014′12′′/,74,013′25″), B-4 (26,013′44′′/,74,013′12″), B-5 (26,013′27′′/,74,013′12″), and R-4 (26,012′56′′/,74,018′30″).

CG1 Point	Al_2O_3	SiO_2	P_2O_5	CaO	FeO	Y_2O_3	La_2O_3	Ce_2O_3	Pr_2O_3	Nd_2O_3	Sm_2O_3	Eu_2O_3	Gd_2O_3	Tb_2O_3	Dy_2O_3	Tm_2O_3	PbO	ThO_2	UO_2	Total	Age (Ma)	Age err
5/1	0.006	0.307	30.645	1.54	0	1.446	15.183	27.451	2.97	9.704	1.807	0	0.927	0.033	0.371	0.11	0.668	6.066	0.982	100.217	1,590	38
6/1	0	0.274	30.53	1.492	0	1.428	15.85	27.684	2.982	9.189	1.601	0	0.843	0.058	0.355	0.151	0.692	5.772	1.218	100.122	1,560	36
7/1	0.014	0.25	29.996	0.63	0	1.242	14.741	29.557	3.186	11.252	2.359	0.298	1.456	0.067	0.466	0.115	0.099	3.055	0.362	99.145	550	44
8/1	0.016	0.308	29.902	0.928	0	1.25	14.604	28.792	3.136	10.99	2.245	0.302	1.481	0.11	0.476	0.141	0.188	5.289	0.431	100.588	656	34
9/1	0.016	0.195	30.181	1.128	0	1.366	14.711	28.234	3.049	10.201	2.15	0.278	1.435	0.055	0.419	0.147	0.204	4.089	0.8	98.656	706	35
10/1	0.01	0.297	29.769	0.877	0	1.291	14.639	28.825	3.117	10.773	2.299	0.236	1.388	0.062	0.439	0.142	0.145	4.155	0.416	98.88	615	38
11/1	0	0.152	30.164	1.081	0	1.609	13.985	27.78	3.012	10.735	2.182	0.436	1.27	0.05	0.435	0.139	0.214	3.855	1.199	98.299	640	30
12/1	0.034	0.191	29.689	1.287	0	1.458	14.184	27.827	3.149	10.591	2.145	0.366	1.254	0.054	0.397	0.147	0.202	3.945	0.982	97.9	656	33
13/1	0	0.338	30.156	0.669	0	0.961	14.989	29.132	3.211	10.936	2.237	0.257	1.359	0.061	0.383	0.123	0.102	2.822	0.197	97.932	684	56
14/1	0.013	0.324	30.85	0.898	0	0.979	15.462	29.602	3.113	10.931	2.196	0.157	1.42	0.032	0.396	0.094	0.15	4.25	0.228	101.094	699	43
15/1	0	0.265	30.64	0.874	0	0.901	15.043	29.645	3.311	11.302	2.284	0.299	1.331	0.066	0.346	0.089	0.147	3.766	0.518	100.825	629	40
16/1	0.007	0.266	30.642	1.297	0	1.459	14.23	28.215	3.084	10.668	2.086	0.279	1.282	0.076	0.484	0.143	0.221	4.716	0.924	100.079	665	31
17/1	0	0.302	30.702	0.937	0	1.144	14.891	29.156	3.227	10.833	2.197	0.182	1.325	0.11	0.401	0.087	0.142	3.917	0.345	99.899	658	42
18/1	0.02	0.43	30.635	1.183	0	1.122	14.753	28.538	3.108	10.664	2.155	0.151	1.265	0.12	0.354	0	0.183	5.395	0.366	100.443	648	34
19/1	0	0.368	30.14	0.956	0	1.071	15.154	29.576	3.128	10.915	2.257	0.25	1.313	0.085	0.403	0.079	0.139	4.167	0.32	100.322	625	40
20/1	0.027	0.166	30.625	0.924	0	1.386	13.893	28.836	3.337	11.972	2.418	0.414	1.327	0.042	0.426	0.167	0.17	2.9	1.1	100.134	611	34
22/1	0.004	0.226	31.387	0.289	0	0.892	11.546	29.566	3.781	15.674	3.165	0.597	1.392	0	0.351	0.125	0.071	1.313	0.438	100.816	605	67
23/1	0.002	0.213	30.896	0.484	0	1.062	12.785	29.858	3.728	13.432	2.564	0.51	1.285	0.001	0.451	0.095	0.109	2.239	1.216	100.93	414	32
B5																						
1/1	0	0.238	30.462	1.875	0	0.511	14.152	27.311	2.959	10.051	2.11	0.31	1.274	0.026	0.193	0.107	0.359	6.256	1.566	99.76	730	25
2/1	0.015	0.231	30.216	1.857	0	0.574	13.911	27.294	2.875	10.126	2.181	0.31	1.318	0.074	0.17	0.133	0.362	6.709	1.651	100.03	694	24
3/1	0.001	0.454	30.122	0.962	0	0.183	15.558	29.05	3.068	10.45	2.277	0.217	0.898	0	0.049	0.149	0.195	5.413	0	99.048	840	41
4/1	0	0.449	29.771	1.257	0	0.373	14.939	29.215	2.955	10.266	2.118	0.288	1.073	0.004	0.129	0.145	0.217	6.523	0.061	99.783	755	35
5/1	0.012	0.693	29.605	2.31	0.371	0.13	13.39	25.292	2.766	9.454	2.079	0.256	0.937	0	0	0	0.47	11.636	0.212	99.613	886	24
6/1	0.005	0.682	29.721	1.67	0.045	0.152	15.462	27.579	2.797	9.584	2.065	0.213	0.862	0	0.032	0.002	0.346	11.228	0.11	102.553	698	23
8/1	0.037	0.239	30.113	0.901	0.394	0.4	16.538	30.486	3.037	10.086	1.998	0.186	0.645	0	0.06	0	0.161	4.287	0.619	100.188	597	35
9/1	0.001	0.267	29.943	0.932	0	0.46	11.178	28.877	3.529	13.474	2.948	0.675	1.657	0.039	0.125	0.226	0.171	4.217	0.643	99.363	633	37
10/1	0	0.268	30.391	1.643	0	0.7	12.089	25.091	3.032	11.691	3.387	0.774	1.842	0	0.171	0.135	0.345	6.52	1.019	99.099	810	29
11/1	0.013	0.245	29.724	0.483	0	0.215	11.975	31.327	3.727	13.73	2.763	0.709	1.134	0	0.088	0.14	0.108	4.691	0	101.073	540	41
12/1	0.012	0.217	29.998	0.632	0	0.258	15.579	31.393	3.218	11.226	2.197	0.331	0.769	0	0.078	0.069	0.096	3.177	0.012	99.261	701	56
13/1	0.04	0.52	29.624	1.312	0	0.204	13.971	25.433	2.923	9.216	1.916	0.22	0.691	0	0	0.062	0.276	5.875	0.498	92.782	851	36
14/1	0.01	0.199	29.382	1.61	0	0.391	14.61	28.064	2.998	10.142	2.083	0.235	1.079	0.057	0.069	0.078	0.377	5.378	2.273	99.037	683	22
15/1	0	0.21	29.503	1.445	0	0.408	14.715	28.447	2.918	10.356	2.149	0.359	1.224	0.01	0.069	0.103	0.311	5.148	1.613	98.987	692	26
16/1	0	0.562	29.764	1.386	0	0.353	6.292	23.07	3.657	16.195	4.95	1.268	2.81	0	0.249	0.304	0.248	5.625	0	96.733	1,022	44
17/1	0.001	0.308	29.433	1.421	0	0.365	14.731	28.287	2.935	10.189	2.192	0.31	1.366	0.048	0.187	0.092	0.243	5.851	0.51	98.468	753	34
18/1	0.001	0.229	29.762	0.373	0	0.387	11.945	31.411	3.737	13.632	2.87	0.641	1.383	0.012	0.16	0.158	0.042	1.676	0.039	98.458	550	83
19/1	0	0.185	29.631	0.305	0	0.258	14.709	33.041	3.58	12.213	2.205	0.326	0.783	0	0.059	0.113	0.015	0.934	0.025	98.382	337	79
20/1	0.011	0.141	30.028	1.5	0	1.055	14.02	27.623	2.995	10.187	2.172	0.346	1.271	0.028	0.35	0.061	0.297	5.249	1.408	98.74	699	27
21/1	0.009	0.273	29.455	1.188	0	0.357	5.987	23.398	3.772	17.472	5.205	1.465	3.084	0	0.137	0.483	0.193	5.693	0	98.171	794	41
22/1	0.013	0.145	29.898	0.38	0	0.34	10.432	30.642	4.009	15.437	3.271	0.827	1.378	0	0.161	0.189	0.08	2.185	0.717	100.104	418	43
23/1	0.003	0.16	30.132	1.155	0	0.836	14.28	29.978	3.015	10.669	2.209	0.396	1.215	0.026	0.3	0.177	0.228	4.659	0.873	100.311	706	33
24/1	0.005	0.251	29.738	1.907	0	0.818	13.93	26.924	2.79	9.418	1.975	0.278	1.191	0.017	0.107	0.168	0.42	6.257	2.071	98.263	745	23
25/1	0.015	0.268	29.615	1.74	0	0.431	14.521	27.633	2.87	9.633	2.011	0.278	0.988	0	0.099	0.137	0.391	5.639	2.065	98.334	731	23
26/1	0.012	0.234	29.226	0.753	0	0.101	18.321	30.611	2.975	9.269	1.735	0.108	0.667	0	0.014	0.094	0.147	3.749	1.573	99.592	392	24
27/1	0.003	0.417	29.382	1.226	0	0.849	14.987	27.909	2.834	9.607	1.984	0.238	1.24	0.028	0.267	0.086	0.257	5.512	0.536	97.361	821	35
28/1	0.027	0.414	29.135	1.229	0	0.39	15.528	28.667	2.869	9.648	2.103	0.307	1.266	0.001	0.162	0.103	0.204	5.525	0.95	98.527	555	28
29/1	0	0.195	29.725	0.553	0	0.461	18.251	30.346	2.921	9.294	1.822	0.119	0.954	0.003	0.227	0.139	0.159	3.734	0.608	99.51	650	38

(Continued on following page)

TABLE 4 | (*Continued*) EPMA analytical result of monazite for the samples CG-1 (26,014′12″/,74,013′25″), B-4 (26,013′44″/,74,013′12″), B-5 (26,013′27″/,74,013′12″), and R-4 (26,012′56″/,74,018′30″).

CG1 Point	Al_2O_3	SiO_2	P_2O_5	CaO	FeO	Y_2O_3	La_2O_3	Ce_2O_3	Pr_2O_3	Nd_2O_3	Sm_2O_3	Eu_2O_3	Gd_2O_3	Tb_2O_3	Dy_2O_3	Tm_2O_3	PbO	ThO_2	UO_2	Total	Age (Ma)	Age err
30/1	0	0.225	29.364	0.567	0	0.259	15.687	31.8	3.048	10.326	2.028	0.234	0.735	0	0.09	0.131	0.095	2.607	0.001	97.196	845	68
31/1	0.072	0.424	29.315	1.11	0	0.255	12.606	28.872	3.081	10.519	2.122	0.364	0.854	0	0.096	0.142	0.235	5.384	0.128	95.58	941	43
32/1 R4	0.023	0.291	29.58	0.712	0	0.278	15.367	32.073	3.097	10.544	2.028	0.287	0.673	0	0.082	0.087	0.069	1.841	0.037	97.07	813	88
1/1	0	1.119	29.458	1.104	0	1.458	12.411	26.031	2.669	11.349	2.445	0.814	1.586	0	0.55	0	0.324	8.361	0.113	99.794	864	27
2/1	0.011	0.448	31.529	0.973	0	1.672	13.301	28.869	2.796	11.075	2.283	0.858	1.406	0	0.523	0	0.191	4.861	0.328	101.122	749	35
3/1	0.014	0.784	30.181	0.801	0	1.33	13.174	28.809	2.808	11.601	2.538	0.894	1.632	0	0.538	0	0.2	5.027	0.11	100.439	864	39
4/1	0.01	0.416	30.574	0.853	0	1.321	13.696	29.516	2.977	11.316	2.446	0.908	1.513	0	0.486	0	0.171	4.377	0.178	100.756	803	41
5/1	0	0.803	29.722	0.843	0	1.343	13.104	28.157	2.883	11.543	2.523	0.884	1.648	0	0.511	0	0.235	6.101	0.111	100.411	847	34
6/1	0.074	0.574	30.597	1.078	0	1.727	12.249	28.236	2.765	11.274	2.382	0.804	1.495	0	0.547	0	0.214	4.96	0.567	99.544	732	34
7/1	0.031	0.463	30.382	1.019	0	1.814	13.039	28.475	2.806	10.955	2.29	0.823	1.412	0	0.549	0	0.213	5.35	0.354	99.975	760	33
8/1	0.004	0.539	30.646	0.744	0	1.278	13.434	29.409	2.893	11.517	2.448	0.903	1.522	0	0.545	0	0.171	4.491	0.111	100.656	818	42
9/1	0.007	0.303	31.227	1.134	0	1.672	12.482	28.538	2.879	11.436	2.478	0.893	1.508	0	0.526	0	0.197	4.716	0.515	100.51	717	33
10/1	0	0.497	30.731	1.036	0	1.463	12.879	28.546	2.821	11.084	2.324	0.94	1.485	0	0.482	0	0.217	5.632	0.252	100.391	783	33
46/1	0	0.478	30.367	0.874	0	1.348	13.157	28.849	2.896	11.248	2.366	0.873	1.44	0	0.473	0	0.186	4.81	0.203	99.57	792	38
47/1	0.005	0.463	30.426	0.968	0	1.368	13.395	28.943	2.806	11.031	2.412	0.818	1.402	0	0.515	0	0.191	4.968	0.19	99.902	795	37
48/1	0.013	0.474	30.348	0.842	0	1.34	13.438	29.139	2.876	11.206	2.405	0.857	1.354	0	0.499	0	0.179	4.596	0.172	99.739	807	40
49/1	0	0.476	30.826	0.881	0	1.399	13.519	29.308	2.911	11.094	2.404	0.823	1.461	0	0.496	0	0.177	4.765	0.203	100.741	758	37
50/1	0	0.482	30.512	1	0	1.466	13.18	28.687	2.82	11.104	2.365	0.831	1.379	0	0.485	0	0.21	5.506	0.243	100.271	775	39

Sewariya Pluton

It indicates a higher % of SiO_2 (75.35–78.68), moderate to high Fe_2O_3 (0.74–1.03), moderate to high Al_2O_3 (10.81–13.73), and lower Na_2O compared to K_2O. The A/NK and A/CNK values are >1.0. The CIPW norm shows normative quartz, diopside, albite, corundum, and ilmenite (**Table 2**). The rock lies in the per-aluminous field in the A/NK vs. A/CNK plot (**Figure 5A**) and S type field in the Na_2O vs. K_2O and TiO_2 vs. Zr plot (**Figures 5B,C**) (Chappell and White, 1992) and calc-alkaline to calcic field in Na_2O + K_2O-CaO vs. SiO_2 plot (**Figure 5D**) (cf. Frost et al., 2001). The Na_2O + K_2O–(CaO + MgO) *5 Fe_2O_3 (t) * 5 ternary plot (**Figure 5F**) shows the sample lies in "island arc to continental arc setting" with few in the rift setting (Grebennikov, 2014). The Zr values range from 29 to 130 ppm indicating Zr saturation temperature is around 700 to 800 °C (cf. Watson and Harrison, 1983).

Geochemistry of the granites and metarhyolite can be summarized as the Pratapgarh pluton is meta-aluminous, I type, and emplaced in intraplate rift setting; metarhyolite is peralkaline, I type, and emplaced in intracontinental rift setting; these intruded during pre-D_1 stage. The Sewariya granite is peraluminous, S type, and emplaced in syncollisional setting, syn-D_1.

Zircon Geochronology

5.2.1 Sample No. TKB-1

The sample is collected from the gneissic part of the Sewariya pluton near Bar, where high temperature solid state fabric is prominently developed (**Figure 2A**). The zircon crystals are subangular in shape. The CL image reveals oscillatory zoning patterns, consistent with magmatic zircon (**Figure 6**, textural details in Appendix). The isotopic data plot in a well-defined cluster on Concordia, with two analyses within that population plotting with larger errors and off Concordia, corresponding to the two analyses with the highest f_{206} (**Figure 7**, TKB1-25, TKB1-26, TKB-1). The concordant points correspond to a Concordia age of 878 ± 9 Ma, which we take to be the best estimate for the emplacement age of the granitoid. One analysis, TKB1-14, plots well away from the Concordia age and corresponds to a darker CL zircon (**Figure 6**), with a $^{207}Pb/^{206}Pb$ age of 1,634 ± 22 Ma (2σ confidence, 101% concordant, **Figure 7** TKB-1). This represents the xenocrystic component age.

Sample No. TKB-2

The sample is collected from Rupnagar metarhyolite (**Figure 2C**). The rock is foliated with close spaced S_1 fabric. The zircon grains are dominantly subangular to subrounded. The CL image reveals oscillatory zoning patterns, consistent with magmatic zircon (**Figure 6**, textural details in Appendix). The data plot in a well-defined cluster on Concordia (**Figure 7**), with the exception of TKB-2–15 and TKB-2–17, which record the highest f_{206} values and plot off Concordia. The concordant population of 27 zircons defines a Concordia age of 982 ± 3 Ma, which is the best approximation of the emplacement age of the granite protolith.

Sample No. TKB-3

The sample belongs to the Pratapgarh granite pluton (**Figure 2B**). The zircon grains are subangular in shape, with some subrounded zircon. The CL image reveals relatively low response, with dark oscillatory zoning patterns, consistent with magmatic zircon (**Figure 6**, textural details in Appendix). Twenty-one analyses were conducted on twenty-one zircons and resulted in variable f_{206} values between 0 and 21.7%. One zircon (TKB-3–16) recorded very high U and Th values, but the Uranium and Thorium content for all other zircons range between 100 and 1802 and 29 and 1,071 ppm, respectively (**Table 3**), resulting in Th/U ratios between 0.02 and 1.96. The lowest Th/U values were recorded on angular euhedral zircon with clear oscillatory patterns, and the overall range of Th/U values and CL patterns suggest the zircon to be magmatic in character. Two zircon grains record older $^{207}Pb/^{206}Pb$ ages, with the one near-concordant point (TKB-3–7) giving an age of 2,765 ± 18 Ma. These are considered to record some xenocrystic components in the granite protolith (**Figure 7**). The remaining points plot along a Pb-loss trend anchored at an upper concordant cluster with a Concordia age of 992 ± 12 Ma (**Figure 7**). The Pb-loss pattern is consistent with present-day loss.

Sample No. TKB-4

The sample is collected from Sumel granite (**Figure 2C**). The zircons range from euhedral crystals to irregular shape indicating the presence of various xenocrystic components. Faintly observable oscillatory zoning suggests magmatic growth (**Figure 6**, textural details in Appendix). One analysis yielded an older age of ca 2,890 ±87 Ga, but plots slightly under Concordia (TKB- 4–3, **Figure 7**). This grain is interpreted to reflect a xenocrystic component in the granite dyke. The remaining analyses mainly plot along a broad Pb-loss trend, with the highest U grains plotting inversely discordant (**Figure 7**). The trend appears to be subparallel to Concordia and most likely related to ancient Pb-loss, possibly during intrusion of the regional granite suites or during subsequent metamorphism. The oldest cluster of concordant grains in the population and also the zircon with the lowest f_{206} provide a Concordia age of 946 ± 18 Ma, which could reflect the emplacement age of the granite dyke. One zircon (TKB-4–7), analyzed twice during the session, provides a concordant data point at 270 ± 12 Ma and corresponds to a subangular zircon grain with faint sector zoning. This young grain would put the age of emplacement of the granite dykes at 270 Ma, with the older populations reflecting inheritance of ca. 950 Ma aged zircon, recording Pb-loss due to a metamorphic event either at or before 270 Ma.

Zircon geochronology suggests that the granites of the study area were emplaced during two distinct periods, one at 992–946 Ma and the other at ca. 878 Ma (**Table 1**). The former is pre-D_1 while the latter is syn -D_1. The granite carries xenocrysts from the basement rock showing ages ca. 1,634 Ma, ca. 2,765 Ma, and ca. 2,890 Ma. The intrusion of pegmatite veins in the granite along fractures is ca.270 Ma.

Monazite Geochronology

Sample No. CG1

The sample belongs to mica schist mylonite of the Phulad thrust. The mylonite is foliated containing dynamically recrystallized elliptical quartz grains arranged oblique to the mylonitic foliation; these oblique grains define mylonitic S foliation. The monazites are elliptical in shape and occur oblique to the C fabric indicating its synshearing recrystallization (**Figure 8A**). The monazite grains contain domains; the lighter domain shows low Y and high Th values and produces an age of 813 Ma to 716 Ma (**Figures 8B–D**). This age corresponds to D_2 events. The darker domain contains fractures and produces an age of ca. 590 Ma suggesting the age of brittle deformation event. Isochron plot and probability curve indicate three events 819–680–588 Ma and 811–700–569 Ma, respectively (**Figures 8E,F**). The D_2 deformation and thrusting belong to ca 811–680 Ma and the brittle deformation is at ca. 588–569 Ma.

Sample No. B4

The sample is collected from pre-Delhi upper amphibolite facies slivers emplaced within Phulad thrust; there are several elliptical monazite grains aligned parallel to the mylonitic foliation (**Figures 8G,I**). Grains are fractured along the edge and yield ages as ca. 706 Ma and 550 Ma (**Figure 8H**), indicating age of the D_2 and D_4 brittle deformation events, respectively. In addition, several rounded grains (**Figure 8J**) resembling the rounded garnet grains (**Figure 4C**) occur in the rock. These monazite grains crystallized during pre-Delhi metamorphism and yield higher ages as 1,595 to 1,638 Ma. Isochron and probability curve indicate two age clusters (**Figures 8K,L**). The pre-Delhi metamorphism is at ca. 1,611–1,609 Ma and the D_2 is at ca. 704–686 Ma.

Sample No. B-5

The sample is collected from the mica schist, west of Babra. The monazite grains are equant in shape with moderate to low ellipticity (**Figures 9A–D**). They occur parallel to S_1 fabric in the rock and developed during D_1-M_1. It contains domains; the lighter domains, lying at the outer edge of the grain, are Y poor and Th rich and yield higher age as ca. 886 Ma while the darker domains, present in the center of the grain, show ages as ca. 783–597 Ma (**Figure 9B**). Fracture along the grain margin channelized the fluid into the core of the grain resulting in rejuvenation of the age. There are three isochrons indicating as many events as 864 Ma for D_1, 718 Ma for D_2, and 588 Ma for brittle deformation (**Figure 9E**). Probability graph indicates three peaks at ca. 846, 697, and 564 Ma (**Figure 9F**), for D_1, M_1, and D_2 and brittle deformation events, respectively.

Sample No. R4

The sample is collected from the mica schist (**Figure 9G**) close to the Pratapgarh. The monazite grains occur within biotite and are rounded to ellipsoidal with compositional domains (**Figures 9H–J**). The Y low/high Th domains yield higher ages as ca. 863 Ma corresponding to D_1-M_1, and Y poor domains yield ca. 792 Ma corresponding to D_2 (**Figure 9H**). The isochrons indicate two ages ca. 865 and 720 Ma (**Figure 9K**) and probability curve

contains peaks at ca. 852 and 743 Ma (**Figure 9L**) corresponding to D_1 and D_2, respectively.

The result of the monazite geochronology can be summarized that the D_1-M_1 is ca. 865 Ma; it continued up to 846 Ma. The D_2 is ca. 811–680 Ma and D_4 brittle deformation is ca. 588 to 564 Ma. The pre-Delhi deformation and metamorphism were at 1,638 Ma (**Table 1**). The D_1 deformation age nearly coincides with D_1 age derived from zircon age of Sewariya granite (878 Ma). Combining these ages, we define the D_1-M_1 age as 878–846 Ma. The D_2 event included both folding and thrusting. Therefor a spread in ages is indicated (811–680 Ma). Thrusting is marked by fluid flow and therefore resets the ages to ca. 680 Ma, in most cases. Therefore, we are taking ca. 680 Ma as the lower age limit for thrusting. The roll of D_3 deformation cannot be ruled out for such wide spread of ages. The age of D_4 deformation is at ca 588–564 Ma.

DISCUSSION

Tectonic Setting of Metarhyolite and Granite

The Chang, Sendra, and Pratapgarh plutons (**Figure 2C**) intruded the calcareous schist and folded the surrounding rocks in the core of the SDT, showing similar geochemical character and isotopic age (Tobisch et al., 1994; Pandit et al., 2003, Tiwana et al., 2019; present study). Previous studies by Pandit et al. (2003) and Tiwana et al. (2019) suggest that these are A2-subtype granites (cf. Eby, 1992) and are generated from subcontinental lithosphere or lower continental crust in postcollisional or postorogenic settings, perhaps during late-stage extensional collapse. Based on initial Sr isotope composition (0.710), the Chang pluton was suggested to be derived from basic magmatic source, produced from remelting of Archaean Banded Gneissic Complex in an Andean type magmatic setting (Pandit et al., 2003). The plutons were metamorphosed during South Delhi orogeny. Our study suggests that the Pratapgath granite is meta-aluminous, I type, and calc-alkaline (**Figure 5**) and was produced from the remelting of basic igneous rocks at 750–800°C (zircon saturation temperature). Further, Rb, NB, and Y values indicate the granite to represent within plate magma intruded in intracontinental rift setting. These led to implication that the post-Aravalli (globally post-Columbia and Grenvillian) rifting of the Marwar Craton formed the South Delhi basin and granite was intruded in the basin in an extensional setting. Rupnagar metarhyolite was studied for the first time by us. It occurs as synsedimentary lava flows. Geochemical data indicates it is peralkaline, I type, and alkalic to alkali-calcic composition (**Figure 5**). The Rb- Nb-Y and $Na_2O + K_2O$–(CaO + MgO) *5 Fe_2O_3 (t) * 5 plot shows within plate magma intruded in a continental rift setting. This implies that the rifting of the Marwar Craton led to alkali volcanism in the South Delhi basin. The Sewariya pluton exhibits a different tectonic setting altogether. Previous study (Bhattacharjee et al., 1993; Ray et al., 2015; Sivasubramaniam et al., 2019) shows that the granite is peraluminous being produced from melting of Delhi metasediments at higher water pressure (3 kb) at 750°C by muscovite breakdown reaction in a subduction zone setting. More peraluminous nature implies there is little contribution from mantle (Ray et al., 2015). Our study finds similar result as the granite is peraluminous, S type, more calcic, and syncollisional in nature (**Figure 5**). However, some of the analysis lies in rift setting (**Figure 5F**). Collision/subduction of the South Delhi Terrane resulted in the melting of the Delhi metasediments and produced such granite.

Life Span of South Delhi Orogeny

The South Delhi orogeny is constrained by multiple proxies as deformation, metamorphism, geochemistry, and geochronology of pre- and synorogenic granites and tectonometamorphic fabric. The study area is represented by greenschist facies rocks which are intruded by two phases of granites; the Sewariya granite is the youngest. All the plutons carry the imprint of D_1 deformation; hence the D_1 deformation cannot be older than Sewariya pluton. Geochemically it is S type and produced in a syncollisional setting. In addition, we have illustrated that the Sewariya pluton shows a transition from magmatic/submagmatic to solid state deformation fabric S_1, from core to the margin. At the margin it shows perfect coupling with S_1 fabric in the host mica schist. This is an evidence of syntectonic (syn-D_1-M_1) nature of granite intrusion. The granite yields a zircon age of ca. 0.87 Ga that marks the initiation of the South Delhi orogeny. We did the monazite dating of tectonometamorphic fabric which further constrains the D_1-M_1 age at ca. 0.86–0.84 Ga. The D_2 event is constrained at ca. 0.81 to 0.68 Ga. Though D_3 event could not be dated, the spread in D_2 ages (nearly hundred years) may be partly due to the D_3 event. Considering all these ages, it is suggested that the South Delhi orogeny is ca. 0.87–0.68 Ga old and much younger than the Grenvillian orogeny (1.3 Ga to 1.0 Ga/Li et al., 2008) and may be synchronous with early phase of Pan-African orogeny (ca. 0.9–0.7 Ga, Rogers and Santosh, 2002; Kroner and Stern, 2005; Rino et al., 2008; , Singh et al., 2010; Tiwari and Biswal, 2019a). The postorogenic brittle deformation in the SDT belongs to ca. 0.58–0.56 Ga that coincides with the period of Kuunga orogeny (0.65–0.5 Ga, Meert, 2003; Pradhan et al., 2009) representing the later part of Pan-African orogeny (Ambaji area, 0.76–0.65 Ga, Tiwari and Biswal, 2019b; Pali area, ca. 0.6 Ga, Bhardwaj and Biswal, 2019).

Our study shows a similarity with other parts of the SDT. The D_1 event was dated at ca. 0.87–0.86 Ga and thrusting at ca. 0.81–0.78 Ga from Ambaji area (Tiwari and Biswal, 2019a) and thrusting at ca. 0.81 Ga from Phulad area (Chatterjee et al., 2017). Further, on the eastern flank of the SDT near Srinagar, the granite bears post-0.98 Ga deformation imprint (Ruj and Dasgupta, 2014; Bose et al., 2017). The Sirohi Terrane in the west of SDT shows a deformation age between 0.89 and 0.8 Ga (Arora et al., 2017).

Earlier view that the South Delhi orogeny is Grenvillian comes from 1.0 Ga age of Pratapgarh, Sumel, Chang, and Sendra plutons (0.98 Ga, Tobisch et al., 1994; 0.96 Ga/Pandit et al., 2003; 0.97 Ga/ Tiwana et al., 2019), but geochemistry of these granites suggests that these are I type, produced from remelting of basic rocks, and intruded in postorogenic intracontinental extensional setting. The granites lack magmatic fabric, deformed by all phases of

deformation as the metasediments and metamorphosed in greenschist facies. The plagioclase and K-feldspar retained their magmatic habit. Based on these we interpret that these plutons are preorogenic to SDT and intruded at the time of rifting of South Delhi basin. As far as age of rifting and sedimentation are concerned, previous study on SDT constrained it at ca. 1.7–1.0 Ga (Wang et al., 2014) and ca. 1.2–0.86 Ga (Singh et al., 2010). Our study on the Rupnagar metarhyolite that stands as an unequivocal evidence of synsedimentary bimodal volcanism like many in the SDT (Bhattacharjee et al., 1988) provides an age of 0.98 Ga that lies within the above age range. Thus, the rifting and formation of South Delhi basin overlap with Rodinia amalgamation event (ca. 1.3–0.9 Ga). Hence, while many continents were experiencing orogenic event, the SDT was undergoing rifting.

Another viewpoint that advocates the South Delhi orogeny to be Grenvillian is the 1.0 Ga metamorphic imprint on 1.7–1.5 Ga old granulite of the Pilwa-Chinwali area. As these outcrops occur in the north of the study area Bhowmik et al. (2018) considered the granulite to be part of SDT. However, Fareeduddin et al. (1994) suggested the granulite to be pre-Delhi and belongs to Sandmata Terrane. Our finding suggests that the upper amphibolite grade slivers of ca. 1.6 Ga (equivalent to Pilwa-Chinwali granulite) occur within SDT as tectonic inclusions along the Phulad thrust. The mineral assemblage is in sharp contrast with the surrounding mica schist. We suggest that the Pilwa-Chinwali granulite represents basement for the SDT and it has been exhumed by thrusting and normal faulting along Govindgarh-Jethana fault. Further, the xenocrysts in the Pratapgarh and Sewariya granites yield similar ages (ca. 1.6 Ga, 2.7 Ga, and 2.8 Ga). Furthermore, the Beawar gneiss occurs as exhumed basement block to the east of the study area and shows the age as ca. 0.8 Ga, 1.0 Ga, 1.6 Ga, and 2.8 Ga old (Kaur et al., 2020). Hence 1.0 Ga metamorphic event is an event in the basement not in the SDT.

South Delhi Orogeny in Relation to East Gondwana Tectonics

The East Gondwana includes much of the continents of Australia, India, and Antarctica, which underwent several phases of amalgamation and separation in the Proterozoic period (Fitzsimons, 2000; Collins and Pisarevsky, 2005; Pradhan et al., 2009). It was not a coherent mass during much of Rodinia and Gondwana amalgamation; they finally joined together in Neoproterozoic-Cambrian period in bits and pieces. Thus, individual continents in the assembly were not even completely amalgamated; this is proven from India (Collins and Pisarevsky, 2005). For example the Eastern Ghats Mobile Belt provides evidence for final suturing between India and Antarctica during Cambrian (ca. 0.51 Ga/Biswal et al., 2007). The present study on SDT points to amalgamation of Marwar Craton with Bundelkhanda Craton during Neoproterozoic (ca.0.87 Ga). Based on our finding we are proposing a model for the SDT in reference to amalgamation of Rodinia and Gondwana, using the reconstruction of Supercontinents proposed by several researchers (**Figure 10**, cf. Powell and Pisarevsky, 2002; Li et al., 2008; Meert et al., 2013; Johansson, 2014; Pisarevsky et al., 2014; Oriolo et al., 2017).

i. Before 1.0 Ga (**Figure 10A**): At 1.2 Ga India was in the polar latitude (Pradhan et al., 2009) as a separate landmass, away from Rodinia Supercontinent. By then, the Dharwar Craton of India was separated from Sarmatia at 1.3 Ga, the eastern margin of India was not connected to Antarctica and Australia, and the Marwar Craton, Madagascar, and Syechelles were bordering the western margin of India (Pisarevsky et al., 2013). The Arabian-Nubian shield was located to the south (**Figure 10**).
ii. Ca. 1.0–0.9 Ga (**Figure 10B**): Grenvillian orogeny took place, consequently India amalgamated with Antarctica, the Eastern Ghats Mobile Belt and Rayner Complex formed through subduction and collision (Dasgupta et al., 2013), and in turn Antarctica and Australia amalgamated with the Laurentia completing the assembly of the Rodinia. Thus Eastern Ghats Mobile Belt is considered to be a Grenvillian Mobile Belt. Further, the NW India witnessed discrete metamorphic events, e.g., Sandmata Terrane (Bhowmik and Dasgupta, 2012) and North Delhi Terrane (Pant et al., 2008) of the ADMB. Following this, the NW India underwent extension and rifting reflecting a top-down process (e.g., Cawood et al., 2016).
iii. After Rodinia (**Figure 10B** inset-1): Extension led to rifting in the Marwar-Aravalli-Bhilwara-Bundelkhanda Craton in NW India forming South Delhi basin. A simple shear extension model (cf. Wernicke, 1985) with westward inclined detachment probably created the South Delhi basin (Biswal et al., 1998a, b). In the simple shear model, the rotation of the faulted blocks is easier due to listric nature of the detachment fault which is steeper at the surface and gradually becomes gentler and horizontal at brittle-ductile boundary. This type of model has been applied to Basin and Range province, Bay of Biscay, and northwestern European continental shelf (Montadert et al., 1979; Kusznir et al., 1987; Lister et al., 1991). However, a pure shear model as proposed by McKenzie (1978) cannot be ruled out. In the pure shear model, lithospheric stretching takes place through conjugate planar faults. The slips along conjugate faults oppose each other (Ramsay and Huber, 1987) which is not there in a listric detachment fault postulated in the simple shear model. However, mechanism of basin formation is beyond the scope of the paper. The sediments were deposited in fault-bounded basin. Thick erosional unconformity with conglomerate formed at several parts of the SDT. Biomodal volcanism produced rhyolite and basalt flows (Rupnagar metarhyolite) which are dated at ca. 0.98 Ga in the study area. Granites emplaced in extension setting, namely, Bilara granite and Sendra-Chang-Pratapgarh-Sumel plutons at ca. 1.0–0.9 Ga. With progressive lithospheric stretching, the MOR developed on the east (**Figure 10C** inset −1); the Phulad ophiolites, Ranakpur diorite, and Sirohi plagiogranite (ca. 1.0 Ga, Volpe and Macdougall, 1990; Dharma Rao et al., 2013) were part of the oceanic crust. This represents the

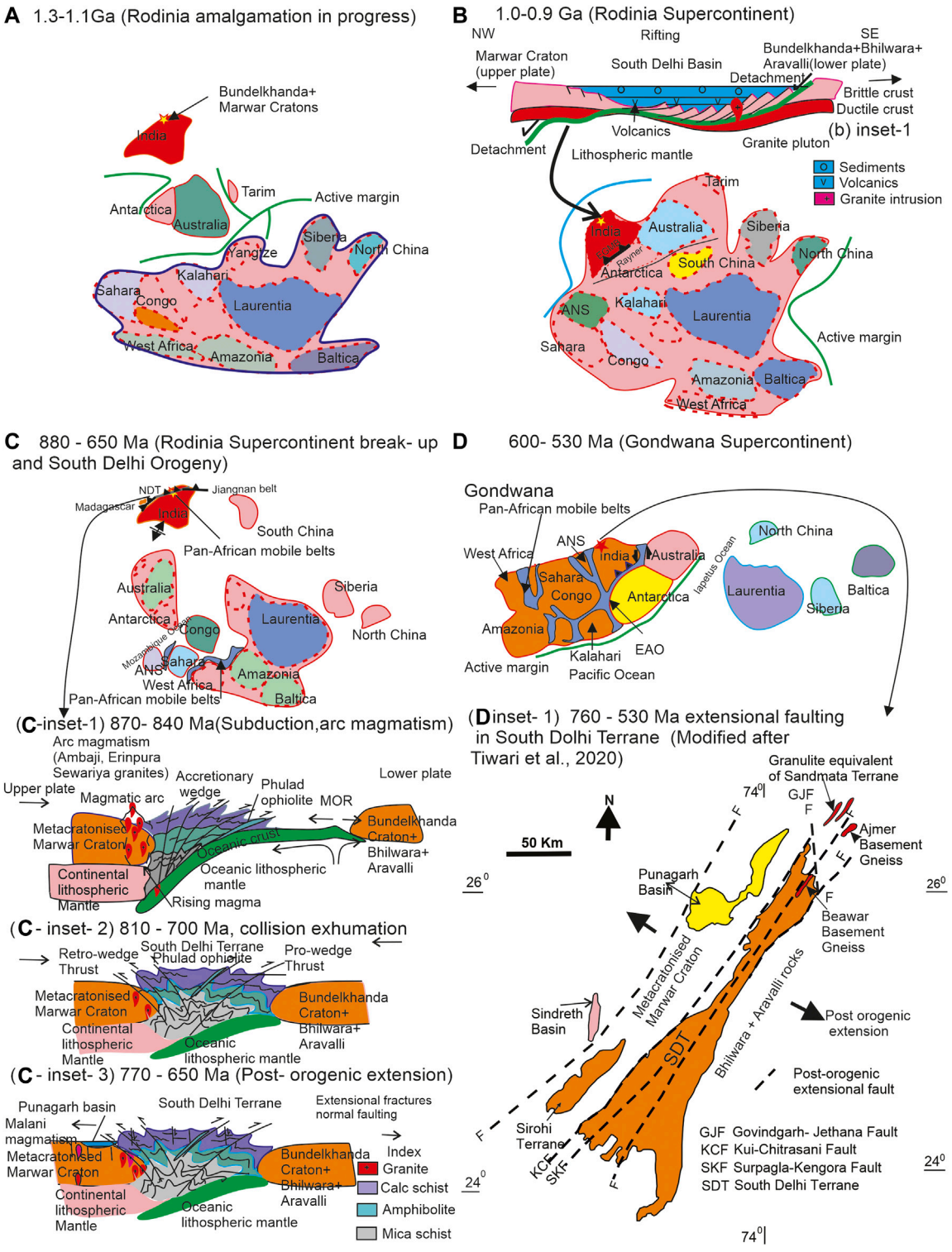

FIGURE 10 | Cartons showing position of India during continental assembly and breakup. **(A)** 1.3–1.1 Ga, Rodinia was under amalgamation; India separated from Baltica, drifted to join Antarctica and Australia. **(B)** East Gondwana continents amalgamated to complete Rodinia assembly by 1.0 Ga. Eastern Ghats Mobile Belt developed in the SE margin of India by subduction/collision between India and Antarctica. Synchronously, the NW margin of India underwent internal rifting that led to the formation of South Delhi basin. A simple shear model has been proposed for basin opening (**Figure 10B**, inset 1) (e.g., Wernicke, 1985, model drawn cf.; Allen and Allen, 2013). The sediments were laid down with a prominent erosional unconformity over granitic basement, marked by conglomerate and paleosol. Further, bimodal volcanism (982 Ma) occurred and granite plutons (992–946 Ma) intruded in the basin, **(C)** Ca 880 Ma, Rodinia broke up; East Gondwana continents were drifted apart.

(*Continued*)

FIGURE 10 | Synchronously, the South Delhi basin closed by subduction/collision, to form SDT, pro- and retro-wedge thrust belts formed. The study area belongs to retro-wedge part (C, insets 1, 2, 3, model of subduction, collision, and extension, cf. Allen and Allen, 2013), **(D)** Ca. 600 -530, East and West Gondwana continents amalgamated to form Gondwana. The SDT experienced brittle tectonics during this period. Number of faults developed (D, inset 1). The Eastern Ghats and several other, Columbia-Rodinia related mobile belts of Peninsular India were overprinted by ca. 0.5 Ga brittle as well as ductile deformation. Brittle tectonics continued till 270 Ma when Gondwana broke up; pegmatite veins in the SDT bear testimony for that.

introversion tectonics as the juvenile crust formed out of such rifting is younger than the age of the breakup (cf. Murphy and Nance, 2013).

iv. Rodinia breakup and South Delhi orogeny (0.88–0.65 Ga, **Figure 10C**). Rodinia broke up and India was detached from Antarctica and Australia along Eastern Ghats and was placed near the north pole by 0.82 Ga (Powell and Pisarevsky, 2002). Breakup of Rodinia gave rise to the opening of major oceans, namely, Mozambique Ocean (**Figure 10C**) and Iapetus Ocean (**Figure 10D**) (e.g., Cawood et al., 2001; Meert and Torsvik, 2003; Li et al., 2008). However, the SDT witnessed subduction/collision between Bundelkhanda + Aravalli Craton and Marwar Craton. The oceanic crust was subducted westward forming continental arc with granite magmatism ranging in ca 0.87–0.76 Ga (**Figure 10C**, inset 1,2) (Erinpura granite, Ambaji granite, and Sewariya granite, Malani Igneous Suite; Sinha Roy, 1988; Sugden et al., 1990; Synchanthavong and Desai, 1977; Biswal et al., 1998b; Singh et al., 2010). Possibly, the detachment zone in the basin converted to a northwesterly dipping subduction zone/collision zone. Seismic reflection data support a NW dipping thrust plane at the contact between SDT and Sandmata Terrane (Satyavani et al., 2004). The magmatic arc was extending upto Madagascar in the south (Singh et al., 2010) and South China in the north (Zhao et al., 2018) as indicated by the presence of similar age granite (ca. 0.7 Ga, Singh et al., 2010) in those far-off continents (**Figure 10C**). The Marwar Craton, which was forming the overriding plate, was completely metacratonized by intrusion of these granitic rocks. The metacratonization was so extensive that Archean outcrops are hardly survived in Marwar Cratonic domain; the Azania block in Madagascar may be the survived part of extensive Marwar Craton (Singh et al., 2010). Along the magmatic arc, several low grade metasedimentary outcrops (roof pendants) occur within expansive granite outcrops, which constitute the Sirohi Terrane (**Figure 1B**). With progressive subduction/collision, compression led to exhumation of rocks at 0.81–0.68 Ga by thrusting (cf. Tiwari and Biswal, 2019a). The SDT is marked by pro- as well as retro-wedge thrust belts (cf. Naylor and Sinclair, 2008). The study area Beawar-Babra sector belongs to retro-wedge thrust belts while the eastern part around Shyamgarh (**Figure 2A**) belongs to pro-wedge thrust belt, together forming a doubly-vergent orogen (Hahn et al., 2020)

v. The SDT type Tonian-Cryogenian (1.0–0.72 Ga) rifting occurred between landmasses in the West Gondwana (Oriolo et al., 2017). The Arabian-Nubian shield shows signature of ca. 0.88–0.7 Ga accretion of island arcs and juvenile crust (Kroner and Stern, 2005); the Dahomey Belt has subduction with associated back-arc extension and development of island arc (Ganade et al., 2016); Borborema Province has ca. 0.85–0.75 Ga juvenile material (Ganade de Araujo et al., 2014) and the São Gabriel Block has ca. 0.9–0.7 Ga old intraoceanic subduction (Fortes de Lena et al., 2014).

vi. Ca.0.6–0.53 Ga (Amalgamation of Gondwana Supercontinent): Collision and strike-slip shearing led to amalgamation of different Gondawana blocks along Pan-African orogens (**Figure 10D**). The Mozambique ocean closed through Kuunga orogeny (0.65–0.5 Ga), bringing together the West and East Gondwana continents along East African Orogen (**Figure 10D**, Collins and Windley, 2002; Meert, 2003). India initially joined with Australia at ca. 0.6 Ga through strike-slip shearing (Powell and Pisarevsky, 2002) and later at 0.53 with Antarctica through collision. The Eastern Ghats Mobile Belt thrusts over Bastar Craton along the terrane boundary shear zone at 0.51 Ga (TBSZ, Biswal et al., 2007). During this period, the SDT experienced extensional tectonics (**Figure 10D** inset-1) that produced several prominent faults, namely, Kui-Chitraseni fault, Surpagla-Kengora fault, and Govindgarh-Jethana fault. Extensional basins like Sindreth and Punagarh developed in the intra-arch region (**Figure 10C**, inset-3, cf. Schobel et al., 2017). The brittle tectonics in the ADMB continued till the breakup of Gondwana. The N-S fractures that host 0.27 Ga pegmatite veins in the study area probably belong to Gondwana breakup period.

CONCLUSION

(1) We applied the tectonic fabric and geochemistry of the granite and metarhyolite in combination with zircon and monazite geochronology to date the South Delhi orogeny. The Pratapgarh-Sumel granite plutons intruded in extensional setting during rifting, Rupnagar metarhyolite extruded during sedimentation, and all these yielded an age of ca. 992–946 Ma. The Sewariya granite is syncollisional and produced an age of ca. 878 Ma. It is syntectonic with D_1 as indicated by coplanar attitude of magmatic Sm and S_1 fabrics. The monazite geochronology estimated the age of D_1-M_1 metamorphism at 865–846 Ma, the D_2 at 810–680 Ma, and brittle deformation D_4 at 588–564 Ma. We suggest that the South Delhi orogeny is ca. 878 to 680 Ma old and coeval with early part of the Pan-African orogeny.

(2) The South Delhi orogeny brought amalgamation of the Marwar Craton with Aravalli-Bhilwara-Bundelkhanda Craton that led in process to forming a united Indian

subcontinent, in the East Gondwana assembly. This strengthens the view that the East Gondwana blocks were sutured in bits and pieces till Neoproterozoic-Cambrian period.

(3) The Marwar Craton was extensively metacratonized by ≤878 Ma granites during South Delhi orogeny so that the Archaean rocks are totally lost from the cratonic domain. Similar metacratonization is also observed in Mangalwar and Sandmata terranes during Aravalli orogeny. Migmatization of Archean rocks and intrusion of charnockitic magma completely reset the age of the rocks in those terranes to Mesoproterozoic.

DATA AVAILABILITY STATEMENT

The original contributions presented in the study are included in the article/**Supplementary Material**, further inquiries can be directed to the corresponding authors.

AUTHOR CONTRIBUTIONS

All authors listed have made a substantial, direct, and intellectual contribution to the work and approved it for publication.

ACKNOWLEDGMENTS

The authors acknowledge the Department of Earth Sciences, IIT Bombay, for financial support during field work. Reviewers are profusely thanked for their constructive comments that helped in improving the MS.

SUPPLEMENTARY MATERIAL

The Supplementary Material for this article can be found online at: https://www.frontiersin.org/articles/10.3389/feart.2020.594355/full#supplementary-material.

REFERENCES

Allen, C. M., Williams, I. S., Stephens, C. J., and Fielding, C. R. (1998). Granite genesis and basin formation in an extensional setting: the magmatic history of the Northernmost New England Orogen. *Aust. J. Earth Sci.* 45 (6), 875–888. doi:10.1080/08120099808728442

Allen, P. A., and Allen, J. R. (2013). *Basin analysis, Principles and application to petroleum play assessment*. 2nd Edn. Hoboken, NJ, USA: Wiley-Blackwell Publ, 617.

Arora, D., Pant, C., Fareeduddin, S., and Sadiq, M. (2017). Inferring a neoproterozoic orogeny preceding the Rodinia break-up in the Sirohi group, NW India. *Geol. J.* 457, 319–338. doi:10.1144/SP457.8

Ashwal, L. D., Solanki, A. M., Pandit, M. K., Corfu, F., Hendriks, B. W., Burke, K., et al. (2013). Geochronology and geochemistry of the Neoproterozoic Mt, Abu granitoids, NW India: regional correlation and implications for Rodinia paleogeography. *Precambrian Res.* 236, 265–281. doi:10.1016/j.precamres.2013.07.018

Bhardwaj, A., and Biswal, T. K. (2019). "Deformation and tectonic history of Punagarh basin in the trans-aravalli terrane of north-western India," in *Geological evolution of the precambrian Indian shield*. (Cham, Switzerland: Springer), 159–178.

Bhattacharjee, J., Fareeduddinand Jain, S. S. (1993). Tectonic setting, petrochemistry and tungsten metallogeny of Sewariya granite in south Delhi fold belt, Rajasthan. *J. Geol. Soc. India.* 42, 3–16.

Bhattacharjee, J., Golani, P. R., and Reddy, A. R. (1988). Rift related bimodal volcanism and metallogeny in the Delhi Fold Belt, Rajasthan and Gujarat, India. *J. Geol. Soc. India.* 60, 191–199.

Bhowmik, S. K., Bernhardt, H. J., and Dasgupta, S. (2010). Grenvillian age high-pressure upper amphibolite–granulite metamorphism in the Aravalli–Delhi mobile belt, northwestern India: new evidence from monazite chemical age and its implication. *Precambrian Res.* 178, 168–184.

Bhowmik, S. K., Dasgupta, S., Baruah, S., and Kalita, D. (2018). Thermal history of a late mesoproterozoic paired metamorphic belt during Rodinia assembly: new insight from medium-pressure granulites from the Aravalli-Delhi mobile belt, northwestern India. *Geoscience Frontiers.* 9 (2), 335–354.

Bhowmik, S. K., and Dasgupta, S. (2012). Tectonothermal evolution of the banded gneissic Complex in central Rajasthan, NW India: present status and correlation. *J. Asian Earth Sci.* 49, 339–348. doi:10.1016/j.jseaes.2011.07.025

Biswal, T. K., De Waele, B., and Ahuja, H. (2007). Timing and dynamics of the juxtaposition of the Eastern Ghats Mobile Belt against the Bhandara Craton, India: a structural and zircon U–Pb SHRIMP study of the fold–thrust belt and associated nepheline syenite. *Tectonics.* 26, TC4006. doi:10.1029/2006TC002005

Biswal, T. K., Gyani, K. C., Parthasarathy, R., and Pant, D. R. (1998a). Implications of the geochemistry of the pelitic granulites of the Delhi supergroup, Aravalli mountain belt, northwestern India. *Precambrian Res.* 87, 75–85. doi:10.1016/S0301-9268(97)00057-0

Biswal, T. K., Gyani, K. C., Parthasarathy, R., and Pant, D. R. (1998b). Tectonic implication of geochemistry of gabbro-norite-basic granulite suite in the Proterozoic Delhi Supergroup, Rajasthan, India. *J. Geol. Soc. India.* 52, 721–732.

Biswal, T. K. (1988). Polyphase deformation in Delhi rocks, south-east amirgarh, banaskantha district, Gujarat, in precambrian of the Aravalli mountain, Rajasthan, India. *Memoir Geological Society of India.* 7, 267–277.

Black, L. P., Kamo, S. L., Williams, I. S., Mundil, R., Davis, D. W., Korsch, R. J., et al. (2004). Improved 206Pb/238Umicroprobe geochronology by the monitoring of a trace-element-related matrix effect; SHRIMP, ID-TIMS, ELA-ICP-MS and oxygen isotope documentation for a series of zircon standards. *Chem. Geol.* 205, 115–140.

Black, L. P., Kamo, S. L., Williams, I. S., Mundil, R., Davis, D. W., Korsch, R. J., et al. (2003). The application of SHRIMP to Phanerozoic geochronology; a critical appraisal of four zircon standards. *Chem. Geol.* 200 (1–2), 171–188.

Bose, S., Seth, P., and Dasgupta, N. (2017). "Meso-Neoproterozoic mid-crustal metamorphic record from the Ajmer-Srinagar section, Rajasthan, India and its implication to the assembly of the greater Indian Landmass during the Grenvillian-age orogenesis,". *Crustal evolution of India and Antarctica, the supercontinent Connection*. Editors N. C. Pant and S. Dasgupta (London, UK: Geological Society of London), 457, 291–318.2017

Bouchez, J. L., Gleizes, G., Djouadi, T., and Rochette, P. (1990). Microstructure and magnetic susceptibility applied to emplacement kinematics of granites: the example of the Foix pluton (French Pyrenees). *Tectonophysics.* 184 (2), 157–171. doi:10.1080/17445647.2017.1302364

Büttner, S. H. (1999). The geometric evolution of structures in granite during continuous deformation from magmatic to solid-state conditions: an example from the central European Variscan Belt. *Am. Mineral.* 84, 1781–1792.

Cawood, A. (2005). Terra australis orogen. Rodinia breakup and development of the pacific and Iapetus margins of Gondwana during the neoproterozoic and paleozoic. *Earth Sci. Rev.* 69, 249–279. doi:10.1016/j.earscirev.2004.09.001

Cawood, P. A., Mccausland, P. J. A., and Dunning, G. R. (2001). Opening Iapetus: constraints from the laurentian margin in newfoundland. *Geol. Soc. Am. Bull.* 113, 443–453. doi:10.1130/0016-7606(2001)113<0443:OICFTL>2.0.CO;2

Cawood, P. A., Strachan, R. A., Pisarevsky, S. A., and Brendan, J. (2016). Linking collisional and accretionary orogens during Rodinia assembly and breakup: implications for models of supercontinent cycles. *Earth Planet Sci. Lett.* 449, 118–126. doi:10.1016/j.epsl.2016.05.049

Chappell, B. W., and White, A. J. R. (1992). I- and S-type granites in the lachlan fold belt. *Trans. R. Soc. Edinb. Earth Sci.* 83, 1–12.

Chatterjee, S. M., Roy Choudhury, M., Das, S., and Roy, A. (2017). Significance and dynamics of the neoproterozoic (810 Ma) Phulad shear zone, Rajasthan, NW India. *Tectonics.* 36 (8), 1432–1454. doi:10.1002/2017TC004554

Cherniak, D. J., and Pyle, J. M. (2008). Th diffusion in monazite. *Chem. Geol.* 256 (1-2), 52–61. doi:10.1016/j.chemgeo.2008.07.024

Chattopadhyay, N., Mukhopadhyay, D., and Sengupta, P. (2012). Reactivation of basement: example from the Anasagar Granite Gneiss Complex, Rajasthan, western India, in Mazumder, R. & Saha, D. (eds) 2012, Palaeoproterozoic of India. Geological Society, London, Special Publications, 365, 219–245.

Cherniak, D. J., Watson, E. B., Grove, M., and Harrison, T. M. (2004). Pb diffusion in monazite: a combined RBS/SIMS study. *Geochem. Cosmochim. Acta.* 68 (4), 829–840. doi:10.1016/j.gca.2003.07.012

Cherniak, D. J., and Watson, E. B. (2001). Pb Diffusion in zircon. *Chem. Geol.* 172, 5–24.

Choudhary, A. K., Gopalan, K., and Sastry, C. A. (1984). Present status of the geochronology of the Precambrian rocks of Rajasthan. *Tectonophysics.* 105, 131–140. doi:10.1016/0040-1951(84)90199-9

Claoue´-Long, J. (1994). *SHRIMP zircon data*. (Canberra, Australia: Australian Geological Survey), 33.

Collins, A. S., and Pisarevsky, S. A. (2005). Amalgamating eastern Gondwana: the evolution of the circum-Indian orogens. *Earth Sci. Rev.* 71, 229–270.

Collins, A. S., and Windley, B. F. (2002). The tectonic evolution of central and northern Madagascar and its place in the final assembly of Gondwana. *J. Geol.* 110 (3), 325–339. doi:10.1086/339535

Crawford, A. R. (1975). Rb-Sr age determination for the Mount Abu Granite and related rocks of Gujarat. *J. Geol. Soc. India.* 16, 20–28.

Dahl, P. S. (1997). A crystal-chemical basis for Pb retention and fission track annealing systematics in U-bearing minerals with implications for geochronology. *Earth Planet Sci. Lett.* 150, 277–290. doi:10.1016/S0012-821X(97)00108-8

Dasgupta, N., Mukhopadhyay, D., and Bhattacharyya, T. (2012). Analysis of superposed strain: a case study from barr conglomerate in the south Delhi fold belt, Rajasthan, India. *J. Struct. Geol.* 34, 30–42. doi:10.1016/j.jsg.2011.10.010

Dasgupta, S., Bose, S., and Das, K. (2013). Tectonic evolution of the eastern Ghats belt, India. *Precambrian Res.* 227, 247–258. doi:10.1016/j.precamres.2012.04.005

De Wall, H., Pandit, M. K., and Chauhan, N. K. (2012). Paleosol at the archean –proterozoic contact in udaipur. *Precambrian Res.* 216, 120–131. doi:10.1016/j.precamres.2012.06.017

De Wall, H., Pandit, M. K., Sharma, K. K., Schobel, S., and Just, J. (2014). Deformation, granite intrusion in the Sirohi area, SW Rajasthan – constraints on cryogenian to pan- african crustal dynamics of NW India. *Precambrian Res.* 254, 1–18. doi:10.1016/j.precamres.2014.07.025

Deb, M., Thorpe, R. I., Cumming, G. L., and Wagner, A. (1989). Age, source and stratigraphic implication of Pb isotope data for conformable, sediment-hosted, base metal deposits in the proterozoic Aravalli- Delhi orogenic belt, northwestern India. *Precambrian Res.* 43, 1–22. doi:10.1016/0301-9268(89)90002-8

Deb, M., and Thorpe, R. I. (2001). "Geochronological constraints in the precambrian geology of northwestern India and their metallogenic implication," in *Sediment-hosted lead-zinc sulfide deposit in the northwestern Indian ShieldProceedings of an international workshop*. Editors M. Deb and W. D. Goodfellow (Delhi-Udaipur, India, 137–152.

Deb, M., Thorpe, R. I., Krstic, D., Corfu, F., and Davis, D. W. (2001). Zircon U-Pb and galena Pb isotope evidence an approximate 1.0 Ga terrane constituting the western margin of the Aravalli-Delhi orogenic belt, northwestern India. *Precambrian Res.* 108, 195–213.

Deshmukh, T., Prabhakar, N., Bhattacharya, A., and Madhavan, K. (2017). Late paleoproterozoic clockwise P-T history in the mahakoshal belt, central Indian tectonic zone: implications for Columbia supercontinent assembly. *Precambrian Res.* 298, 56–78. doi:10.1016/j.precamres.2017.05.020

Dharma Rao, C. V., Santosh, M., and Kim, S. W. (2012). Cryogenian volcanic arc in the NW Indian Shield: zircon SHRIMP U-Pb geochronology of felsic tuffs and implications for Gondwana assembly. *Gondwana Res.* 22, 36–53. doi:10.1016/j.gr.2011.10.014

Dharma Rao, C. V., Santosh, M., Kim, S. W., and Li, S. (2013). Arc magmatism in the Delhi Fold Belt. SHRIMP U–Pb zircon ages of granitoids and implications for Neoproterozoic convergent margin tectonics in NW India. *J. Asian Earth Sci.* 78, 83–99. doi:10.1016/j.jseaes.2012.09.007

Eby, G. N. (1992). Chemical subdivision of the A-type granitoids; petrogenetic and tectonic implications. *Geology.* 20, 641–644. doi:10.1130/0091-7613(1992)020<0641:CSOTAT>2.3.CO;2

Fareeduddin, M., Basavalingu, B., and Janardhan, A. (1994). PT conditions of pelitic granulites and associated charnockites of Chinwali area, west of Delhi fold belt, Rajasthan. *J. Geol. Soc. India.* 43 (2), 169–178.

Fiannacca, P., Williams, I. S., Cirrincione, R., and Pezzino, A. (2019). Poly-orogenic melting of metasedimentary crust from a granite geochemistry and inherited zircon perspective (southern calabria-peloritani orogen. Italy). *Front. Earth Sci.* 7, 1–15. doi:10.3389/feart.2019.00119

Fitzsimons, I. C. W. (2000). A review of tectonic events in the East Antarctic Shield and their implications for Gondwana and earlier Supercontinents. *J. Afr. Earth Sci.* 31, 3–23. doi:10.1016/S0899-5362(00)00069-5

Fortes de Lena, L. O., Pimentel, M. M., Philipp, R. P., Armstrong, R., and Sato, K. (2014). The evolution of the Neoproterozoic São Gabriel juvenile terrane, southern Brazil based on high spatial resolution U-Pb ages and d18O data from detrital zircons. *Precambrian Res.* 247, 126–138.

Foster, G., Parrish, R. R., Horstwood, M. S. A., Cheney, S., Pyle, J., and Gibson, H. D. (2004). The generation of prograde P–T-t points and paths; a textural, compositional, and chronological study of metamorphic monazite. *Earth Planet Sci. Lett.* 228, 125–142.

Fritz, H., Abdelsalam, M., Ali, K. A., Bingen, B., Collins, A. S., Fowler, A. R., et al. 2013). Orogen styles in the east african orogen: a review of the neoproterozoic to cambrian tectonic evolution. *J. Afr. Earth Sci.* 86, 65–106. doi:10.1016/j.jafrearsci.2013.06.004

Frost, B. R., Barnes, C. G., Collins, W. J., Arculus, R. J., Ellis, D. J., and Frost, C. D. (2001). A geochemical classification for granitic rocks. *J. Petrol.* 42, 2033–2048. doi:10.1093/petrology/42.11.2033

Ganade, C. E., Cordani, U. G., Agbossoumounde, Y., Caby, R., Basei, M. A. S., Weinberg, R. F., et al. (2016). Tightening-up NE Brazil and NW Africa connections: new U-Pb/Lu-Hf zircon data of a complete plate tectonic cycle in the Dahomey belt of the West Gondwana Orogen in Togo and Benin. *Precambrian Res.* 276, 24–42. doi:10.1016/j.precamres.2016.01.032

Ganade de Araujo, C. E., Cordani, U. G., Weinberg, R. F., Basei, M. A. S., Armstrong, R., and Sato, K. (2014). Tracing Neoproterozoic subduction in the Borborema Province (NE-Brazil): clues from U-Pb geochronology and Sr-Nd-Hf-O isotopes on granitoids and migmatites. *Lithos.* 202-203, 167–189. doi:10.1016/j.lithos.2014.05.015

Gangopadhyay, A., and Mukhopadhyay, D. (1984). "Structural geometry of the Delhi Supergroup near Sendra," in *Recent researches in Geology*. Editor A. K. Saha (India: Geological Evolution of Peninsular). 45–60.

Ghosh, S. K., Hazra, S., and Sengupta, S. (1999). Planar, non-planar and refolded sheath folds in the Phulad Shear Zone, Rajasthan, India. *J. Struct. Geol.* 21 (12), 1715–1729.

Ghosh, S. K., Sen, G., and Sengupta, S. (2003). Rotation of long tectonic clasts in transpressional shear zones. *J. Struct. Geol.* 25 (7), 1083–1096. doi:10.1016/S0191-8141(02)00146-3

Ghosh, S. K. (1988). Theory of chocolate tablet boudinage. *J. Struct. Geol.* 10, 541–553. doi:10.1016/0191-8141(88)90022-3

Gonçalves, G. O., Lana, C., Scholz, R., Buick, I. S., Gerdes, A., Kamo, S. L., et al. (2016). An assessment of monazite from the Itambé pegmatite district for use as U-Pb isotope reference material for microanalysis and implications for the origin of the "Moacyr" monazite. *Chem. Geol.* 424, 30–50 doi:10.1016/j.chemgeo.2015.12.019

Gopalan, K., Trivedi, J. R., Merh, S. S., Patel, P. P., and Patel, S. G. (1979). Rb-Sr age of Godhra and related granites, Gujarat, India. *Proc. Indiana Acad. Sci.* 88, 7–17.

Goscombe, B. D., Passchier, C. W., and Hand, M. (2004). Boudinage classification: end-member boudin types and modified boudin structures. *J. Struct. Geol.* 26, 739–763. doi:10.1016/j.jsg.2003.08.015

Grebennikov, A. V. (2014). A-type granites and related rocks: petrogenesis and classification. *Russ. Geol. Geophys.* 55, 1074–1086. doi:10.1016/j.rgg.2014.10.011

Gupta, P., Guha, D. B., and Chattopadhyay, B. (1998). Basement –cover relationship in the Khetri copper belt and the emplacement mechanism of the granite massif, Rajasthan, India. *J. Geol. Soc. India.* 52, 417–432.

Gupta, S. N., Arora, Y. K., Mathur, R. K., Iqbaluddin, B. P., Prasad, B., Sahai, T. N., et al. (1997). The Precambrian geology of the Aravalli region, southern Rajasthan and northeastern Gujarat.*Memoir Geological Survey of India.* 123, 262

Hahn, G., Kodl, G., de Wall, H., Schulz, B., Bestmann, M., and Chauhan, N. K. (2020). "Deformation in the Aravalli supergourp, Aravalli-Delhi mobile belt, NW India and tectonic significance," in *Structural geometry of mobile belts of Indian subcontinent*. Editor T. K. Biswalal. (Berlin, Germany; Springer), 23–55. doi:10.1007/978-3-030-40593-9_2

Hawkesworth, C. J., Cawood, P. A., Dhuime, B., and Kemp, T. I. S. (2017). ""Earth's continental lithosphere through time," in *Annual review of earth and planetary Sciences*. Editors R. Jeanloz and K. H. Freeman (Palo Alto, CA: Annual Reviews), 45, 169–198. doi:10.1146/annurev-earth-063016-020525

Heron, A. M. (1953). The geology of central Rajputana. *Mem. Geol. Surv. India*. 79, 389. doi:10.1016/0301-9268(77)90044-4

Jercinovic, M. J., and Williams, M. L. (2005). Analytical perils (and progress) in electron microprobe trace element analysis applied to geochronology: background acquisition interferences, and beam irradiation effects. *Am. Mineral.* 90 (4), 526–546. doi:10.2138/am.2005.1422

Jercinovic, M. J., Williams, M. L., and Lane, E. D. (2008). *In-situ* trace element analysis of monazite and other fine-grained accessory minerals by EPMA. *Chem. Geol.* 254 (3-4), 197–215. doi:10.1016/j.chemgeo.2008.05.016

Johansson, A. (2014). From Rodinia to Gondwana with the 'SAMBA' model—a distant view from Baltica towards amazonia and beyond. *Precambrian Res.* 244, 226–235. doi:10.1016/j.precamres.2013.10.012

Just, J., Schulz, B., de Wall, H., Jourdan, F., and Pandit, M. K. (2011). Monazite CHIME/EPMA dating of Erinpura granitoid deformation: implications for Neoproterozoic tectono-thermal evolution of NW India. *Gondwana Res.* 19, 402–412. doi:10.1016/j.gr.2010.08.002

Kaur, P., Chaudhri, N., Okrusch, M., and Koepke, J. (2006). Palaeoproterozoic A-type felsic magmatism in the Khetri Copper Belt, Rajasthan, northwestern India: petrologic and tectonic implications. *Mineral. Petrol.* 87 (1-2), 81–122.

Kaur, P., Zeh, A., Chaudhri, N., Gerdes, A., and Okrusch, M. (2013). Nature of magmatism and sedimentation at a Columbia active margin: insights from combined U–Pb and Lu–Hf isotope data of detrital zircons from NW India. *Gondwana Res.* 23, 1040–1052. doi:10.1016/j.gr.2012.07.008

Kaur, P., Zeh, A., and Chaudhri, N. (2019). Archean crustal evolution of the Aravalli Banded Gneissic Complex, NW India: constraints from zircon U-Pb ages, Lu-Hf isotope systematics, and whole-rock geochemistry of granitoids. *Precambrian Res.* 327, 81–102. doi:10.1016/j.precamres.2019.03.004

Kaur, P., Zeh, A., Chaudhri, N., and Tiwana, J. K. (2020). First evidence of late paleoproterozoic/early mesoproterozoic sediment deposition and magmatism in the central Aravalli orogen (NW India). *J. Geol.* 128. doi:10.1086/707235

Kearey, P., Klepeis, K. A., and Vine Frederick, J. (2009). *Global tectonics*. 3rd ed., (Hoboken, NJ, USA: Wiley-Blackwell). Available at: https://en.wikipedia.org/wiki/International_Standard_Book_Number"ISBN

Khan, M. S., Smith, T. E., Raza, M., and Huang, J. (2005). Geology, geochemistry and tectonic significance of mafic–ultramafic rocks of mesoproterozic Phulad ophiolite suite of South Delhi fold belt, NW Indian shield. *Gondwana Res.* 8, 553–566. doi:10.1016/S1342-937X(05)71155-2

Kröner, A., and Stern, R. J. (2005). "Pan-African orogeny," in *Encyclopedia of Geology*. Editors R. C. Selley, L. R. M. Cooks, and I. R. Plimer (Amsterdam, Netherland: Elsevier), 1, 1–12.

Kruhl, J. H. (1996). Prism-and basal-plane parallel subgrain boundaries in quartz: a microstructural geothermobarometer. *J. Metamorph. Geol.* 14 (5), 581–589. doi:10.1046/j.1525-1314.1996.00413.x

Kumar, A., Prakash, A., Saha, L., Corfu, F., and Bhattacharya, A. (2019). 940 Ma anatexis in 1726 Ma orthogneiss in the northern margin of the Bhilwara belt and significance for the precambrian evolution in northwest India. *J. Geol.* 127, 6.

Kusznir, N. J., Karner, G. D., and Egan, S. (1987). "Geometric, thermal and isostatic consequences of detachments in continental lithosphere extension and basin formation,". *Sedimentary basins and basin forming mechanism.* Editors C. Beaumont and A. I. Tankard (Calgary, Alberta: Canadian Society of Petroleum Geologists Memoires), 12, 185–203.

Lehmann, J., Saalmann, K., Naydenov, K. V., Milani, L., Belyanin, G. A., Zwingmann, H., et al. (2016). Structural and geochronological constraints on the Pan-African tectonic evolution of the northern Damara Belt, Namibia. *Tectonics.* 35, 103–135.

Li, Z. X., Bogdanova, S. V., Collins, A. S., Davidson, A., De Waele, B., Ernst, R. E., et al. (2008). Assembly, configuration, and break-up history of Rodinia: a synthesis. *Precambrian Research.* 160, 179–210.

Lister, G. S., Etheridge, M. A., and Symonds, P. A. (1991). Detachment model for the Formation of passive continent margins. *Tectonics.* 10 (5), 1038–1064.

Liu, F., and Han, D. (2019). *Petrogenetic and tectonic implications of Triassic granitoids in the Chinese Altay: the Alaer granite example*. (Amsterdam, Netherlands: Elseviers). doi:10.1016/j.heliyon

Ludwig, K. R. (2012). *Isoplot 4.15. A geochronological toolkit for microsoft excel. (Special publication No. 5)*. (Berkeley, CA, USA: Berkeley Geochronology Center)

Mahan, K. H., Goncalves, P., Williams, M. L., and Jercinovic, M. J. (2006). Dating metamorphic reactions and fluid flow: application to exhumation of high-P granulites in a crustal-scale shear zone, western Canadian Shield. *J. Metamorph. Geol.* 24, 193–217. doi:10.1111/j.1525-1314.2006.00633.x

McKenzie, D. P. (1978). Some remarks on the development of sedimentary basins. *Earth Planet Sci. Lett.* 40, 25–32. doi:10.1016/0012-821X(78)90071-7

McMenamin, M. A. S., and McMenamin, D. L. S. (1990). *The emergence of animals: the cambrian breakthrough*, (New York, NY, USA: Columbia University Press), 217.

Meert, J. G. (2003). A synopsis of events related to the assembly of eastern Gondwana. *Tectonophysics.* 362 (1-4), 1–40. doi:10.1016/S0040-1951(02)00629-7

Meert, J. G., and Lieberman, B. S. (2008). The neoproterozoic assembly of gondwanaland its relationship to the ediacaran–cambrian radiation. *Gondwana Res.* 14, 5–21.

Meert, J. G., Pandit, M. K., and Kamenov, G. D. (2013). Further geochronological and paleomagnetic constraints on Malani (and pre-Malani) magmatism in NW India. *Tectonophysics.* 608, 1254–1267. doi:10.1016/j.tecto.2013.06.019

Meert, J. G., and Santosh, M. (2017). The Columbia supercontinent revisited. *Gondwana Res.* 50, 67–83. doi:10.1016/j.gr.2017.04.011

Meert, J. G., and Torsvik, T. H. (2003). The making and unmaking of a supercontinent: Rodinia revisited. *Tectonophysics.* 375, 261–288. doi:10.1016/S0040-1951(03)00342-1

Mehdi, M., Kumar, S., and Pant, N. C. (2015). Low grade metamorphism in the lalsot-bayana sub-basin of the north Delhi fold belt and its tectonic implication. *J. Geol. Soc. India.* 85 (4), 397–410.

Merlet, C. (1992). Quantitative electron probe microanalysis: new accurate Φ(pz) description. *Mikrochim. Acta.* 12, 107–115 doi:10.1007/978-3-7091-6679-6_8

Miller, R. B., and Paterson, S. R. (1994). The transition from magmatic to high-temperature solid-state deformation: implications from the Mount Stuart batholith, Washington. *J. Struct. Geol.* 16 (6), 853–865. doi:10.1016/0191-8141(94)90150-3

Misra, A., Chauhan, A., and Chatterjee, D. (2020). Petrology, geochemistry and geochronology of neoarchean A-type granite from alwar basin, north Delhi terrane, NW India. *J. Earth Syst. Sci.* 129 (88), 1–34. doi:10.1007/s12040-020-1349-5

Montadert, L., Roberts, D. G., de Charpal, O., and Guennoc, P. (1979). Rifting and subsidence of northern continental margin of the Bay of Biscay. *Deep Sea Drill. Proj.* 48, 1025–1060.

Montel, J. M., Foret, S., Veschambre, M., Nicollet, C., and Provost, A. (1996). Electron microprobe dating of monazite. *Chem. Geol.* 131 (1-4), 37–53. doi:10.1016/0009-2541(96)00024-1

Mukhopadhyay, D., and Matin, A. (1991). Early major folds in the Delhi Supergroup around Hatankhera, Ajmer district, Rajasthan. *Indian J. Geol.* 63, 67–74.

Mukhopadhyay, D. (1989). Structural history of the central section of the Delhi orogenic belt" in Proceedings of 28th International Geological Congress, Wahington, DC, July, 1989, 479–480.

Murao, S., Deb, M., Takagi, T., Seki, Y., Pringle, M., and Naito, K. (2000). "Geochemical and geochronological constraints for tin- poly- metallic mineralization in Tosham area, Haryana, India," in *Crustal evolution and metallogeny in the northwestern Indian shield*. Editor M. Deb (New Delhi, India: Narosa Publishing House), 430–442.

Murphy, J. B., and Nance, R. D. (2013). Speculations on the mechanisms for the formation and breakup of supercontinents. *Geoscience Frontiers.* 4, 185–194. doi:10.1016/j.gsf.2012.07.005

Naha, K., Mitra, S. K., and Biswal, T. K. (1987). Structural history of the rocks of the Delhi group around todgarh, central Rajasthan. *Indian J. Geol.* 59, 126–156.

Naha, K., Mukhopadhyay, D. K., Mohanty, R., Mitra, S. K., and Biswal, T. K. (1984). Significance of contrast in the early stages of the structural history of the Delhi and the Pre-Delhi rock groups in the Proterozoic of Rajasthan, western India. *Tectonophysics.* 105, 193–206. doi:10.1016/0040-1951(84)90203-8

Naylor, M., and Sinclair, H. D. (2008). Pro- vs. retro-foreland basins. *Basin Res.* 20, 3. doi:10.1111/j.1365-2117.2008.00366.x

Oriolo, S., Oyhantçabal, P., Wemmer, K., and Siegesmund, S. (2017). Contemporaneous assembly of Western Gondwana and final Rodinia break-up: implications for the supercontinent cycle. *Geosci. Front.* 8 (6), 1431–1445. doi:10.1016/j.gsf.2017.01.009

Ozha, M. K., Mishra, B., Hazarika, P., Jeyagopal, A. V., and Yadav, G. S. (2016). EPMA monazite geochronology of the basement and supracrustal rocks within the Pur-Banera basin, Rajasthan: evidence of Columbia breakup in Northwestern India. *J. Asian Earth Sci.* 117, 284–303. doi:10.1016/j.jseaes.2015.12.016

Pandey, M., Pant, N. C., and Santosh, K. (2013). Criteria to distinguish between regional and contact zone monazite. A case study from Proterozoic North Delhi Fold Belt (NDFB), India. *Episodes.* 36, 275–289.

Pandit, M. K., Carter, L. M., Ashwal, L. D., Tucker, R. D., Torsvik, T. H., Jamtveit, B., et al. (2003). Age, petrogenesis and significance of 1 Ga granitoids and related rocks from the Sendra area, Aravalli Craton, NW India. *J. Asian Earth Sci.* 22 (4), 363–381. doi:10.1016/S1367-9120(03)00070-1

Pandit, M. K., de Wall, H., and Chauhan, N. K. (2008). Paleosol at the Archean-Proterozoic contact in NW India revisited: evidence for oxidizing conditions during paleoweathering?. *J. Earth Syst. Sci.* 117, 201–209.

Pant, N. C., Kundu, A., and Joshi, S. (2008). Age of metamorphism of Delhi Supergroup rocks-electron microprobe ages from Mahendragarh district, Haryana. *J. Geol. Soc. India.* 72 (3), 365–372.

Pant, N. C., Kundu, A., Joshi, S., Dey, A., Bhandari, A., and Joshi, A. (2009). Chemical dating of monazite: testing of an analytical protocol against independently dated standards. *Indian Journal of Geosciences.* 63, 311–318.

Passchier, C. W., and Trouw, R. A. (2005). *Microtectonics*. Berlin, Germany: Springer Science and Business Media.

Paterson, S. R., Fowler, T. K., Schmidt, K. L., Yoshinobu, A. S., Yuan, E. S., and Miller, R. B. (1998). Interpreting magmatic fabric patterns in plutons. *Lithos.* 44, 53–82. doi:10.1016/S0024-4937(98)00022-X

Pearce, J. A. (1996). Sources and settings of granitic rocks. *Episodes.* 19, 120–125. doi:10.18814/epiiugs/1996/v19i4/005

Pidgeon, R. T., Furfaro, D., Kennedy, A. K., Nemchin, A. A., and Van Bronswijk, W. (1994). Calibration of zircon standards for the Curtin SHRIMP II, US. *Geol. Surv. Circular.* 1107, 251. doi:10.13140/RG.2.2.27418.08646

Pisarevsky, S. A., Biswal, T. K., Wang, X.-C., De Waele, B., Ernst, R., Söderlund, U., et al. (2013). Palaeomagnetic, geochronological and geochemical study of mesoproterozoic lakhna dykes in the bastar craton, India: implications for the mesoproterozoic supercontinent. *Lithos.* 174, 125–143. doi:10.1016/j.lithos.2012.07.015

Pisarevsky, S. A., Elming, Sten-Åke., Pesonen, L. J., and Li, Zheng-Xiang. (2014). Mesoproterozoic paleogeography: supercontinent and beyond. *Precambrian Res.* 244, 207–225.

Powell, C. M A., and Pisarevsky, S. A. (2002). Late neoproterozoic assembly of east gondwanaland. *Geology.* 30, 3–6. doi:10.1130/0091-7613(2002)030<0003:LNAOEG>2.0.CO;2

Prabhakar, N. (2013). Resolving poly-metamorphic Paleoarchean ages by chemical dating of monazites using multi-spectrometer U, Th, and Pb analyses and sub-counting methodology. *Chem. Geol.* 347, 255–270. doi:10.1016/j.chemgeo.2013.04.012

Pradhan, V. R., Meert, J. G., Pandit, M. K., Kamenov, G., Gregory, L. C., and Malone, S. (2009). India's changing place in global Proterozoic reconstructions: a review of geochronologic constraints and paleomagnetic poles from the Dharwar, Bundelkhand and Marwar cratons. *J. Geodyn.* 50, 224–242.

Pryer, L. L. (1993). Microstructures in feldspars from a major crustal thrust zone: the Grenville Front, Ontario, Canada. *J. Struct. Geol.* 15 (1), 21–36. doi:10.1016/0191-8141(93)90076-M

Purohit, R., Papineau, D., Kröner, A., Sharma, K. K., and Roy, A. B. (2012). Carbon isotope geochemistry and geochronological constraints of the Neoproterozoic Sirohi Group from northwest India. *Precambrian Res.* 220, 80–90. doi:10.1016/j.precamres.2012.07.012

Pyle, J. M., Spear, F. S., and Ramsay, J. G. (2003). "Four generations of accessory-phase growth in low pressure migmatites from SW New Hampshire. American Mineralogist," in *1967. Folding and fracturing of rocks.* (New York, NY, USA: McGraw-Hill Companies), 88, 338–351.

Ramsay, J. G. (1967). *Folding and fracturing of rocks*. McGraw-Hill Companies, p. 568

Ramsay, J. G., and Huber, M. I. (1987). *The techniques of modern structural geologyFolds and fractures*. London, UK: Academic Press.

Ray, S., Joshi, B. K., Sundarraman, S., Joshi, D., and Ahmad, T. (2015). Geochemical and petrogenetic study of proterozoic Sewariya and Govindgarh granitoids from south Delhi fold belt. *Curr. Sci.* 109 (8), 1458–1465. doi:10.18520/v109/i8/1458-1465

Ray, S. K. (1974). Structural history of the Saladipura purite-pyrrohotite deposit and associated rock, Khetri Copper Belt, Rajasthan. *J. Geol. Soc. India.* 15, 227–238.

Raza, M., and Siddiqui, M. Z. (2012). Geochemistry and tectonic significance of mafic volcanic rocks of the Hindoli belt, southeastern Rajasthan: implications for continent assembly. *J. Geol. Soc. India.* 80 (4), 553–562. doi:10.1007/s12594-012-0176-y

Rino, S., Kon, Y., Sato, W., Maruyama, S., Santosh, M., and Zhao, D. (2008). The Grenvillian and Pan-African orogens: world's largest orogenies through geologic time, and their implications on the origin of superplume. *Gondwana Res.* 14, 51–72. doi:10.1016/j.gr.2008.01.001

Rogers, J. J., and Santosh, M. (2002). Configuration of Columbia, a mesoproterozoic supercontinent. *Gondwana Res.* 5 (1), 5–22. doi:10.1016/S1342-937X(05)70883-2

Rosenberg, C. L., and Stünitz, H. (2003). Deformation and recrystallization of plagioclase along a temperature gradient: an example from the Bergell tonalite. *J. Struct. Geol.* 25 (3), 389–408. doi:10.1016/S0191-8141(02)00036-6

Roy, A. B., Kröner, A., Laul, V., and Purohit, R. (2005). "Single zircon dating of hypersthene bearing granitoid from Balaram-Abu Road area, southern part of the Aravalli Mountains. NW India—implication for Malani Magmatism related thermal event," in *Metamorphism and crustal evolution*. Editor H. Thomas (New Delhi, India: Atlantic Publishers and Distributors), 339–346.

Roy, A. B. (2001). Neoproterozoic crustal evolution of northwestern Indian shield: implications on break-up and assembly of supercontinents. *Gondwana Res.* 4, 289–306. doi:10.1016/S1342-937X(05)70330-0

Roy, A. B., and Sharma, K. K. (1999). Geology of the region around Sirohi town, western Rajasthan–story of Neoproterozoic evolution of the Trans-Aravalli crust. *Geological Evolution of Western Rajasthan*, 19–33.

Ruj, T., and Dasgupta, N. (2014). Tectonic imprints within a granite exposed near Srinagar, Rajasthan, India. *Journal of earth system science.* 123 (6), 1361–1374.

Sambridge, M. S., and Compston, W. (1994). Mixture modeling of multi-component data sets with application to ion-probe zircon ages. *Earth Planet Sci. Lett.* 128 (3-4), 373–390. doi:10.1016/0012-821X(94)90157-0

Sarkar, G., Bishui, P. K., Chattopadhyay, B., Chowdhury, S., Chowdhury, I., Saha, K. C., et al. (1992). Geochronology of granites and felsic volcanic rocks of Delhi Fold Belt. *GSI.* 125 (2), 21–23.

Satyavani, N., Dixit, M. M., and Reddy, P. R. (2004). Crustal structure of Delhi fold belt, India, from seismic reflection data. *Curr. Sci.* 86 (7), 991–999.

Schobel, S., Sharma, K. K., Horbrand, T., Bohm, T., Donhauser, I., de Wall, et al. (2017). continental rift-setting and evolution of neoproterozoic Sindreth basin in NW-India. *J. Earth Syst. Sci.* 90, 126. doi:10.1007/s12040-017-0855-6

Sharma, K. K. (2005). Malani magmatism: an extensional lithospheric tectonic origin. *GSA (Geol. Soc. Am.) Spec. Pap. (Reg. Stud.).* 388, 463–476.

Singh, S., Shukla, A., Umasankar, B. H., and Biswal, T. K. (2020). "Timing of South Delhi orogeny: interpretation from structural fabric and granite Geochronology, beawar-rupnagar- Babra area, Rajasthan, NW India," in *Society of Earth Scientists Series, Structural Geometry of Mobile Belts of the Indian Subcontinent.* Editors T. K. Biswal, et al. (Switzerland: Springer Nature AG). doi:10.1007/978-3-030-40593-9_1

Singh, Y. K., De Waele, B., Karmarkar, S., Sarkar, S., and Biswal, T. K. (2010a). Tectonic setting of the balaram–kui–surpagla–kengora granulites of the south Delhi terrane of the Aravalli mobile belt, NW India and its implication on

correlation with the east african orogen in the Gondwana assembly. *Precambrian Res.* 183, 669–688. doi:10.1016/j.precamres.2010.08.005

Sinha-Roy, S. (1988). "Proterozoic wilson cycles in Rajasthan," in *Precambrian of the Aravalli mountain, Rajasthan, India*. Editor A. B. Roy (Bengaluru, India: Geological Society of India, Memoirs), 7, 95–108.

Sivasubramaniam, R., Anand, S. V., Pandian, M. S., and Balakrishnan, S. (2019). Geological, geochemical and Rb–Sr isotopic studies on tungsten mineralised Sewariya–Govindgarh granites of Delhi Fold Belt, Rajasthan, NW India. *J. Earth Syst. Sci.* 128 (1), 19. doi:10.1007/s12040-018-1034-0

Spear, F. S., and Wark, D. A. (2009). Cathodoluminescence imaging and titanium thermometry in metamorphic quartz. *J. Metamorph. Geol.* 27 (3), 187–205. doi:10.1111/j.1525-1314.2009.00813.x

Stacey, J. T., and Kramers, J. D. (1975). Approximation of terrestrial lead isotope evolution by a two-stage model. *Earth Planet Sci. Lett.* 26 (2), 207–221. doi:10.1016/0012-821X(75)90088-6

Stern, R. A. (2001). *A new isotopic and trace-element standard for the ion microprobe: preliminary thermal ionization mass spectrometry (TIMS) U-Pb and electron-microprobe data*. Canada: Ressources naturelles Canada, 11.

Stern, R. J. (1994). Arc assembly and continental collision in the neoproterozoic East African orogen. Implications for the consolidation of gondwanaland. *Annu. Rev. Earth Planet Sci.* 22, 319–351. doi:10.1146/annurev.ea.22.050194.001535

Stipp, M., Stunitz, H., Heilbronner, R., and Schmid, S. M. (2002). The eastern Tonale fault zone: a 728 'natural laboratory' for crystal plastic deformation of quartz over a temperature range from 729 250 to 700oC. *J. Struct. Geol.* 24, 1861–1884.

Sugden, T. J., Deb, M., and Windley, B. F. (1990). "The tectonic setting of mineralization in the Proterozoic Aravalli-Delhi orogenic belt, NW India," in *Precambrian continental crust and its economic resources*. Editor S. M. Naqvi (New York, NY, USA: Elsevier), 367–390.

Suzuki, K., and Dunkley, D. J. (2014). Uranium-lead, chemical isochron U-Pb method (CHIME). *Encyclopedia of Scientific Dating Methods*. Dordrecht: Springer Science+Business Media, 1–10. doi:10.1007/978-94-007-6326-5_200-1

Synchanthavong, S. P., and Desai, S. D. (1977). Protoplate tectonics controlling the Precambrian deformation and metallogenic epochs in NW India. *Miner. Sci. Eng.* 1, 218–236.

Tiwana, J. K., Kaur, P., Chaudhri, N., and Manisha (2019). First record of circa 970 Ma post-collisional A-type magmatism in the Sendra Granitoid Suite, central Aravalli orogen, northwest India. *Curr. Sci.*, 801–808. doi:10.18520/cs/v118/i5/801-808

Tiwari, S. K., Beniest, A., and Biswal, T. K. (2020). Variation in vorticity of flow during exhumation of lower crustal rocks (Neoproterozoic Ambaji granulite, NW India). *J. Struct. Geol.* 130, 103912. doi:10.1016/j.jsg.2019.103912

Tiwari, S. K., and Biswal, T. K. (2019a). Dynamics, EPMA Th-U-total Pb monazite geochronology and tectonic implications of deformational fabric in the lower-middle crustal rocks, a case study of Ambaji granulite, NW India. *Tectonics.* 38 (7), 2232–2254. doi:10.1029/2017TC004891

Tiwari, S. K., and Biswal, T. K. (2019b). Paleostress and magma pressure measurement of granite veins in the Neoproterozoic Ambaji granulite, South Delhi terrane, Aravalli–Delhi mobile belt, NW India: implication towards extension driven exhumation of middle-lower crustal rocks. *J. Earth Syst. Sci.* 128 (150), 1–13. doi:10.1007/s12040-019-1187-5

Tobisch, O. T., Collerson, K. D., Bhattacharya, T., and Mukhopadhyay, D. (1994). Structural relationship and Sm-Nd isotope systematics of polymetamorphic granitic gneisses and granitic rocks from central Rajasthan, India-Implications for the evolution of the Aravalli craton. *Precambrian Res.* 65, 319–339. doi:10.1016/0301-9268(94)90111-2

Twiss, R. J., and Moores, E. M. (1992). "Plate tectonic models of orogenic core zones," in *Structural Geology*. 2nd ed. (New York, NY: Macmillan), 493.

USGS Reference standards (2005). Available at: http://minerva.union.edu/hollochk/icp-ms/rock_ standards. html (Accessed March 12, 2020).

Valentine, J. W., and Moores, E. M. (1970). Plate-tectonic regulation of faunal diversity and sea level: a model. *Nature*, 228, 657–659. doi:10.1038/228657a0

Van Lente, B., Ashwal, L. D., Pandit, M. K., Bowring, S. A., and Torsvik, T. H. (2009). Neoproterozoic hydrothermally altered basaltic rocks from Rajasthan, northwest India: implications for late Precambrian tectonic evolution of the Aravalli Craton. *Precambrian Res.* 170 (3-4), 202–222. doi:10.1016/j.precamres.2009.01.007

Verma, K., and Greiling, R. O. (1995). Tectonic evolution of the Aravalli orogen (NW India): an inverted proterozoic rift basin?. *Geol. Rundsch.* 84, 683–686.

Vernon, R. H., Paterson, S. R., and Geary, E. E. (1989). Evidence for syntectonic intrusion of plutons in the Bear Mountains fault zone, California. *Geology.* 17, 723–726. doi:10.1130/0091-7613(1989)017<0723:EFSIOP>2.3.CO;2

Volpe, A. M., and Macdougall, J. D. (1990). Geochemistry and isotopic characteristics of mafic (Phulad ophiolite) and related rocks in the Delhi supergroup, Rajasthan, India: implications for rifting in the Proterozoic. *Precambrian Res.* 48, 167–191. doi:10.1016/0301-9268(90)90061-T

Wang, W., Cawood, P. A., Pandit, M. K., Zhou, M., and Chen, W. (2014). Zircon U–Pb age and Hf isotope evidence for an Eoarchaean crustal remnant and episodic crustal reworking in response to supercontinent cycles in NW India. *J. Geol. Soc.* 174 (4), 759–772. doi:10.1144/jgs2016-080,174,759–772

Watson, E. B., and Harrison, T. M. (1983). Zircon saturation revisited: temperature and composition effects in a variety of crustal magma types. *Earth Planet Sci. Lett.* 64, 295–304. doi:10.1016/0012-821X(83)90211-X

Wawrzenitz, N., Krohe, A., Rhede, D., and Romer, R. L. (2012). Dating rock deformation with monazite: the impact of dissolution precipitation creep. *Lithos.* 134, 52–74. doi:10.1016/j.lithos.2011.11.025

Wernicke, B. (1985). Uniform normal-sense simple shear of the continental lithosphere. *Can. J. Earth Sci.* 22, 108–125.

Williams, M. L., Jercinovic, M. J., Goncalves, P., and Mahan, K. (2006). Format and philosophy for collecting, compiling, and reporting microprobe monazite ages. *Chem. Geol.* 225, 1–15. doi:10.1016/j.chemgeo.2005.07.024

Williams, M. L., and Jercinovic, M. J. (2002). Microprobe monazite geochronology; putting absolute time into microstructural analysis. *J. Struct. Geol.* 24, 1013–1028. doi:10.1016/S0191-8141(01)00088-8

Zhang, W. X., Zhu, L. Q., Wang, H., and Wu, Y. B. (2018). Generation of post-collisional normal calc-alkaline and adakitic granites in the Tongbai orogen, central China. *Lithos.* 296–299, 513–531. doi:10.1016/j.lithos.2017.11.033

Zhao, G., Cawood, P. A., Wilde, S. A., and Sun, M. (2002). Review of global 2.1–1.8 Ga orogens: implications for a pre-Rodinia supercontinent. *Earth Sci. Rev.* 59, 125–162. doi:10.1016/S0012-8252(02)00073-9

Zhao, J. H., Pandit, M. K., Wang, W., and Xia, X. P. (2018). Neoproterozoic tectonothermal evolution of NW India: evidence from geochemistry and geochronology of granitoids. *Lithos.* 316–317, 330–346. doi:10.1016/j.lithos.2018.07.020

Conflict of Interest: Author BDW was employed by the company SRK Consulting (Australasia) Pvt Ltd.

The remaining authors declare that the research was conducted in the absence of any commercial or financial relationships that could be construed as a potential conflict of interest.

APPENDIX

Textural interpretation of zircon:

Sample TKB-1. Zircons from this sample range in size from 50 to 150 μm and have length to width ratios of 1:1 to 3:1. The zircon crystals are subangular in shape. CL image reveals oscillatory zoning patterns, consistent with magmatic zircon (**Figure 6**). A small number of zircons have small homogenous overgrowths, but none were large enough to allow measuring on the instrument. Seventeen analyses were conducted on seventeen separate grains and indicate low levels of f_{206} (proportion of nonradiogenic ^{206}Pb in total ^{206}Pb), between 0 and 2.02 (**Table 3**). Uranium and Thorium values are in the ranges 118–434 and 55–470 ppm, respectively, resulting in Th/U ratios between 0.24 and 1.69, typical for magmatic zircon.

Sample TKB-2. Zircons from this sample range in size from 50 to 150 μm and have length to width ratios of 1:1 to 2:1. The zircon grains are dominantly subangular to subrounded. CL image reveals oscillatory zoning patterns, consistent with magmatic zircon (CL **Figure 6**). Some zircons show an inner medium-CL domain of oscillatory zoning, overgrown by an outer higher-CL domain, also oscillatory zoned. The internal zoning patterns in the zircon are consistent with growth from magmatic fluids. A small number of zircons have small homogenous dark-CL overgrowths, possibly related to metamorphic overgrowth, but none were large enough to allow measurement. Thirty analyses were conducted on thirty grains, all on oscillatory zoned domains. One analysis resulted in extremely high U and Th counts and plots inversely discordant (TKB-2–20, **Table 3**). The 29 remaining analyses yielded f_{206} values between 0 and 9.51%, with U and Th in the ranges 115–483 and 101–681 ppm, respectively. Th/U ratios are in the range 0.79–1.73, consistent with magmatic zircon.

Sample TKB-3. Zircons from sample TKB-3 range in size from 50 to 150 μm and have length to width ratios of 1:1 to 3:1. The zircon grains are subangular in shape, with some subrounded zircon. CL image reveals relatively low response, with dark oscillatory zoning patterns, consistent with magmatic zircon (**Figure 6**). Twenty-one analyses were conducted on twenty-one zircons and resulted in variable f_{206} values between 0 and 21.7%. One zircon (TKB-3–16) recorded very high U and Th values, but the Uranium and Thorium content for all other zircons range between 100 and 1802 and 29 and 1,071 ppm, respectively (**Table 3**), resulting in Th/U ratios between 0.02 and 1.96. The lowest Th/U values were recorded on angular euhedral zircon with clear oscillatory patterns, and the overall range of Th/U values and CL patterns suggest the zircon to be magmatic in character.

Sample TKB-4. Zircons from sample TKB-4 range in size from 50 to 200 μm and have highly variable length to width ratios between 1:1 and 4:1 (**Figure 6**). The zircons range from euhedral crystals, to irregular and rounded shapes, interpreted to possibly reflect the presence of various xenocrystic components. CL image reveals very low response for all zircons, with very faintly observable oscillatory zoning suggestive of magmatic growth (**Figure 6**). Twenty-eight analyses were conducted, including two analyses on a single zircon (TKB-4–7). Except for a few zircons, the analyses show high f_{206} values, ranging from 0 to 18.70%. The higher values correspond to high U and high Th zircon, and the U and Th values in the zircon are in the ranges 30–4,903 and 4–3,773 ppm, respectively, with Th/U ratios between 0 and 2.14. Nineteen analyses display extremely low Th/U values consistent with metamorphic zircon, but these analyses correspond to euhedral elongate zircon grains and are thus unlikely related to metamorphic growth.